3-2022

Co-Seismic and Post-Seismic deformation for the 1995 Colima–Jalisco and 2003 Tecoman thrust earthquakes, Mexico subduction zone,´ from modelling of GPS data

Beatriz Cosenza-Muralles
University of Wisconsin-Madison

Charles DeMets
University of Wisconsin - Madison

O. Sanchez
Portland State University

Enrique Cabral-Cano
Universidad Nacional Autonoma de Mexico

J. Stock
California Institute of Technology

See next page for additional authors

Citation Details

Cosenza-Muralles, B., DeMets, C., Márquez-Azúa, B., Sánchez, O., Stock, J., Cabral-Cano, E., & McCaffrey, R. (2022). Co-seismic and post-seismic deformation for the 1995 Colima–Jalisco and 2003 Tecomán thrust earthquakes, Mexico subduction zone, from modelling of GPS data. Geophysical Journal International, 228(3), 2137-2173.

Authors

Beatriz Cosenza-Muralles, Charles DeMets, O. Sanchez, Enrique Cabral-Cano, J. Stock, B. Márquez-Azúa, and Robert McCaffrey

Geophysical Journal International

Geophys. J. Int. (2022) **228,** 2137–2173 https://doi.org/10.1093/gji/ggab435
Advance Access publication 2021 October 25
GJI Geodynamics and Tectonics

Co-seismic and post-seismic deformation for the 1995 Colima–Jalisco and 2003 Tecomán thrust earthquakes, Mexico subduction zone, from modelling of GPS data

B. Cosenza-Muralles,[1,2] C. DeMets,[1] B. Márquez-Azúa,[3] O. Sánchez,[4] J. Stock,[5]
E. Cabral-Cano[4] and R. McCaffrey[6]

[1] *Department of Geoscience, University of Wisconsin-Madison, Madison, WI* 53706, *USA. E-mail: cosenzamural@wisc.edu*
[2] *Instituto de Investigación en Ciencias Físicas y Matemáticas, Escuela de Ciencias Físicas y Matemáticas, Universidad de San Carlos de Guatemala,* 01012 *Ciudad de Guatemala, Guatemala*
[3] *Departamento de Estudios Socio Urbanos, Universidad de Guadalajara,* 44100 *Guadalajara, Jalisco, México*
[4] *Instituto de Geofísica, Universidad Nacional Autónoma de México, Ciudad Universitaria, México CDMX* 04510, *México*
[5] *Caltech Seismological Laboratory, California Institute of Technology, Pasadena, CA* 91125, *USA*
[6] *Department of Geology, Portland State University, Portland, OR* 97201, *USA*

Accepted 2021 October 20. Received 2021 October 17; in original form 2021 January 29

SUMMARY

We invert ∼25 yr of campaign and continuous Global Positioning System daily positions at 62 sites in southwestern Mexico to estimate co-seismic and post-seismic afterslip solutions for the 1995 $M_w = 8.0$ Colima–Jalisco and the 2003 $M_w = 7.5$ Tecomán earthquakes, and the long-term velocity of each GPS site. Estimates of the viscoelastic effects of both earthquakes from a 3-D model with an elastic crust and subducting slab, and linear Maxwell viscoelastic mantle are used to correct the GPS position time-series prior to our time-dependent inversions. The preferred model, which optimizes the fit to data from several years of rapid post-seismic deformation after the larger 1995 earthquake, has a mantle Maxwell time of 15 yr (viscosity of 2×10^{19} Pa s), although upper-mantle viscosities as low as 5×10^{18} Pa s cannot be excluded. Our geodetic slip solutions for both earthquakes agree well with previous estimates derived from seismic data or via static co-seismic offset modelling. The afterslip solutions for both earthquakes suggest that most afterslip coincided with the rupture areas or occurred farther downdip and had cumulative moments similar to or larger than the co-seismic moments. Afterslip thus appears to relieve significant stress along the Rivera plate subduction interface, including the area of the interface between a region of deep non-volcanic tremor and the shallower seismogenic zone. We compare the locations of the seismogenic zone, afterslip and tremor in our study area to those of the neighbouring Guerrero and Oaxaca segments of the Mexico subduction zone. Our newly derived interseismic GPS site velocities, the first for western Mexico that are corrected for the co-seismic and post-seismic effects of the 1995 and 2003 earthquakes, are essential for future estimates of the interseismic subduction interface locking and hence the associated seismic hazard.

Key words: Satellite geodesy; Seismic cycle; Space geodetic surveys; Transient deformation; Subduction zone processes.

1 INTRODUCTION

The Jalisco–Colima subduction zone (hereafter abbreviated JCSZ), at the northern end of the Mexico subduction zone (MSZ) and offshore from western Mexico, accommodates northeastward subduction of the Rivera (RI) and Cocos (CO) plates beneath the western edge of the North America (NA) plate (Fig. 1). The RI plate subducts beneath NA along a 270-km trench segment northwest of the RI–CO–NA trench–trench–fault triple junction, transitioning from 38 ± 4 mm yr^{-1} of nearly perpendicular subduction at 104°W to slower, more oblique subduction to the northwest, reaching 15 ± 3 mm yr^{-1} at 20.8°N (DeMets & Wilson 1997). The Cocos plate, on the other hand, subducts at 51 ± 2 mm yr^{-1} along the trench south and east of the Colima Graben (Fig. 1).

Global Positioning System (GPS) measurements in Jalisco began in the mid-1990s as part of an effort to study the regional subduc-

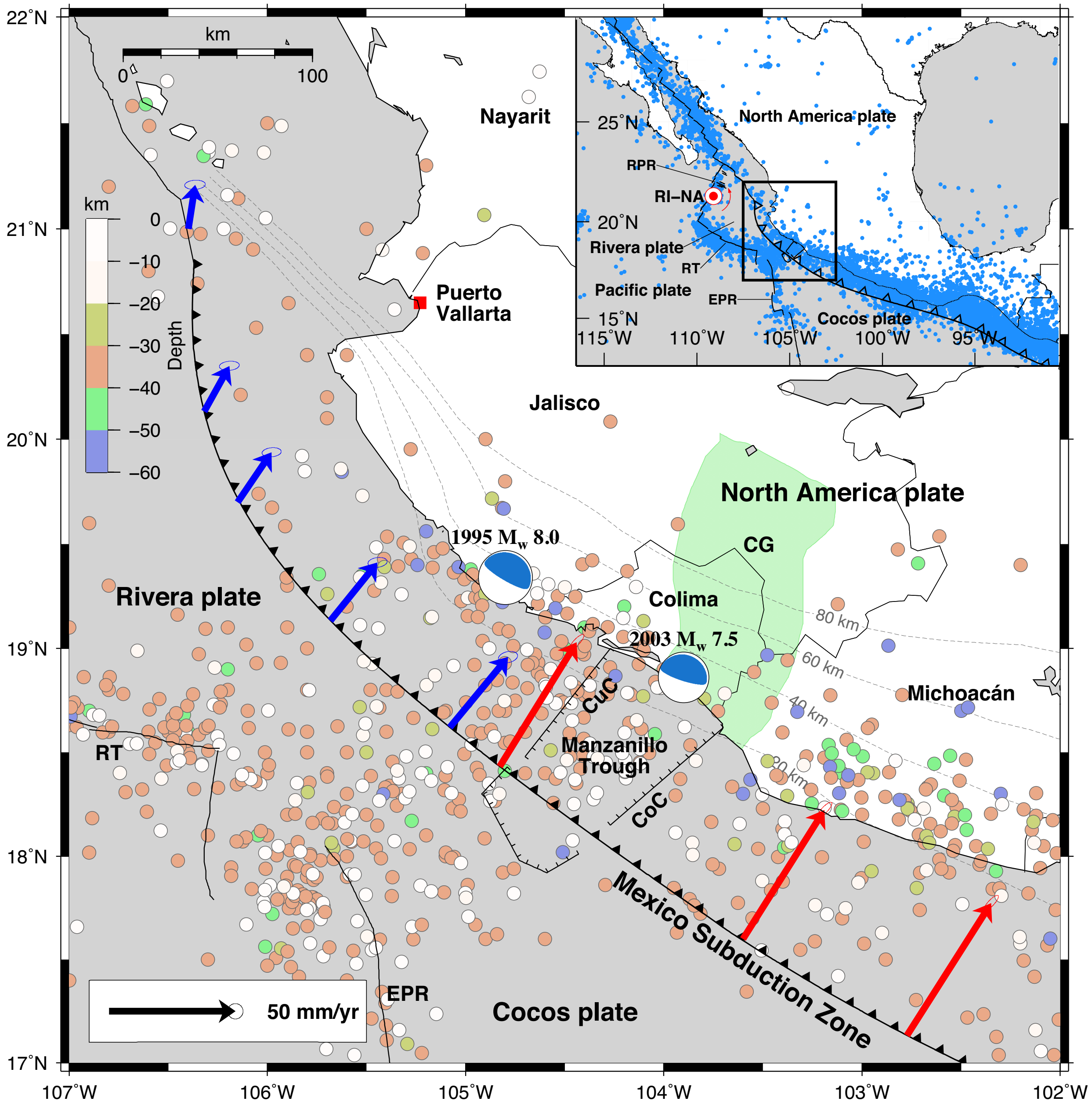

Figure 1. Tectonic setting. Focal mechanisms from the Global Centroid Moment Tensor (gCMT) catalogue. Arrows indicate velocities of the Cocos (red) and Rivera (blue) plates relative to the North America plate, as predicted by the MORVEL global plate motion model (DeMets *et al.* 2010). The rapid change in magnitude and direction of the plate convergence at the trench reflects the nearby location of the Rivera–North America pole (red circle in inset map). Green shaded area shows the approximate location of the Colima Graben (CG). CoC: Coahuayana canyon. CuC: Cuyutlán canyon. EPR: East Pacific Rise. RPR: Rivera–Pacific Ridge. RT: Rivera transform. Dashed lines show the slab contours every 20 km. Coloured circles show the $M \geq 3.0$ earthquakes with depths $\leq$60 km from 1962 to 2017 from the United States Geologic Survey (USGS) catalogue. The seismicity suggests distributed shear across a diffuse Rivera–Cocos plate boundary (DeMets & Wilson 1997).

tion earthquake cycle and associated seismic hazards (DeMets *et al.* 1995; Cabral-Cano *et al.* 2018). Multiple large subduction thrust earthquakes have ruptured the Jalisco–Colima subduction interface during the past century, including $M_s \sim 8.2$ and $M_s \sim 7.8$ earthquakes in 1932 (Singh *et al.* 1985), the 1973 $M_w \sim 7.6$ Colima earthquake (Reyes *et al.* 1979), the 1995 $M_w = 8.0$ Colima–Jalisco earthquake and the 2003 $M_w = 7.5$ Tecomán earthquake (Fig. 2). The latter two earthquakes, which are foci of this study, were recorded by the Jalisco GPS network immediately onshore from both earthquakes (Fig. 2).

The 1932 June 3 and 18 earthquakes ruptured the shallow part of the RI-NA interface in a combined area of ∼280 km by ∼80 km, as estimated from aftershocks (Singh *et al.* 1985). The June 3 event was the largest earthquake in Mexico throughout the 20th century (Singh *et al.* 2003). Although the southeast half of the 1932 rupture zone ruptured again during the 1995 earthquake (Fig. 2), the northwestern ∼120 km of the 1932 rupture zone, offshore from major tourist resorts along Jalisco's Gold Coast (Figs 1 and 2), has been seismically quiescent since 1932 (Ortiz *et al.* 1998). The January 30, 1973 earthquake (Fig. 2) ruptured ∼90 km of the subduction

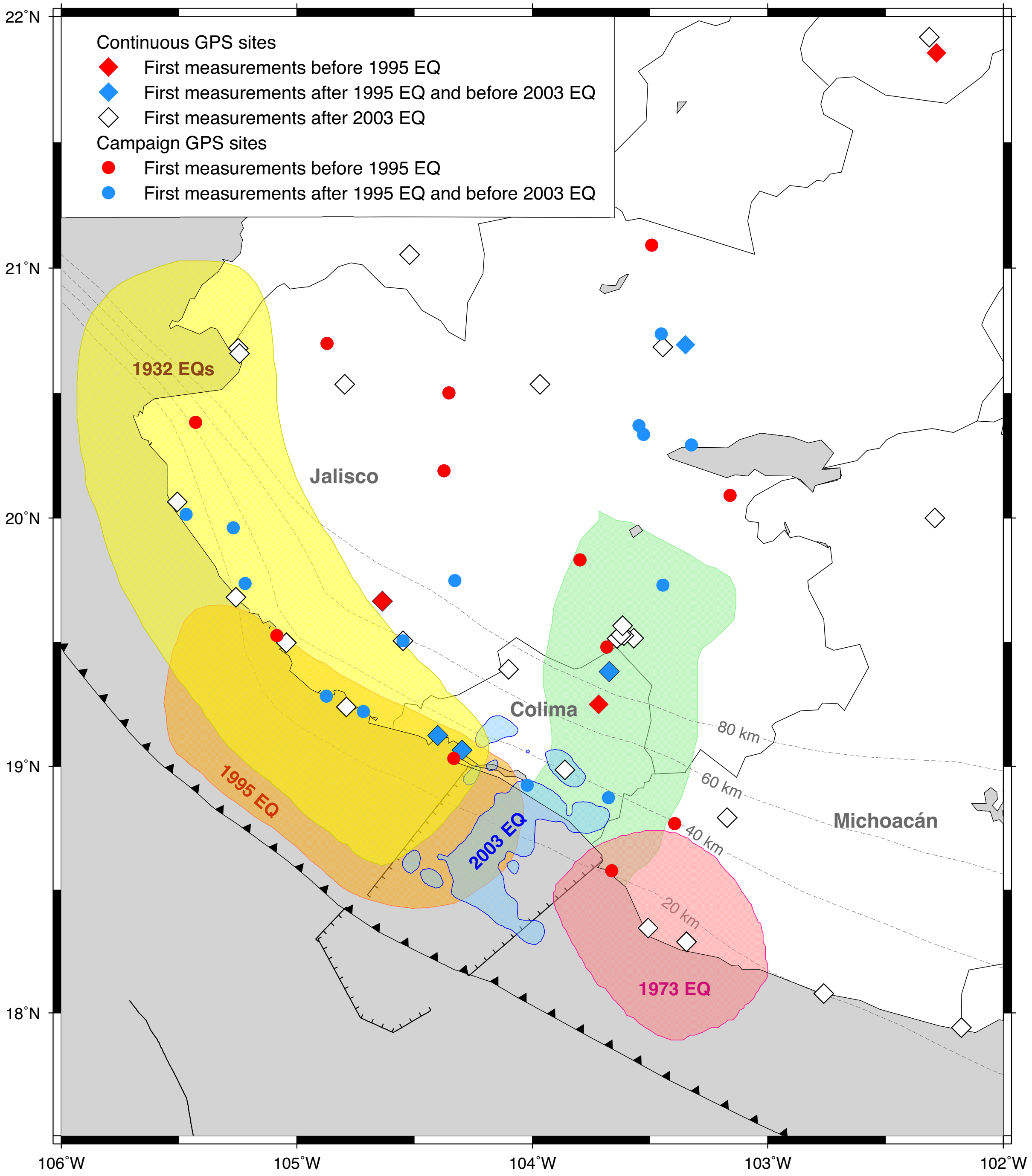

Figure 2. Locations of the GPS stations used in this study. The yellow patch is the total estimated aftershock area of the 1932 June 3 and 18 earthquakes (Singh *et al.* 1985). Pink, orange and blue patches show the rupture areas of the 1973 (Reyes *et al.* 1979), 1995 (Pacheco *et al.* 1997) and 2003 (Yagi *et al.* 2004) earthquakes, respectively. Green shaded area shows the approximate location of the Colima Graben. Dashed lines show the slab contours every 20 km.

zone immediately southeast of the Colima Graben, where the Cocos plate subducts (Reyes *et al.* 1979).

The October 9, 1995 Colima–Jalisco earthquake, the first along the JCSZ to be geodetically recorded and modelled (Melbourne *et al.* 1997; Hutton *et al.* 2001; Schmitt *et al.* 2007), was the first large rupture of the JCSZ segment since 1932. Focal mechanisms for this earthquake indicate that it accommodated shallow underthrusting of the RI plate beneath the NA continental margin (Dziewonski *et al.* 1997; Escobedo *et al.* 1998; Fig. 1). Modelling of its local and teleseismic body waveforms (e.g. Courboulex *et al.* 1997; Escobedo *et al.* 1998; Mendoza & Hartzell 1999) indicate that the ∼150 km-long rupture initiated at depths of 15–20 km near the Cuyutlán submarine canyon (labelled 'CuC' in Fig. 1). The Cuyutlán canyon along with the Coahuayana canyon (CoC in Fig. 1) delimit a deforming offshore area (e.g. Bandy *et al.* 2005) that we refer to hereafter as the Manzanillo Trough. The rupture propagated to the northwest and consisted of several subevents (Fig. 2). Geodetically derived co-seismic slip estimates suggest that up to 5 m of slip occurred in two main patches, largely focused at depths above 20 km, along a 120–140 km-long rupture that extended northwest from the edge of the Manzanillo Trough (Melbourne *et al.* 1997; Hutton *et al.* 2001; Schmitt *et al.* 2007), in agreement with the seismic estimates referenced above. The earthquake triggered transient fault afterslip mostly downdip from the co-seismic rupture zone, which by 1999 had accumulated an equivalent seismic moment of ∼70 per cent of the co-seismic moment release (Hutton *et al.* 2001). Masterlark *et al.* (2001) and Marquez-Azua *et al.* (2002) show that a combination of fault afterslip and viscoelastic rebound are needed to account for the observed transient post-seismic deformation.

The most recent large earthquake along the JCSZ was the January 22, 2003 Tecomán earthquake, which ruptured the subduction interface below the Manzanillo Trough (Fig. 1; Ekström *et al.* 2004; Yagi *et al.* 2004). Modelling of waveforms from local and teleseismic body wave data suggest that this rupture initiated at a depth of ∼20 km and propagated up- and downdip (Yagi *et al.* 2004; Fig. 2). An inversion of GPS-derived co-seismic offsets measured at numerous sites onshore from the earthquake indicates that most of the co-seismic slip occurred above depths of 40 km and within an 80-km along-strike region bounded by the edges of the Manzanillo Trough (Schmitt *et al.* 2007), in agreement with the seismic results. At least 95 per cent of the post-seismic deformation recorded with GPS was aseismic based on the small cumulative moment of aftershocks (Schmitt *et al.* 2007). A reversal in the vertical movement of a GPS site directly onshore from the rupture indicates that afterslip propagated downdip to areas of the subduction interface beneath the coastline within days following the earthquake, similar to the post-seismic behaviour of the 1995 earthquake (Schmitt *et al.* 2007).

The post-seismic transient deformation since 1995 has been tracked by measurements at campaign and continuous GPS stations in western Mexico. As an example, continuous GPS measurements at site COLI onshore from the 1995 and 2003 earthquakes (inset map in Fig. 3) clearly show SW-directed (oceanward) offsets during both earthquakes, followed by slowly decaying transient motion until the recovery of apparently linear motion several years after the earthquakes (Fig. 3). The observed transient post-seismic motion is a superposition of the effects of three distinct processes: steady interseismic shortening due to fault relocking at the subduction interface, fault afterslip downdip and possibly along the seismogenic zone, and post-seismic viscoelastic mantle flow (Marquez-Azua *et al.* 2002; Wang *et al.* 2012; Bedford *et al.* 2016). The latter two processes decay with different characteristic timescales after the earthquakes. At present, the motions at sites in western Mexico are a superposition of steady interseismic strain accumulation due to frictional locking of the Mexico subduction interface and transient surface deformations from post-seismic afterslip and viscoelastic rebound triggered by the 1995 and 2003 earthquakes.

In this first part of a two-part study, we estimate geodetic co-seismic slip and post-seismic afterslip solutions for the 1995 Colima–Jalisco and 2003 Tecomán earthquakes via time-dependent modelling of 1993-to-2020 GPS daily station positions from the state of Jalisco and neighbouring states, including calibrations for the viscoelastic rebound triggered by these events. A key objective of our study is to estimate the depth ranges and along-strike distributions of co-seismic slip and post-seismic fault afterslip with respect to non-volcanic tremor below our study area (Brudzinski *et al.* 2016). These estimates would contribute to a better understanding of the range of fault slip phenomena that accommodate the long-term plate convergence along the JCSZ and their locations on the subduction interface. We also estimate the long-term velocities of all the GPS sites fully corrected for the co-seismic and post-seismic effects of the 1995 and 2003 earthquakes. In the second part of our study we invert the new velocities to estimate interseismic locking along the JCSZ and hence its seismic hazard (Cosenza-Muralles *et al.* 2021). Hereafter, we refer to the second-stage study as CM21-II.

2 GPS DATA

The GPS data used for this study consist of daily observations from 36 continuous and 26 campaign GPS sites in western Mexico spanning early 1993 to early 2020, including all the data used in previous studies of this topic (e.g. Melbourne *et al.* 1997; Hutton *et al.* 2001; Melbourne *et al.* 2002; Marquez-Azua *et al.* 2002; Schmitt *et al.* 2007; Selvans *et al.* 2011). Fig. 2 and Supporting Information Fig. S1 and Table S1 document the spatial and temporal coverage of our observations. Highlights include the following:

(i) Of the fifteen GPS sites with observations before the October 1995 earthquake, two sites (COLI near the coast and INEG farther inland) are continuous and were installed in 1993. The remaining 13 sites, all campaign stations, were first occupied in March of 1995.

(ii) Thirty sites were operational during the January 2003 earthquake, of which five were continuous and two began as campaign stations and were converted to continuous operation after the 2003 earthquake (PURI and COOB).

(iii) Twenty-nine sites, all continuous, began operating after the 2003 earthquake. Five continuous stations, namely TNCM, TNLC, TNM2, MNZO and TNMR, were installed at the same locations of earlier discontinued stations: CHMC, GUFI, UCOL, MANZ and MMIG, respectively.

3 DATA ANALYSIS

3.1 GPS analysis methodology

We analysed all of the GPS code-phase data with releases 6.3 and 6.4 of the GIPSY software suite from the Jet Propulsion Laboratory (JPL). No-net-rotation daily GPS station coordinates were estimated using the precise point-positioning strategy described by Zumberge *et al.* (1997). Our processing methodology includes constraints on *a priori* tropospheric hydrostatic and wet delays from Vienna Mapping Function parameters (http://ggosatm.hg.tuwien.ac.at), elevation dependent and azimuthally dependent GPS and satellite antenna phase centre corrections from IGS08 ANTEX files (available via ftp from sideshow.jpl.nasa.gov) and FES2004 corrections for ocean tidal loading (holt.oso.chalmers.se). Phase ambiguities were resolved using GIPSY's single-station ambiguity-resolution feature (Bertiger *et al.* 2010). Daily no-net rotation station location estimates were transformed to IGS14, which conforms to ITRF2014 (Altamimi *et al.* 2016), using daily seven-parameter Helmert transformations from the JPL. We estimated daily correlated noise between stations from the coordinate time-series of linearly moving continuous stations outside the study area (Marquez-Azua & DeMets 2003). Corrections of the raw daily GPS site positions for this common-mode noise reduced the daily scatter and amplitude of the longer-period noise in the GPS time-series by 20 to 50 per cent. All GPS coordinate time-series were also corrected for equipment-related offsets and other discontinuities not related to earthquakes. Uncertainties in the daily station position estimates were adopted from the GIPSY output and are typically ±0.6 mm in longitude, ±0.5 mm in latitude and ±2.5 mm in elevation.

Prior to any modelling, we transformed each GPS position time-series from the ITRF14/IGS14 frame of reference to a frame of

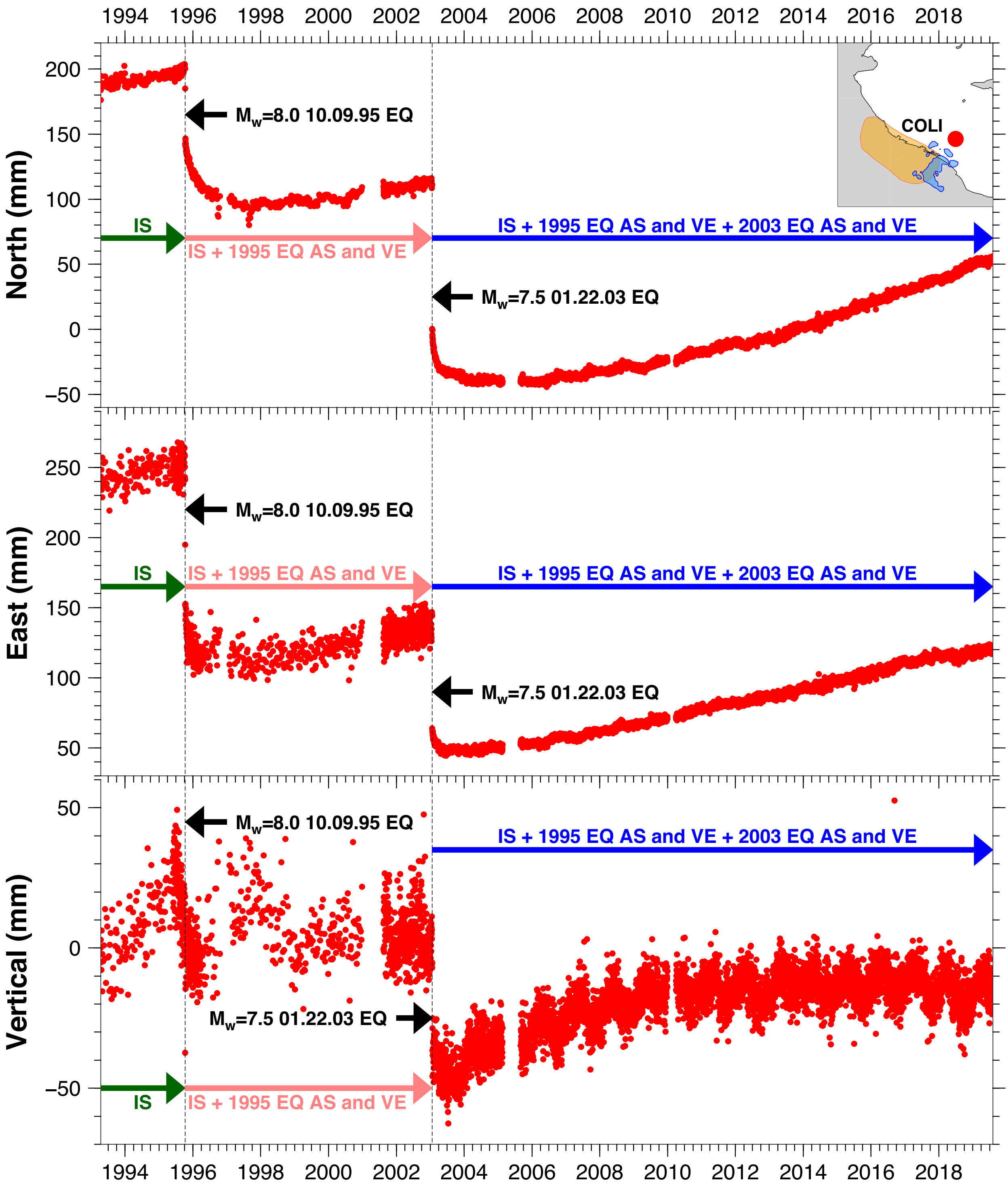

Figure 3. GPS station COLI daily positions, 1993 to 2019. The inset map shows the site location and 1995 and 2003 earthquake rupture areas. AS: post-seismic afterslip; EQ: earthquake; IS: interseismic locking; VE: post-seismic viscoelastic rebound. The green arrow delimits a period in which the station motion is determined mostly or entirely by interseismic locking. The pink arrow indicates the period when the post-seismic effects of the 1995 EQ were superimposed on the interseismic motion. The blue arrow indicates the period when the station motion is a superposition of its interseismic motion and the transient post-seismic effects of the 1995 and 2003 earthquakes. The smaller scatter after early 2003 was caused by a change in the GPS equipment.

reference tied to the NA plate, the natural geological frame of reference for this study. To do so, we used a pole located at 7.45°N, 92.04°E with an angular rate 0.183×10^{-6} deg yr^{-1}, which best fits the ITRF14 velocities of ∼1000 GPS sites from the North America plate interior. The formal uncertainties in the NA-IGS14 angular velocity vector propagate into 1σ uncertainties of only ±0.03 mm yr^{-1} in the north and east components of the velocity for the North America plate relative to IGS14 at the centre of our study area, too small to affect any of the results or interpretations that follow.

3.2 1993 to 2020 GPS site position time-series

The 1995 and 2003 earthquakes strongly influenced horizontal (Fig. 4) and vertical (Fig. 5) station movements in our study area. For example, during the years immediately after the 1995 $M_w = 8.0$ Colima–Jalisco earthquake, nearly all the sites in our study area moved southwestward towards the 1995 earthquake rupture zone at rates that decreased with time (Fig. 4; also see Hutton *et al.* 2001). The cumulative post-seismic site displacements during this period ranged from a maximum of ∼200 mm at site PURI ∼30 km inland from the rupture to a minimum of ∼50 mm at site MCAB ∼250 km inland from the earthquake. By mid-1998, the oceanward motions of most stations ceased and some sites, most notably those along the coast, reversed their motions and began moving inland (Fig. 4). Hutton *et al.* (2001) find that the temporal evolution of the horizontal displacements up to 1999 is well approximated by logarithmic decay curves with a time constant of ∼2.4–3.7 d, consistent with afterslip on the subduction interface. Marquez-Azua *et al.* (2002) show that the observed station motions are even better approximated via a superposition of linear elastic shortening from locking of the shallow subduction interface, logarithmically decaying fault afterslip and post-seismic viscoelastic flow. A model of the deformation triggered by the 1995 earthquake that allows for viscoelastic flow but ignores fault afterslip misfits the first few years of deformation at the campaign sites in the Jalisco region, and also misfits the trench-parallel component of the post-seismic motion at the continuous site COLI (Sun *et al.* 2018).

The vertical motions of GPS sites in our study area (Fig. 5; Hutton *et al.* 2001) were also strongly influenced by the 1995 earthquake. Within a few months of the earthquake, the elevations of nearly all the coastal sites and a few inland sites (i.e. AUTA, AYUT and GUFI) increased, whereas most inland sites subsided. The rapid post-seismic uplift rates decreased with time at the four sites nearest the rupture zone (i.e. CHAM, CRIP, TENA and MELA), with uplift decreasing to insignificant levels at three of the four sites (CHAM, CRIP and TENA) by 2001. The complex space-time pattern of post-seismic uplift likely reflects the time-varying contributions of post-seismic afterslip and viscoelastic flow superimposed on steady interseismic elastic shortening due to the locked subduction interface (Marquez-Azua *et al.* 2002).

The 3-D post-seismic effects of the $M_w = 7.5$ 2003 January 22 Tecomán earthquake (Figs 6 and 7) were also apparent in most of our study area. The maximum horizontal post-seismic displacements were a few tens of millimetres, ∼25 per cent of those for the larger-magnitude 1995 earthquake (Figs 4 and 5). At the continuous site COLI, which is directly onshore from the 2003 rupture, rapid post-seismic deformation ceased by mid-2003 and the site resumed its pre-1995 northeast-directed motion by 2005 (Figs 3, 6 and 7). Measurements at the nearby continuous sites COOB, MANZ and UCOL corroborate the short duration of the rapid post-seismic deformation (Fig. 6a). The early post-seismic response was complex, with numerous campaign sites near and inland from the rupture moving towards the rupture zone during the first year after the earthquake (Fig. 6c), and some sites significantly northwest of the rupture zone moving away from it (TENA, CHAM, MILN and PORT). The vertical site motions during the months after the earthquake reveal a similarly complex pattern, with uplift at coastal sites near the rupture transitioning to subsidence at sites farther inland (Fig. 7). By 2–2.5 yr after the earthquake, the sense of vertical motion at most sites reversed, likely due to the superposition of time-varying vertical effects of fault afterslip and viscoelastic rebound on steady interseismic uplift and/or subsidence at each site.

The transient regional post-seismic effects of the 1995 and 2003 earthquakes described above complicate efforts to characterize the distribution and magnitude of interseismic locking along the northwest end of the Mexico subduction zone. Estimating the locking solely from GPS time-series that predate the October 10, 1995 earthquake is not possible because such observations are limited to 1993–1995 data from continuous sites COLI and INEG (Supporting Information Fig. S1). Here, we invert ∼25 yr of data to separate the long-term steady interseismic motion of each site from the transient deformation components.

4 METHODS: TIME-DEPENDENT MODELLING

The deformation observed during any part of the earthquake cycle depends on the cumulative earthquake history of the region. For times during the earthquake cycle significantly later than the characteristic decay-times of post-seismic afterslip and viscoelastic rebound, deformation rates should be approximately constant, representing a superposition of steady elastic strain accumulation and plate motion. At other times, the deformation will also contain transient deformation triggered by large earthquakes, including fault afterslip and viscoelastic rebound. Fault afterslip is typically assumed to be restricted to the brittle upper crust and involves short-term, continued slip around the region of co-seismic rupture. Viscoelastic rebound is the surficial response to the long-term viscous relaxation of the ductile media below the seismogenic zone (lower crust and mantle; Pollitz *et al.* 1998; Wang 2007). Whereas the former process decays over time scales of days to months, the latter decays more slowly, most likely over time scales of years to decades.

Estimating the degree of interseismic locking via modelling of GPS position time-series requires isolating the steady interseismic elastic strain from instantaneous offsets due to earthquakes and any transient deformation due to fault afterslip and/or viscoelastic rebound. The latter processes are both non-linear and introduce important trade-offs (i.e. correlations) between their adjustable parameters (e.g. mantle viscosity, mantle-crust interface depth and afterslip decay time). Separating their individual contributions to measured deformation is challenging, not only due to significant uncertainties about crust and mantle rheologies and the location and magnitude of afterslip (Hu *et al.* 2004; Suito & Freymueller 2009; Hu & Wang 2012; Kogan *et al.* 2013; Sun & Wang 2015; Freed *et al.* 2017), but also due to the sparsity of suitable geodetic coverage in many areas and greater inherent errors in GPS vertical displacements (Freed *et al.* 2017). Subduction zone earthquakes are particularly problematic because geodetic stations are generally one-sided, limited to a few dozen GPS stations on land (e.g. Lin *et al.* 2013; Sun *et al.* 2014; Wiseman *et al.* 2015; Freed *et al.* 2017). Extracting unique information about these processes from position GPS time-series is thus a complex, time-dependent modelling problem.

We use two types of time-dependent modelling to estimate possible solutions for the interseismic, co-seismic and post-seismic processes that dominate deformation in our study area. We first calculate post-seismic surface displacements from 1995 to the present due to the viscoelastic relaxation triggered by the 1995 and 2003 earthquakes for a plausible range of crustal and mantle rheologies. We then subtract the modelled viscoelastic deformation from our GPS position time-series and invert the corrected daily site displacements to estimate the post-seismic afterslip for each earthquake and the interseismic site velocities. Co-seismic fault slip solutions for

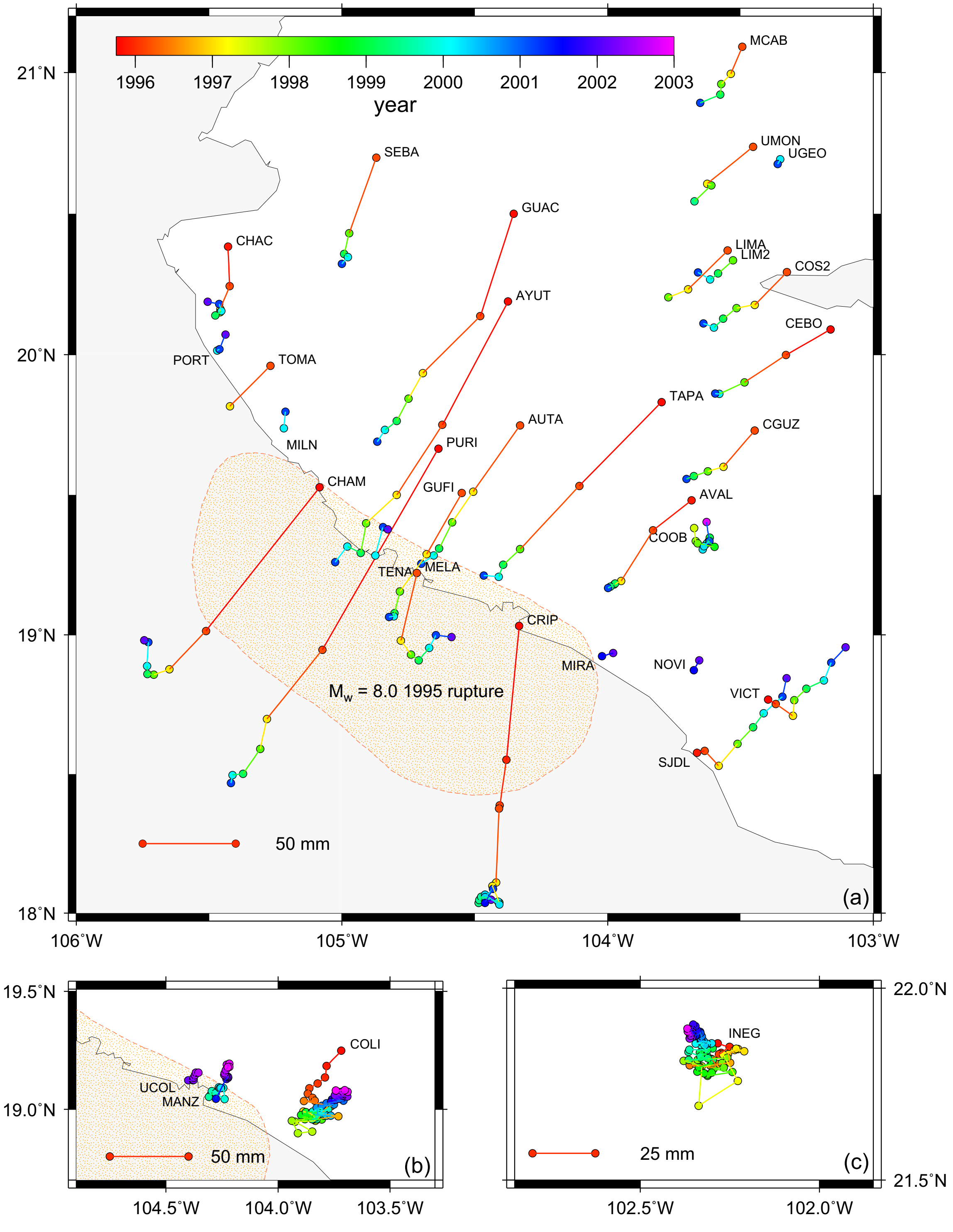

Figure 4. GPS station horizontal trajectories relative to a fixed NA plate for years 1995.77–2003.00. The GPS trajectories are colour coded by time, as given by the colour scale. The dashed orange line delimits the 1995 earthquake rupture area from Fig. 2. (a) Campaign sites. (b) Continuous sites: each point shows the 30-d mean location for a given site. (c) Continuous site farther inland.

the 1995 and 2003 earthquakes are required to drive the forward modelling of their triggered viscoelastic relaxation. Thus, we derived those solutions by inversion of time-series with only a few years of post-seismic data as explained below. For simplicity, we assume that the post-seismic effects of any earthquakes before 1995, most notably two $M \sim 8$ earthquakes in June 1932 (Singh *et al.* 1985), are negligible. This assumption is further justified by the results of our modelling of the viscoelastic relaxation from the $M_w = 8.0$ 1995 earthquake (Section 5.2). Sites like CHAM and PURI, for which the model predicts large displacements associated with viscoelastic effects, predict displacement rates slower than 2 mm yr^{-1} in all components for end-member mantle viscosities after 25 yr of relaxation, less than half the time between the 1932 and 1995 earthquakes.

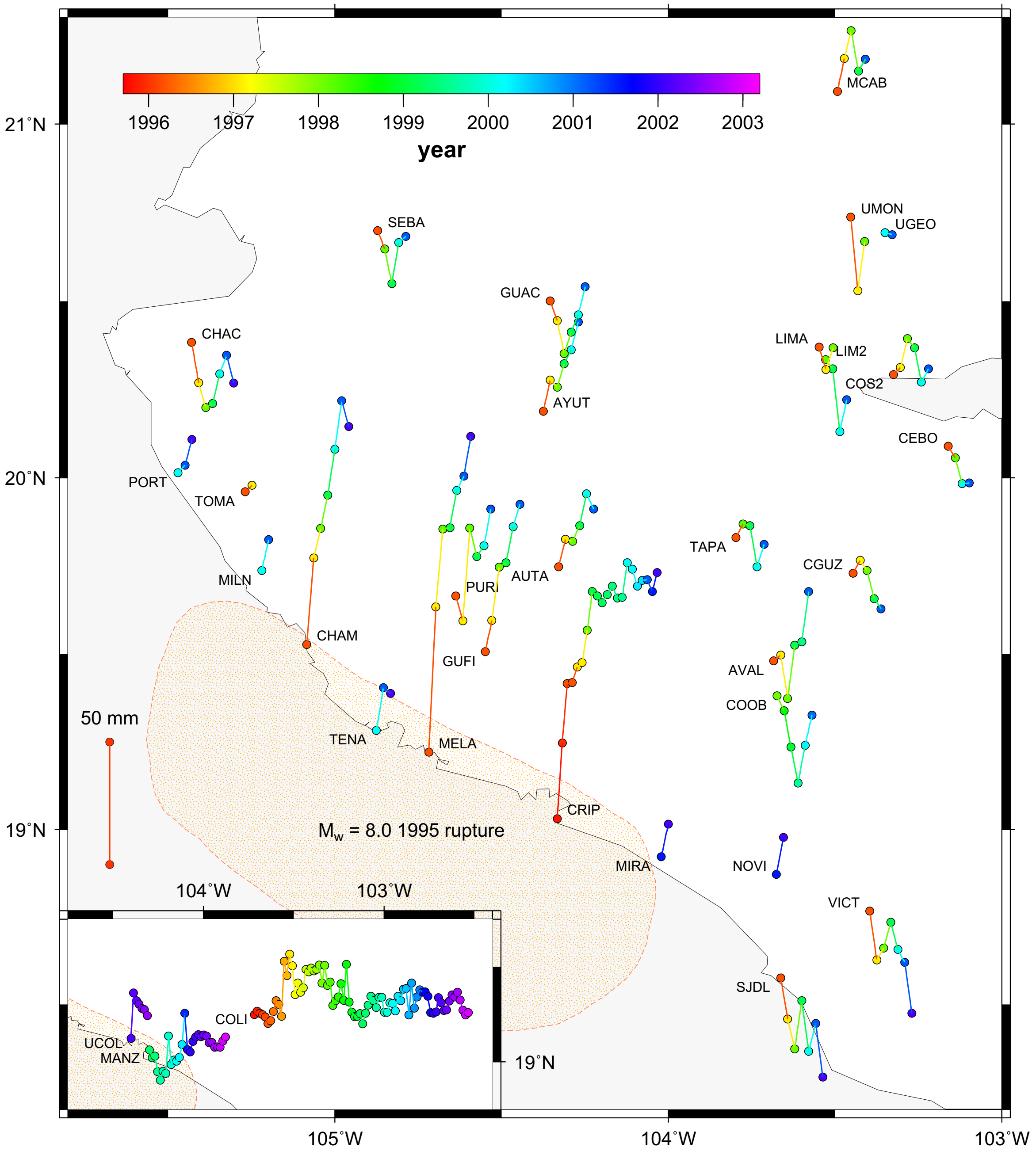

Figure 5. GPS station vertical trajectories for 1995.77–2003.00. Positions are progressively shifted to the right to help visualization. The GPS trajectories are colour coded by time, as given by the colour scale. Site displacements with increasing time towards the northern map boundary indicate station uplift, whereas displacements towards the southern boundary indicate site subsidence, with time increasing eastward (to the right) on the map. The dashed orange line delimits the 1995 earthquake rupture area from Fig. 2. Campaign sites are shown in the main figure. Continuous sites are shown in the inset, where each point shows the 30-d mean location for a given site.

Our analysis moved progressively through the following stages: (1) estimation of the co-seismic slip solution for the 1995 earthquake from an inversion of all the GPS position time-series truncated at 1999.0 (Section 5.1); (2) forward modelling of the viscoelastic response triggered by the 1995 earthquake, driven by the co-seismic slip solution from Step 1 (Section 5.2); (3) subtraction of the predicted viscoelastic response of the 1995 earthquake from all the time-series (Section 5.3); (4) estimation of the co-seismic slip solution for the 2003 earthquake from an inversion of all the GPS time-series corrected for the viscoelastic effects of the 1995 earthquake and truncated at 2005.5 (Section 5.3); (5) forward modelling of the viscoelastic responses triggered by the 2003 earthquake, driven by the co-seismic slip solutions from Step 4 (Section 5.4); (6) subtraction of the predicted viscoelastic responses of the 1995 and 2003 earthquakes from the original GPS time-series through early 2020 (Section 5.5); and (7) estimation of the afterslips triggered by

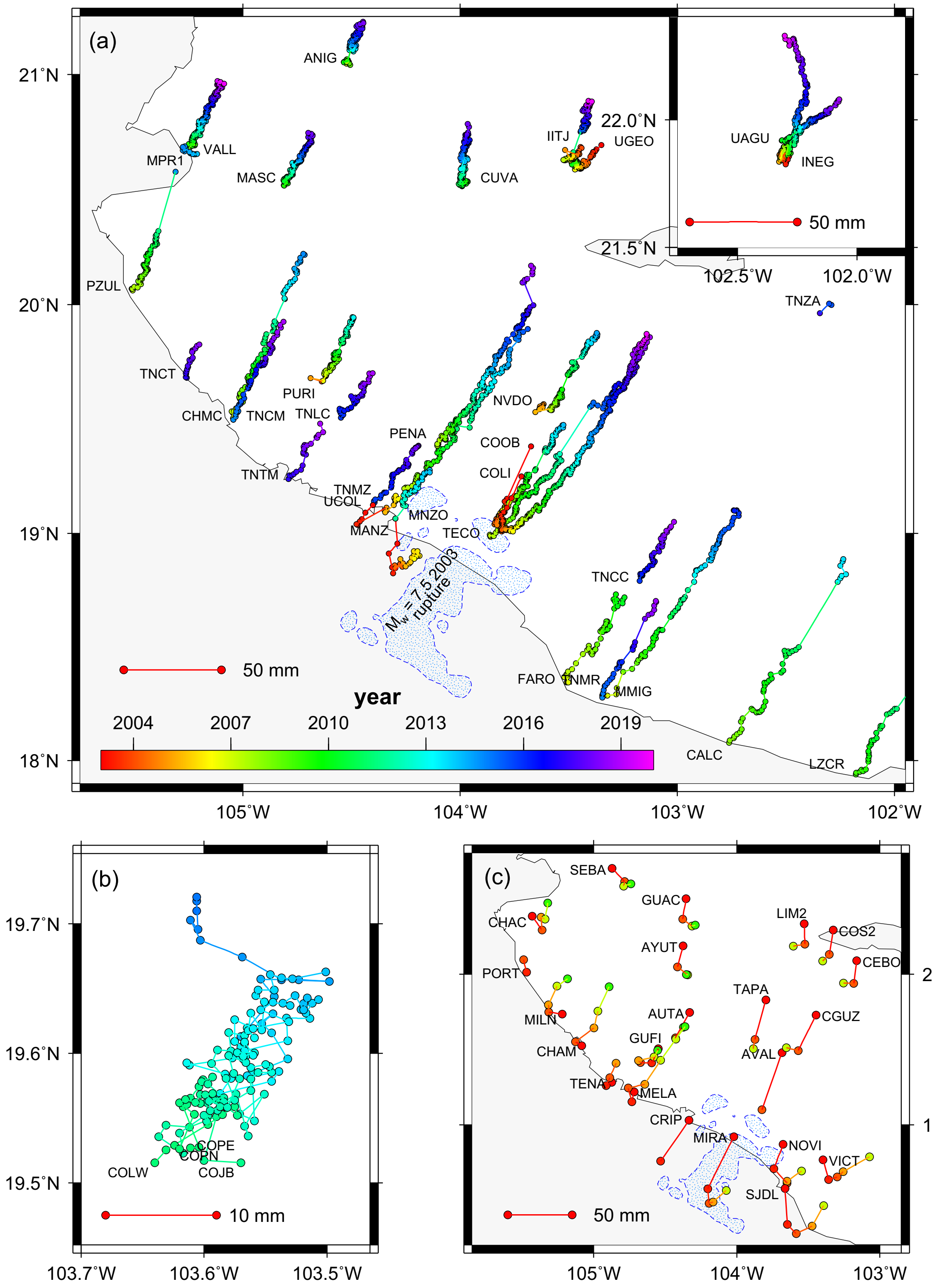

Figure 6. GPS station horizontal trajectories relative to a fixed NA plate for years 2003.08–2020.00. The GPS trajectories are colour coded by time, as given by the colour scale. The 2003 earthquake rupture area from Fig. 2 is shown in blue. (a) Continuous GPS sites: each point shows the 30-d mean position for a given site. Inset shows two continuous sites farther inland. (b) Continuous sites installed near the Nevado de Colima volcano. (c) Campaign sites.

the 1995 and 2003 earthquakes and the interseismic velocities at each GPS site via an inversion of the GPS time-series from Step 6 (Sections 5.5 and 5.6).

Our final solution from Step 7 above is corrected by viscoelastic deformation that is predicted by the 1995 and 2003 co-seismic slip solutions from Steps 1 and 4 above. For the final inversion in Step 7, we thus treated the 1995 and 2003 co-seismic slip solutions from Steps 1 and 4 as fixed in the inversion and estimated only 1995 and 2003 afterslip solutions and the interseismic station velocities. Due to the time-dependent nature of our inversions, all the parameters that are estimated trade-off with each other—for example the co-seismic offsets that are estimated for the 2003 earthquake in Step

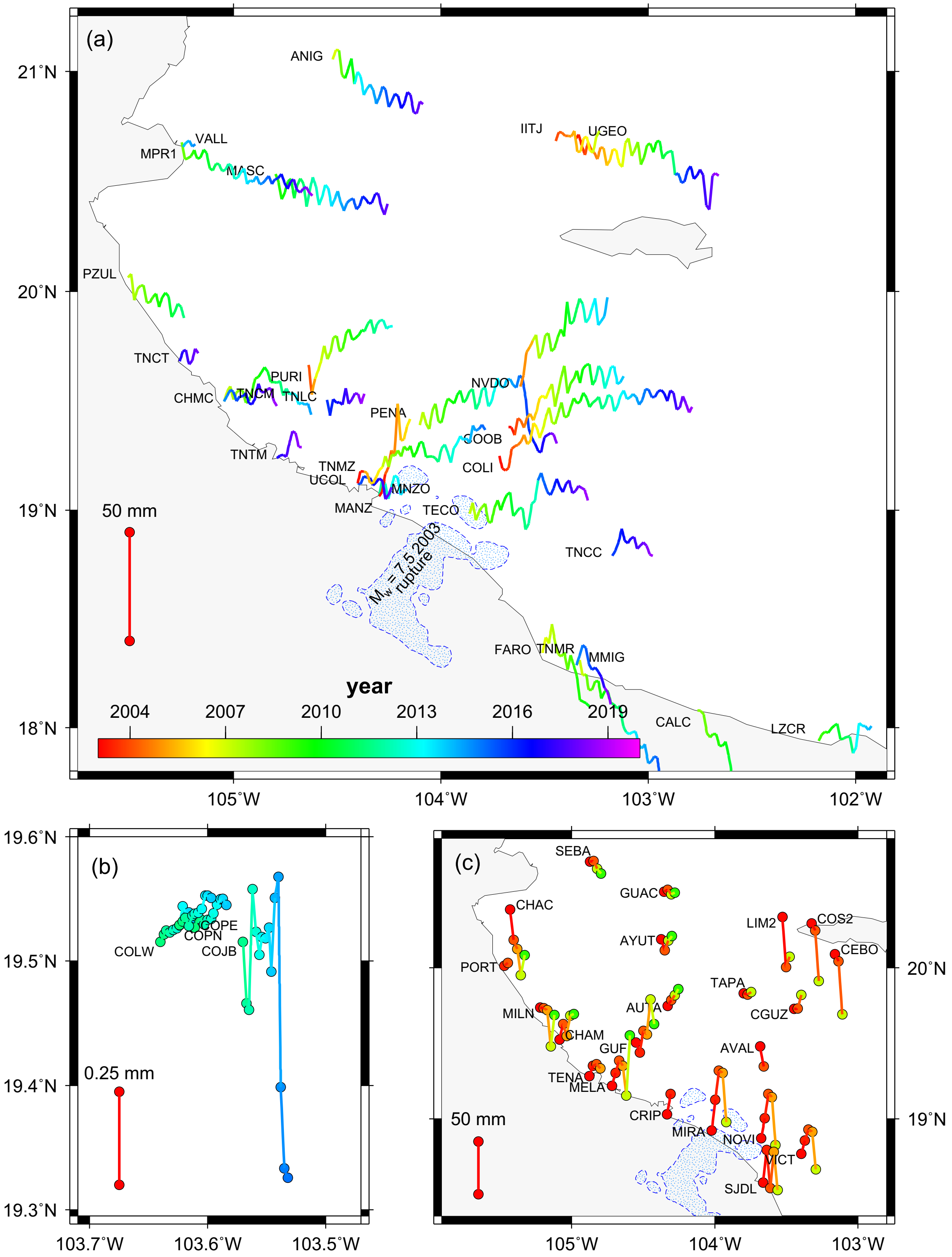

Figure 7. GPS station vertical trajectories for years 2003.08–2020.00. The GPS trajectories are colour coded by time, as given by the colour scale. Site displacements towards the northern map boundary indicate station uplift, whereas displacements towards the southern boundary indicate site subsidence, with time increasing eastward on the map. Blue dashed line delimits the 2003 earthquake rupture area from Fig. 2. (a) Continuous sites: 0.25-yr mean positions. (b) Continuous sites installed near the Nevado de Colima volcano. (c) Campaign sites.

4 depend partly on the viscoelastic corrections (and hence mantle viscosities) that are implicit in Steps 2 and 3. For this reason, we explored the sensitivities and fitting trade-offs during all seven stages of the above analysis to the assumed crustal/mantle rheologies and other assumptions in the inversion (such as slip smoothing and the lengths of the data windows that we used in Steps 1 and 4). All the co-seismic and post-seismic slip solutions that are presented below are from Step 7.

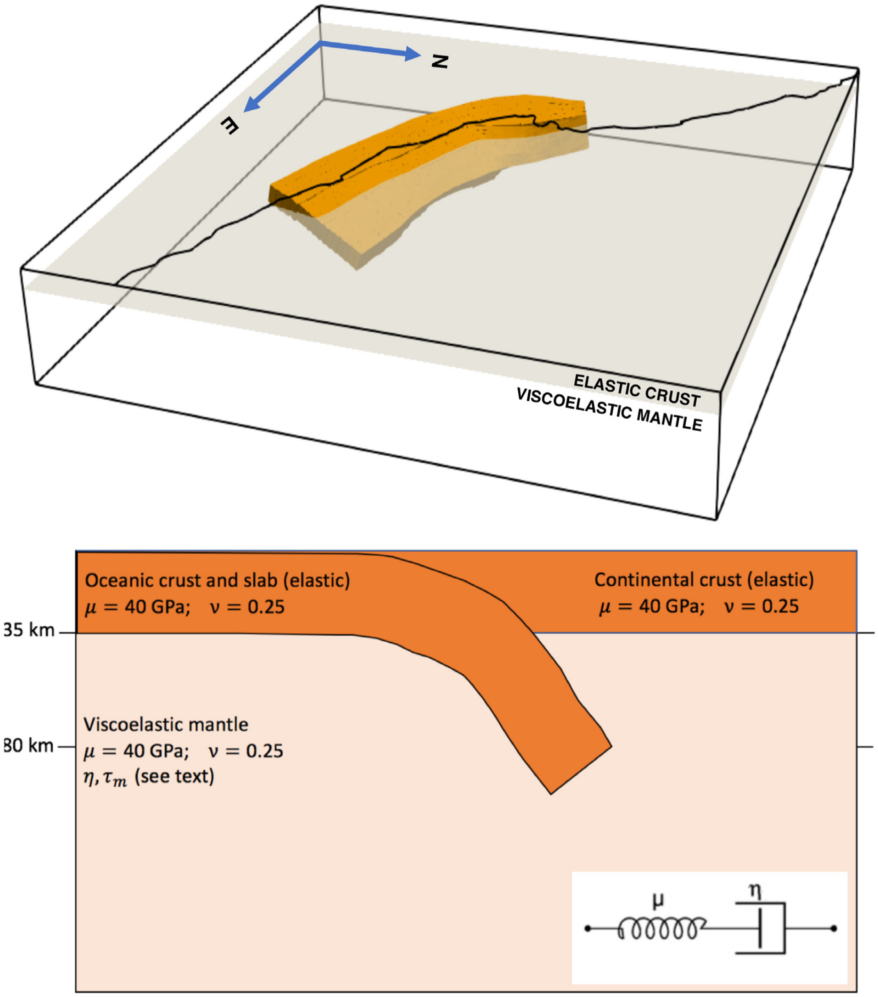

Figure 8. Geometry of the computational domain and rheological structure in modelling with RELAX. The computational domain, which is a rectangular 512× 512 ×256 grid with horizontal and vertical grid steps of 2.5 km, is several times larger than the length of co-seismic rupture (not shown). The top of the domain is the Earth‘s crust. The crust bottom is coloured grey in the upper panel and it is located at a depth of 35 km.

4.1 Forward modelling of the viscoelastic relaxation

We use RELAX 1.0.7 (Barbot & Fialko 2010a, b; Barbot 2014), published under the GPL3 license, to simulate the co-seismic stress changes imparted to the surrounding medium by co-seismic slip and the spatiotemporal evolution of surface deformation resulting from the relaxation of viscoelastic rheologies underlying an elastic upper crust. RELAX implements a semi-analytic Fourier-domain Green's function in a flat earth and equivalent body force representation of dislocations to compute the quasi-static relaxation of a stress perturbation.

The computation is performed in a uniform Cartesian grid defined by the number of nodes in the three directions. The 2.5-km node spacing in our 512× 512 ×256 element 3-D computational grid (Fig. 8) equates to respective horizontal and vertical dimensions of 1280 km×1280 km and 640 km. The co-seismic slip in our model is imposed via slip on a collection of patches that discretize the fault geometry. Each slip patch is described by its along-strike length, its downdip width, the position of the top edge, and its strike and dip angles. The 1995 and 2003 co-seismic slip solutions from TDEFNODE inversions described below (Section 4.2) were adapted for input to RELAX in order to calculate the viscoelastic relaxation from the 1995 and 2003 earthquakes. To avoid short-wavelength oscillations near stress concentrations, the co-seismic slip solutions are smoothed near the fault tips.

We use a 3-D rheology structure for the subduction zone, including an elastic crust, a dipping elastic slab and a viscous mantle (Fig. 8). We imposed a shear modulus $\mu = 40$ GPa and a Poisson's ratio $\upsilon = 0.25$ for the whole domain. Seismicity in the JCSZ concentrates in the continental crust at depths of $\sim$15–35 km (Watkins *et al.* 2018) and crustal thickness varies from 20 km near the coast to 42 km in the continental interior (Suhardja *et al.* 2015). We thus fixed the thickness of the elastic crust at 35 km. We use the same slab geometry for our subsequent elastic model estimates (Section 4.2). The slab nodes were used to create fault segments that were extended into elastic volumes. We matched the slab thickness to that of the elastic crust and assigned a linear viscosity to the mantle, varying the Maxwell time τ_{m} from 2.5 to 40 yr (viscosities from 3.16×10^{18} Pa s to 5.06×10^{19} Pa s for $\mu = 40$ GPa). The 2.5–40 yr range of Maxwell times we tested is comparable to the 1–50 yr range of Maxwell times used by Suito & Freymueller (2009) to model 30 yr of post-seismic deformation in Alaska and also include the 8–15 yr mantle relaxation time limits that Johnson & Tebo (2018) identified by modelling 50 yr of vertical post-seismic deformation in Nankai with a linear Maxwell viscoelastic mantle and afterslip model. Similar to Johnson & Tebo (2018), we only tested linear Maxwell rheologies. We did not test Burgers rheologies because our GPS data lack the spatial and sampling density that would be needed to resolve the likely strong trade-off between the post-seismic afterslip decay constant and the characteristic decaying time of the Kelvin element of the Burgers model. Although we did not test power-law rheologies, which have been used to successfully describe post-seismic deformation in other subduction settings (Freed *et al.* 2006; Peña *et al.* 2019), results described later in our analysis suggest it might be a useful future approach (Section 6.4).

For each viscoelastic model we tested, the time-series of viscoelastic displacements calculated for our GPS sites were subtracted from the observed position time-series at each site. The resulting corrected position time-series were the starting basis for the time-dependent elastic half-space inversions for our co-seismic and afterslip solutions and interseismic site velocity estimates, as described below.

4.2 Inverse modelling with TDEFNODE

TDEFNODE calculates static and time-dependent elastic deformation using the Okada (1985, 1992) elastic half-space dislocation algorithm. It inverts campaign and continuous GPS position time-series and other geodetic, seismologic and plate kinematic data to estimate simultaneously the long-term linear (steady) motions of sites and short-term transients such as co-seismic slip, afterslip and slow slip events (McCaffrey 2009).

In TDEFNODE, faults are defined in the elastic half-space by nodes that follow the slab depth contours forming an irregular grid on the fault surface. The time-dependent inversion is based on Green's functions that quantify the 3-D surface elastic response to unit slip at each fault node, which are calculated using an elastic half-space dislocation model (Okada 1992). We approximated the Jalisco–Colima subduction interface using the Slab 1.0 geometry of Hayes *et al.* (2012) and extended the slab contours to the northwest based on results from local earthquake tomography (Watkins *et al.* 2018) and magnetotelluric imaging (Corbo-Camargo *et al.* 2013). Fault node spacings are ∼9–27 km along-strike (∼18.5 km on average) and ∼5–25 km downdip (∼10.5 km on average), located at 5-km depth contours.

In TDEFNODE, the temporal and spatial distributions of slip on a fault during an event are described by

$$s(x, w, t) = AX(x)W(w)S(t) \tag{1}$$

where s is the slip on the fault as a function of time t, and position along-strike x and downdip w; A is the amplitude; $X(x)$ and $W(w)$ are the along-strike and downdip spatial functions; and $S(t)$ is the temporal function (McCaffrey 2009). The spatial distribution of slip (X and W) can be parametrized in several ways: fault nodes can be treated as independent parameters (independent nodes), they can be grouped, or slip can be a function of the depth of the nodes. Similarly, the time dependence of slip source ($S(t)$) can be defined as impulsive, step, Gaussian, exponential, logarithmic, among others.

The parameters estimated in our TDEFNODE inversions consist of the amplitudes and rake of co-seismic and post-seismic slips at the fault nodes, the rake of the co-seismic slip and afterslip, the afterslip decay rates, and the linear station velocities. GPS station displacements are modelled in TDEFNODE as

$$d_{ij}(t) = x_{ij}^{0} + V_{ij}t + \sum_{k} H_{t_{\mathrm{eq\_}k}}(t) \times \left[A_{ij}^{\mathrm{co\_}k} + A_{ij}^{\mathrm{as\_}k}\log_{10}\left(1 + \frac{t - t_{\mathrm{eq\_}k}}{\tau_{\mathrm{c\_}k}}\right)\right] \tag{2}$$

where i denotes the ith component (east, north and up) of site j, k denotes the kth earthquake, x_{ij}^{0} is the initial position, V_{ij} is the steady (interseismic) velocity, A_{ij}^{co} and A_{ij}^{as} are amplitudes related to a site's elastic response to earthquake co-seismic slip and afterslip, respectively, $H_{t_{\mathrm{eq\_}k}}$ is the Heaviside function centred at the time of the kth earthquake t_{eq} and $\tau_{\mathrm{c\_}k}$ is the logarithmic relaxation time for the kth earthquake afterslip. This equation shows the time dependence ($S(t)$) of our slip sources: earthquakes are modelled as step functions and afterslips as logarithmic functions.

Eq. (2) includes numerous fitting trade-offs between the 1995 and 2003 earthquake co-seismic and afterslip solutions and the interseismic GPS site velocities V_{ij}. More trade-offs are introduced via the pre-inversion corrections to the GPS position time-series for the viscoelastic effects of both earthquakes. We explored these trade-offs by comparing the TDEFNODE fits for viscoelastic models that span mantle Maxwell times τ_{m} of 2.5 to 40 yr.

In our inversions, slip values for the JCSZ were estimated at each fault node (independent nodes) while applying spread smoothing, which penalizes large slip at distances progressively farther from the slip centroid and avoids implausible node-to-node variations in slip values. The misfit F is defined in TDEFNODE as the sum of the reduced chi-squared statistic (χ_{ν}^{2}), which is the weighted least-squares misfit normalized by the degrees of freedom, and the penalties associated with smoothing:

$$\begin{aligned} F &= \chi_{\nu}^{2} + \text{penalties} \\ &= \frac{1}{\nu}\sum_{N}\frac{r^{2}}{\sigma^{2}} + A_{1}\sum_{x}s^{2}dx^{2} + A_{2}\sum_{w}s^{2}dw^{2} \end{aligned} \tag{3}$$

where ν represents the degrees of freedom (number of observations N minus number of parameters); r are the residuals (observed value minus modelled value); σ are the data uncertainties; x and w denote, respectively, the fault nodes positions in the along-strike and downdip directions; A_1 and A_2 are the smoothing factors that scale the penalties in each direction, s is the slip; and dx and dw are, respectively, the along-strike and downdip distances from the slip centroid to the node location. The misfit function F is minimized through simulated annealing and grid search iterations. A measure of the goodness of fit of our solutions is the weighted root-mean-square (McCaffrey 2005):

$$\mathrm{wrms} = \left[\left(\sum_{N}\frac{r^{2}}{\sigma^{2}}\right) \Big/ \left(\sum_{N}\frac{1}{\sigma^{2}}\right)\right]^{1/2} \tag{4}$$

where N is the number of observations, r are the residuals and σ are the data uncertainties. It has units of mm and measures the weighted scatter in the fits (McCaffrey 2005).

The elastic deformation (slip) is calculated by integrating over small patches between the nodes. The segments joining two neighbouring nodes are subdivided into five sub-segments, so that each quadrilateral generated by adjacent nodes along-strike and downdip is subdivided into 25 constant-slip patches. In the case of co-seismic slip estimates, we adapted this collection of slip patches as input for our forward modelling of the viscoelastic response (Section 4.1).

4.3 Spatial resolutions of co-seismic and afterslip solutions

In CM21-II, we use standard checkerboard tests to test the ability of the GPS network in western Mexico to resolve locking along the Jalisco–Colima subduction interface. We use what we learned from those tests to assess the ability of the GPS network (or subsets of it) to recover known slip distributions for the JCSZ using known locking distributions as a proxy and establish a basis for interpreting the 1995 and 2003 earthquake co-seismic and afterslip solutions that are described in Section 5. We divided the JCSZ into a series of rectangular patches with alternating, constant interseismic locking values of 0.0 and 0.5 (upper two panels in each of Supporting Information Figs S2–S5). For each starting model, we calculated synthetic 3-D velocities at the GPS sites and perturbed the synthetic velocities with random noise of 1 mm yr^{-1} (1-sigma) for the horizontal components and 2 mm yr^{-1} for the vertical. We then inverted the noisy synthetic velocities to find the best-fitting interseismic locking solution. The upper locking limit of 0.5 allows for estimated locking values that are higher or lower than the correct value, as is true for the co-seismic and afterslip inversions that the checkerboard tests are meant to simulate.

Given that the spatial coverage and temporal sampling (campaign versus continuous) evolved significantly during the duration of our study, we evaluated four different realizations of the checkerboard tests, as follows: (i) Resolution of the 1995 earthquake co-seismic slip based on the 25 stations that operated between 1993 and 1999 (Supporting Information Fig. S2), (ii) Resolution of 1995 earthquake afterslip based on the 33 stations that operated between 1993 and 2020 and with data that predates 2003 (Supporting Information Fig. S3). (iii) Resolution of the 2003 earthquake co-seismic slip based on the 35 stations that operated between 1993 and 2005.5 and with data after 2003 (Supporting Information Fig. S4). (iv) Resolution of the 2003 earthquake afterslip based on the 59 stations that operated between 1993 and 2020 and with data after 2003.

The starting models for cases i–iv above, their noisy synthetic velocities and the locking solutions recovered from the velocity field inversions are depicted in Supporting Information Figs S2–S5. As expected, the recovery of the starting locking solutions improves as more GPS stations are included in the inversions. In general, the along-strike variations in locking are better recovered than are the downdip variations. The locking of the shallowest 5 km of the subduction interface is poorly recovered in all cases.

5 RESULTS

Outputs of the TDEFNODE inversion described in Section 4.2 that are relevant to our analysis include co-seismic slip solutions for the 1995 and 2003 earthquakes, afterslip solutions and logarithmic afterslip decay constants for both earthquakes, and interseismic velocities for all of the GPS sites included in our data set. Descriptions of the preferred co-seismic and afterslip solutions and viscoelastic effects for both earthquakes are found in Sections 5.1 to 5.5. The interseismic GPS site velocities, which are described and modelled by CM21-II, are summarized briefly in Section 5.6. In the Supporting Information, we describe results from a TDEFNODE inversion of the GPS position time-series assuming that fault afterslip was the source of all the observed transient post-seismic deformation (i.e. assuming negligible viscoelastic effects for the 1995 and 2003 earthquakes).

5.1 Co-seismic slip solution for the 1995 Colima–Jalisco earthquake

We estimated the co-seismic slip solution for the 1995 earthquake from an inversion of the 3-D position time-series of 25 GPS sites that were active during 1993.28 to 1999.00. Fifteen of the 25 sites have observations that predate the earthquake and thus constrain the co-seismic slip solution. Data from the other 10 sites help constrain the post-seismic afterslip. Data from before 1999 were dominated by annual campaign measurements. We thus inverted observations from each site up to ∼3 yr after the 1995 earthquake to ensure that sufficient data were available to constrain the transient deformation at each site. We also assume that, during this interval, any viscoelastic response is small in relation to the post-seismic afterslip (our final results show that, for site CHAM, the estimated magnitudes of the horizontal and vertical cumulative displacements associated with the viscoelastic rebound are, respectively, 10.0 per cent and 8.3 per cent that of the cumulative afterslip. In the case of COLI, the percentages are 10.0 per cent and 18.5 per cent).

Our preferred time-dependent model for 1993.28 to 1999.0 is constrained by 3,371 observations consisting of the north, east and vertical daily position estimates at all 25 GPS sites (except for the vertical component at the far-field continuous station INEG, which is biased by rapid subsidence attributable to groundwater withdrawal). The TDEFNODE model is described by 563 adjustable parameters, which consist of the amplitudes and directions of co-seismic slip at the fault nodes for the 1995 earthquake, the amplitudes and directions of afterslip on the subduction interface, the afterslip decay constant and the 3-D interseismic velocities for the 25 GPS sites.

The best-fitting co-seismic slip solution (Fig. 9a) agrees well with previous seismic estimates (e.g. Courboulex *et al.* 1997; Escobedo *et al.* 1998; Mendoza & Hartzell 1999). Most of the seismic energy (∼75 per cent) was released at depths of 5 to 20 km, consistent with seismic constraints. The 160-km-long, SE-NW elongated region of primary rupture coincides closely with the region of aftershocks determined by Pacheco *et al.* (1997; delineated by the blue line in Fig. 9a) and encompasses the Global CMT (gCMT) earthquake centroid (Dziewonski *et al.* 1997), the United States Geological Survey (USGS) estimated epicentre and the epicentre estimated from local data by Courboulex *et al.* (1997). Our estimated geodetic co-seismic moment of 9.71 × 10^{20} N m, corresponding to $M_{\mathrm{w}} =$ 7.92 for $\mu = 40$ GPa, is close to seismologic estimates of $M_{\mathrm{o}} = 1.15 \times 10^{21}$ N m (Dziewonski *et al.* 1997) and 8.3 × 10^{20} N m (Mendoza & Hartzell 1999).

Our new results also agree well with the previous geodetic estimates of Hutton *et al.* (2001) and Schmitt *et al.* (2007). For example, the seismic potency estimated in the latter study, $P_0 = 2.5 \times 10^{10}$ m^3, where the potency P_0 is defined as the estimated seismic moment normalized by the shear modulus (Ben-Menahmen & Singh 1981), differs by only 3 per cent from $P_0 = 2.43 \times 10^{10}$ m^3 for this study.

Due to the sparse GPS site distribution before year 2000 and campaign-dominated nature of the GPS sites during this period, the details of slip during the 1995 earthquake are more poorly resolved than for the 2003 earthquake slip and afterslip (compare Supporting Information Fig. S2 to Supporting Information Figs S4 and S5). The good agreement between our new co-seismic slip solution (Fig. 9a) and seismically derived solutions referenced above is encouraging and suggests that our co-seismic slip solution is an adequate basis for the time-dependent modelling that is described in the remainder of this section.

Fig. 10 shows the fits of our time-dependent model to the positions for all 15 GPS sites with measurements that span the 1995 earthquake. The wrms misfits are 3.1 to 9.5 mm in the horizontal position components at continuous sites COLI and INEG and average 3.3 mm at the 23 campaign GPS sites. The wrms misfits to the noisier vertical daily positions are 11.2 mm at site COLI and

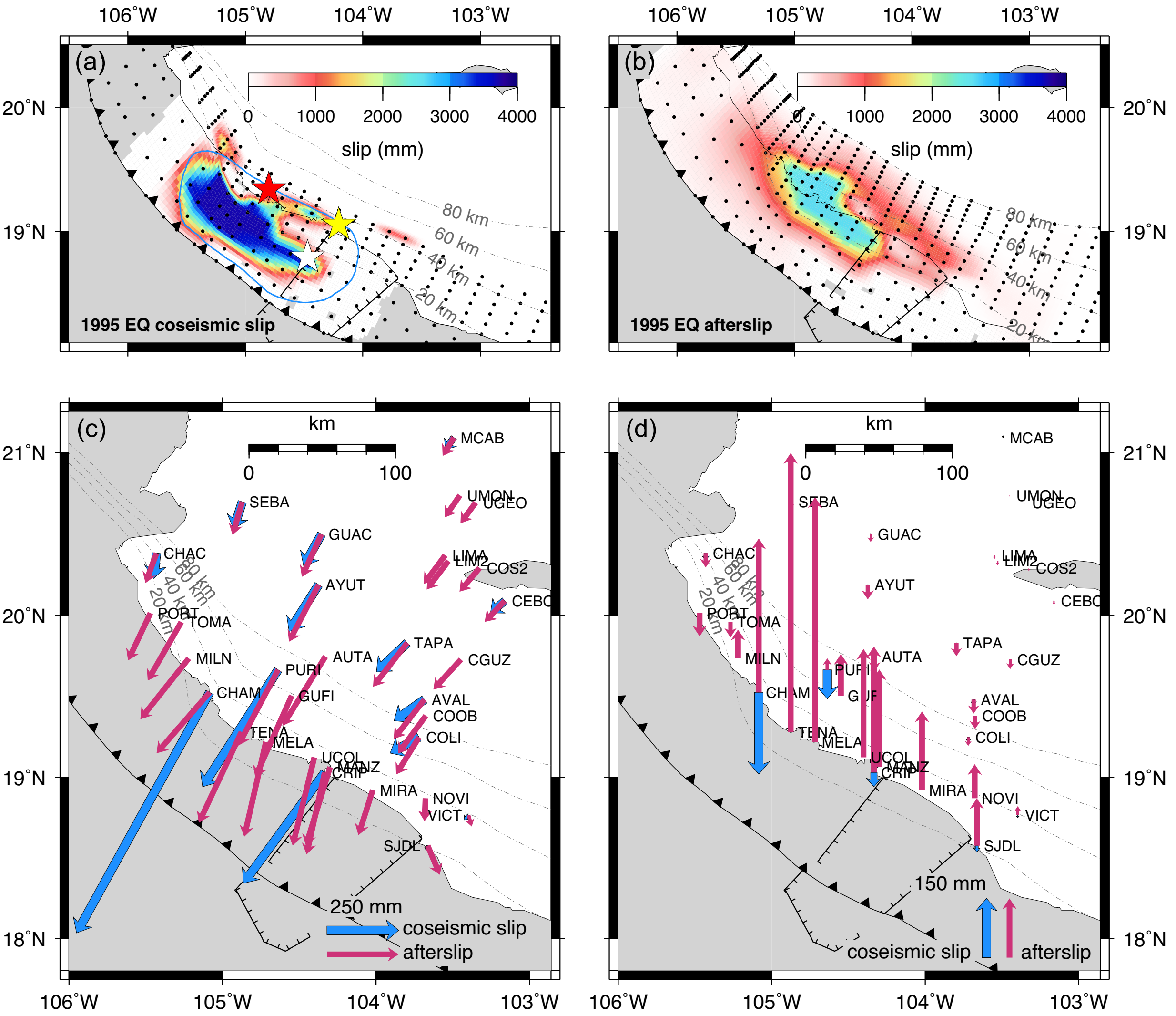

Figure 9. TDEFNODE slip solution for (a) the 1995 Colima–Jalisco earthquake and (b) its post-seismic afterslip (integrated over the 1995.77–2020.00 interval) for a model using time-series corrected for the viscoelastic effects of a mantle with $\tau_{\mathrm{m}} = 15$ yr (see the main text). EQ: earthquake. Dashed lines show the slab contours (extended from Hayes *et al.* 2012, see the main text) every 20 km. Black dots locate the fault nodes where slip is estimated. The blue line delimits the earthquake aftershock area (Pacheco *et al.* 1997). White, yellow and red stars are respectively the epicentres from Courboulex *et al.* (1997) and USGS, and the centroid from the gCMT catalogue (Dziewonski *et al.* 1997). Panels (c) and (d) respectively show the horizontal and vertical site motions predicted by the co-seismic and afterslip solutions from panels (a) and (b) at sites active during the earthquake for panel (c) and sites active between 1995 and 2003 for panel (d).

average 18.6 mm at the 23 campaign sites. The misfit F (eq. 3) for our best model is 13.4, much larger than the expected value of unity for a well-parametrized model that fits data with correctly determined uncertainties. We interpret this result as evidence that the input daily site position uncertainties, which are typically ±0.7–0.9 mm in the horizontal and ±4 mm in the vertical components, are undervalued. Several factors that may contribute to the undervalued uncertainties include neglecting likely correlations between the daily position components, our approximation of the subduction interface geometry, our simplistic homogeneous elastic half-space assumption, and the elastic properties we assumed for our model.

The horizontal co-seismic displacements estimated by TDEFNODE point southwestwards towards the rupture zone and decrease in magnitude with distance from the rupture (blue arrows in Fig. 9c). Co-seismic subsidence is predicted at most sites, decreasing with distance from the large slip areas and transitioning to minor uplift at distances more than 170 km inland from the coast (blue arrows in Fig. 9d). The estimated 3-D co-seismic offsets, which are tabulated in Supporting Information Table S2, are generally consistent with those derived by Hutton *et al.* (2001; Supporting Information Fig. S6).

Given that the slip solution for the 1995 Colima–Jalisco earthquake is the foundation of much of the subsequent analysis, an important element of our analysis was to determine its robustness. Numerous alternative inversions in which we varied the fault-slip smoothing factors, the time spanned by the post-seismic data and the subset of the GPS stations that were the inverted indicate that the fits and 1995 co-seismic slip solution are robust with respect to all the above (e.g. Supporting Information Fig. S7). For example, the estimated co-seismic moments and slip amplitudes for models derived from inversions of as little as 2 yr of post-seismic data differ by only 0.1–2.3 per cent from those for the preferred model and by only 1.8–5.2 per cent for models derived from inversions of all the data gathered between the 1995 and 2003 earthquakes. Inverting the

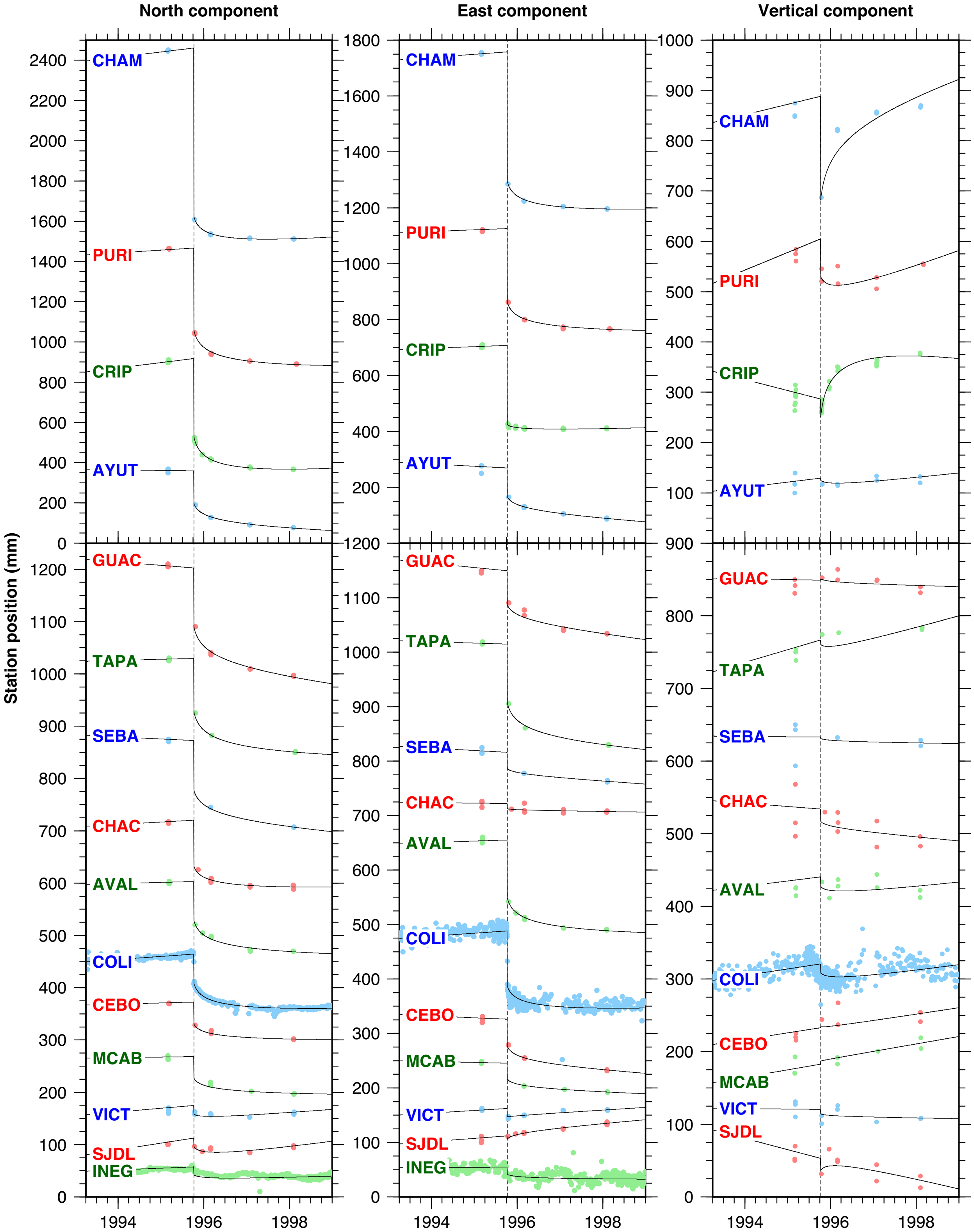

Figure 10. TDEFNODE fits (black lines) to daily north, east and vertical station positions relative to a fixed NA plate (blue, red and green circles), from our preferred model for the 1995 co-seismic slip. Intercepts are arbitrary. Dashed vertical lines mark the time of the earthquake. Only stations that where operating during the earthquake are shown.

position time-series only for the sites with data from before and after the 1995 earthquake changes the estimated co-seismic moment and slip amplitude by 1.3 per cent and 2.4 per cent, respectively.

5.2 Viscoelastic deformation from the 1995 Colima–Jalisco earthquake

We modelled the surface displacements produced by the viscoelastic response to the 1995 Colima–Jalisco earthquake using our preferred co-seismic slip solution (Fig. 9a) and assumed mantle Maxwell times τ_m of 2.5, 4, 8, 15, 25 and 40 yr (equivalent to viscosities η of 3.16×10^{18}, 5.05×10^{18}, 1.01×10^{19}, 1.89×10^{19}, 3.16×10^{19} and 5.05×10^{19} Pa s for $\mu = 40$ GPa) for the 3-D viscoelastic model described in Section 4.1. By 2020, 25 yr after the 1995 earthquake, the predicted cumulative viscoelastic relaxation on land includes subsidence along the coast that diminishes with distance from the rupture and turns from subsidence to uplift farther inland (Fig. 11). Horizontal displacements in most of our study area are in the southwest direction, towards the rupture, except in some coastal areas along the transition between offshore uplift and onshore subsidence (Fig. 11). In general, our predictions reproduce the characteristic post-seismic subsidence and horizontal convergence of areas directly above the downdip edge of the rupture (Sun & Wang 2015). At a given location, the magnitudes of the displacements predicted by models that assume values for τ_m of 2.5, 15 and 40 yr vary by factors of 2 to 5 (Fig. 12), increasing for models with shorter τ_m (i.e. lower viscosities). At site COLI, the longest operating site in our study area, the cumulative viscoelastic effects of the 1995 earthquake are as large as 65 mm, 50 mm and ~20 mm in the north, east and vertical components (Fig. 13).

We evaluated the robustness of the viscoelastic predictions to plausible variations in the 1995 co-seismic slip solutions as follows. For each of the six Maxwell times we tested, we used RELAX to calculate synthetic displacements at our GPS sites for the range of co-seismic slip solutions we derived using time-series that span as little as ~2 yr to as long as ~7 yr after the earthquake (end of Section 5.1). For models with the largest assumed Maxwell time ($\tau_\mathrm{m} = 40$ yr), the differences in the magnitudes of the cumulative viscoelastic deformation 25 yr after the earthquake predicted by the different co-seismic slip solutions were smaller than 25 mm or equivalently 1 mm yr^{-1}. For models with the shortest assumed Maxwell time ($\tau_\mathrm{m} = 2.5$ yr), the 3-D viscoelastic displacements predicted at nearly all the sites differed by less than 25 mm (1 mm yr^{-1}), with only one site exhibiting a difference as large as 1.5 mm yr^{-1}. The sites with the largest differences are located along the coast close to the rupture area, where the predicted viscoelastic deformation is sensitive to small variations in the estimated co-seismic slip. Our results indicate that uncertainties in the 1995 co-seismic slip solution and differences in the Maxwell times we use for our modelling are unlikely to cause systematic biases that are larger than 1 mm yr^{-1} in the long-term interseismic site velocities. Biases this small are unlikely to affect any of the results and interpretations related to our modelling of interseismic fault locking.

5.3 Co-seismic slip solutions for the 2003 Tecomán earthquake

We estimated a co-seismic slip solution for the 2003 Tecomán subduction earthquake for each of the six viscoelastic models that are described in the previous section. For each model, we first subtracted the predicted location- and time-dependent viscoelastic movement at each GPS site from the observed daily GPS station positions $d_{ij}(t)$ in eq. (2). We then inverted the corrected GPS position time-series via TDEFNODE while fixing the 1995 co-seismic slip solution to the same preferred estimate as was used to drive the viscoelastic model (Fig. 9a).

We evaluated the sensitivity of the 2003 co-seismic slip solutions to the length of the post-seismic interval spanned by our data, ranging from as little as ~0.5 yr to as long as ~4.5 yr after the 2003 Tecomán earthquake for each of the six corrected data sets. Supporting Information Fig. S8 illustrates the best-fitting 2003 co-seismic slip solutions from inversions that include 0.5 to 4.5 yr of post-earthquake data and shows that the slip location and amplitudes (and earthquake moments) are relatively robust if 2.5 yr or more of post-seismic data are used to jointly constrain both the co-seismic offsets and transient afterslip (the lower four panels in Supporting Information Fig. S8 are derived using 2.5 yr or more of observations after the January 22, 2003 earthquake). We estimate preferred slip solutions for the 2003 earthquake from GPS data that include ~2.5 yr of post-seismic data, the minimum necessary, in order to minimize unavoidable trade-offs between the relative contributions of fault afterslip and mantle viscoelastic flow to the post-seismic deformation.

The six preferred time-dependent models for 1993.28 to 2005.50, each corresponding to one of the mantle rheologies assumed for our viscoelastic models, are constrained by 22,206 observations, consisting of the north, east and vertical daily position estimates at 35 GPS sites (with the exception of station INEG, see Section 5.1). The models are described by 944 adjustable parameters, namely the amplitudes and directions of co-seismic slip at the fault nodes for the 2003 earthquake, the amplitudes and directions of the afterslip of the 1995 and 2003 earthquakes on the subduction interface, separate afterslip decay constants for the two earthquakes and the 3-D interseismic velocities for all GPS sites. Results for all six of the 2003 Tecomán earthquake co-seismic solutions, one for each of the six viscoelastic models we explored, are displayed and tabulated in Supporting Information Fig. S9 and Tables S3 and S4. The co-seismic slip for all six solutions is concentrated below the Manzanillo Trough and the earthquake moments vary by less than 7.6 per cent relative to an average M_o of $1.98 \pm 0.07 \times 10^{20}$ N m for all six models (Supporting Information Table S4), corresponding to $M_\mathrm{w} = 7.4$–7.5. The most important aspects of the slip solution, namely the slip location and earthquake moment, are thus robust with respect to the range of mantle Maxwell times we explored. Below, we describe in more detail our results for the slip solution for a mantle with $\tau_\mathrm{m} = 15$ yr (corresponding to a mantle viscosity of 1.89×10^{19} Pa s).

Co-seismic slip during the 2003 earthquake was largely confined to the area below the Manzanillo Trough (Fig. 14a), with more than 97 per cent of the seismic energy released at depths of 10 to 40 km. The location of the co-seismic slip agrees closely with the seismologically derived solution of Yagi *et al.* (2004; shown by the red lines in Fig. 14a) and also agrees with the seismologic slip solution of Quintanar *et al.* (2010) and GPS-derived solution of Schmitt *et al.* (2007). The rupture encompasses the gCMT earthquake centroid (Ekström *et al.* 2004), and epicentres estimated by Yagi *et al.* (2004) and the USGS (stars in Fig. 14a). Our geodetically derived co-seismic moment, 1.84×10^{20} N m ($M_\mathrm{w} = 7.4$), is close to seismologic estimates of $M_\mathrm{o} = 2.0 \times 10^{20}$ N m (Ekström *et al.* 2004), 2.3×10^{20} N m (Yagi *et al.* 2004) and 1.88×10^{20} N m (Quintanar *et al.* 2010). This result also agrees with the geodetic solution of Schmitt *et al.* (2007), who estimate a seismic potency of 5.1×10^9 m^3, only 10 per cent different from the potency found in this

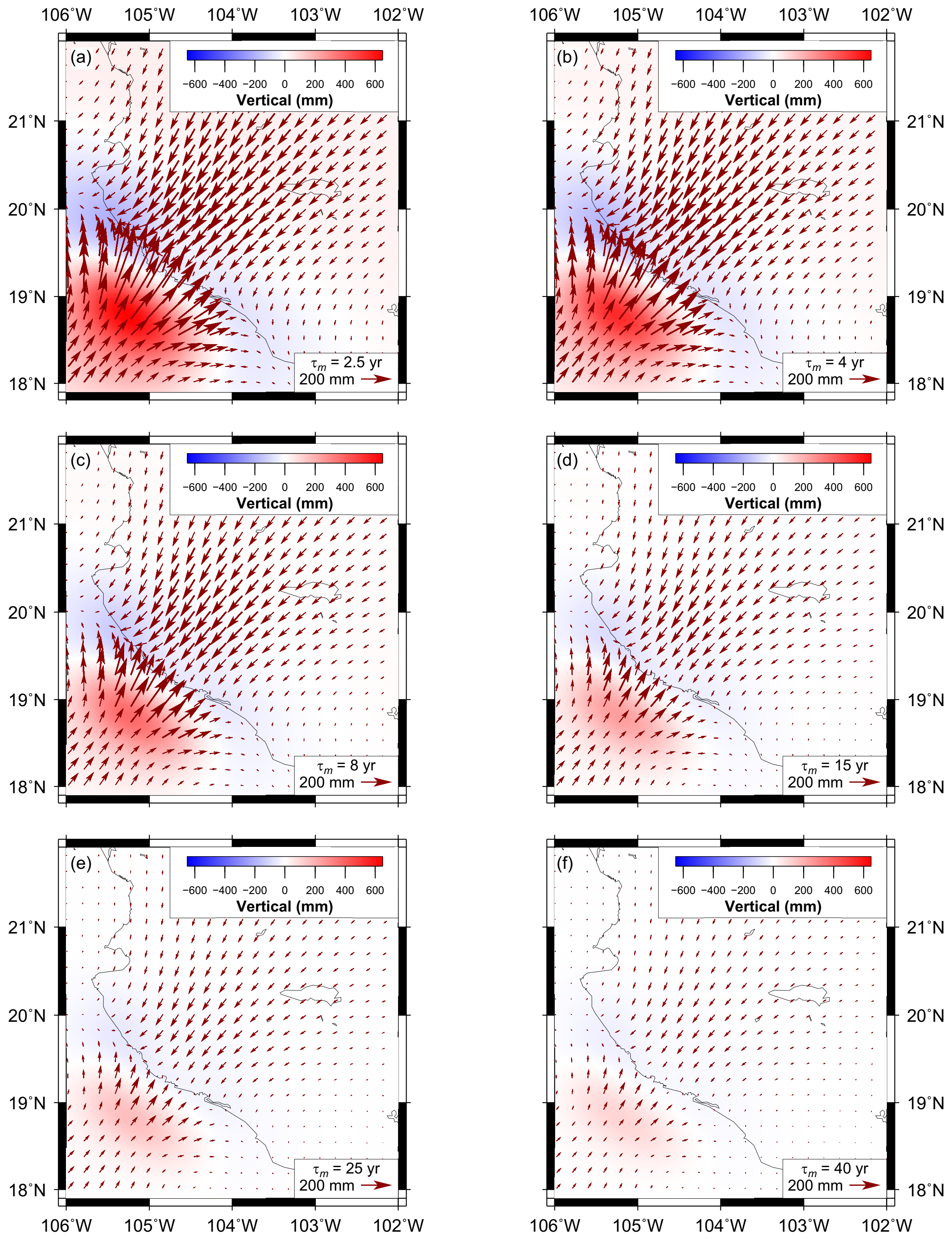

Figure 11. Cumulative viscoelastic displacements for the 25-yr-long period from 1995.77 to 2020.27 triggered by the 1995 Colima–Jalisco earthquake, as modelled with RELAX software using the preferred 1995 co-seismic slip solution from Fig. 9(a). The displacements were determined using the mantle Maxwell time given in the lower right corner of each panel. Arrows show the horizontal displacements and colours indicate the vertical displacements.

study (4.60×10^9 m^3). The potency of the Yagi *et al.* (2004) seismic solution, 4.7×10^9 m^3 (Schmitt *et al.* 2007), differs by only 2 per cent from our estimate.

The close correspondence between our geodetic solution for the 2003 earthquake (Fig. 14a) and the seismologic slip solutions referenced above is reinforced by the checkerboard test most applicable for the 2003 earthquake (Supporting Information Fig. S4). Except for the uppermost 5 km of the subduction interface, where any slip is poorly resolved, the imposed variations in the interface locking are well recovered (compare the lower two and upper two panels

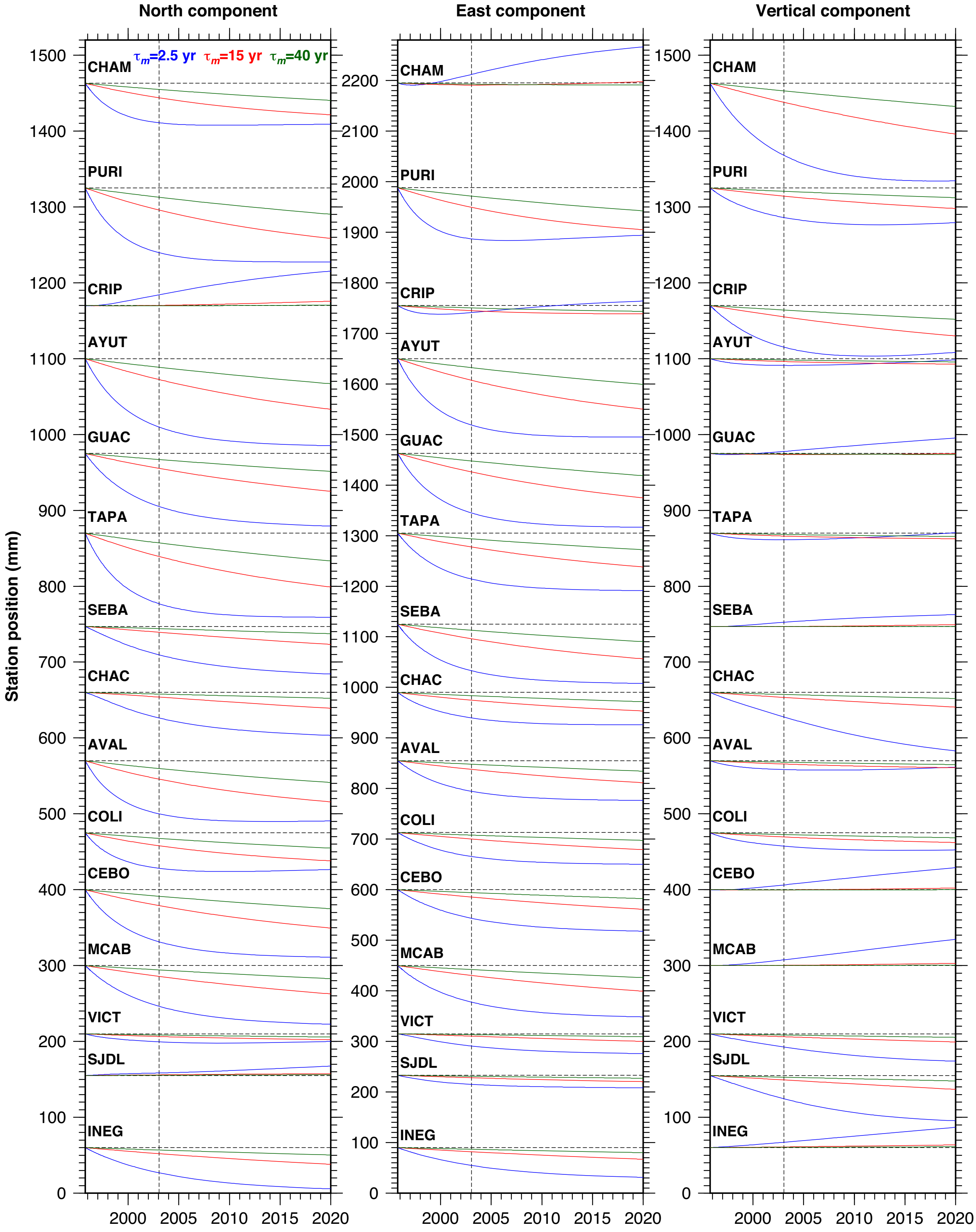

Figure 12. Modelled viscoelastic deformation for the 1995 Colima–Jalisco earthquake at GPS sites active during the earthquake for mantle rheologies corresponding to Maxwell times of 2.5 (blue), 15 (red) and 40 yr (green). The dashed vertical lines mark the time of the 2003 Tecomán earthquake.

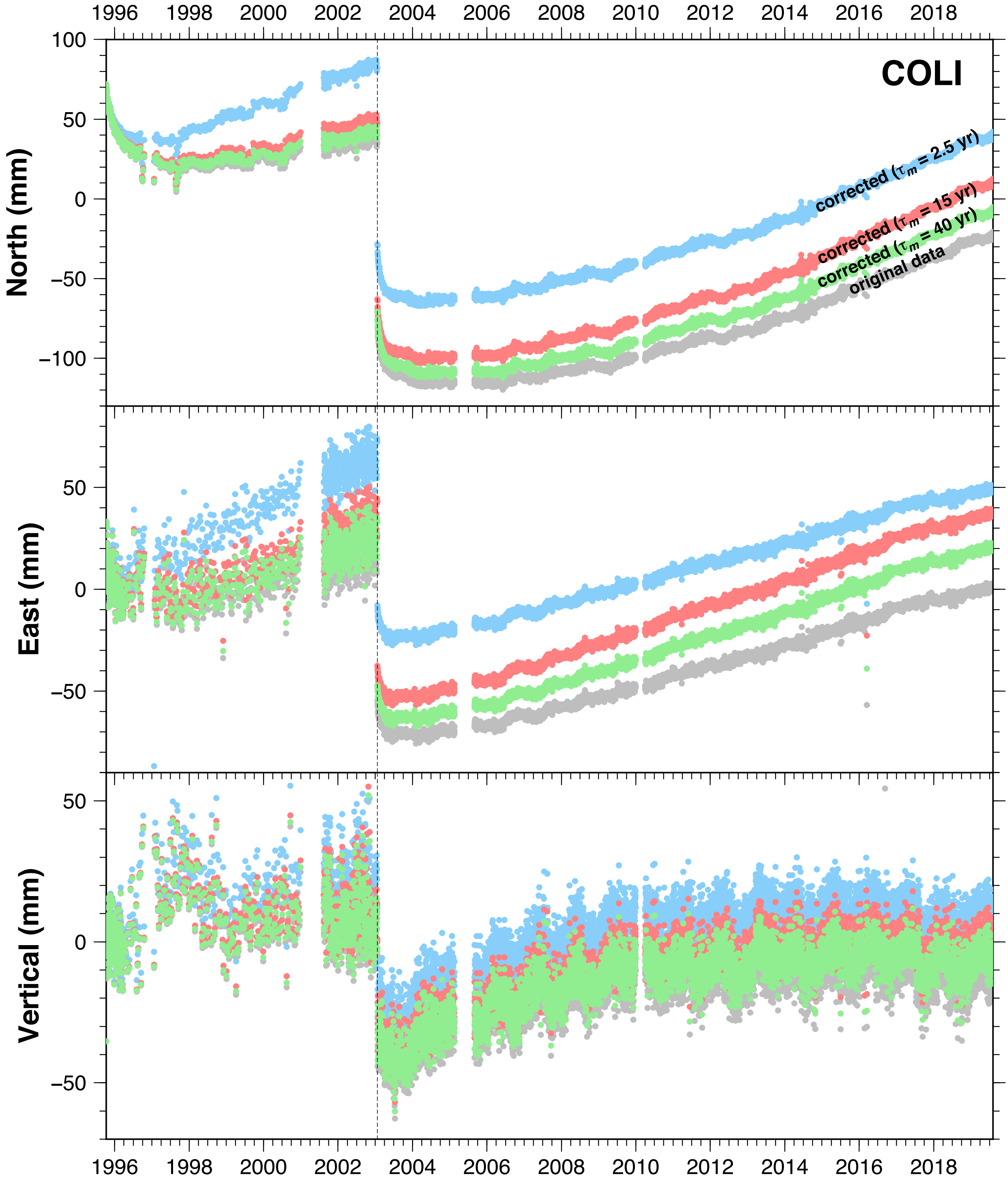

Figure 13. Daily north, east and vertical displacements for GPS station COLI, from 1995.77 to 2019.50. Grey dots correspond to the original time-series. Blue, red and green dots correspond to the corrected time-series for the 1995 earthquake viscoelastic deformation models using $\tau_{\mathrm{m}} = 2.5$, 15 and 40 yr, respectively. The black dashed line marks the time of the 2003 Tecomán earthquake.

in Supporting Information Fig. S4). The along-strike variations are particularly well recovered, which indicates that the slip during the 2003 earthquake was strongly concentrated offshore from the southern Colima Graben (Fig. 14a), at the southeastern limit of the 1995 rupture zone (Fig. 9a).

The fits of the time-dependent model with $\tau_{\mathrm{m}} = 15$ yr are good overall (Fig. 15), with wrms misfits of 1.6–2.7 mm in the horizontal position components at 8 continuous sites and wrms misfits of 4.0–4.5 mm at the 27 campaign GPS sites. The wrms misfits to the noisier vertical daily positions are 8.6 mm at 7 continuous sites and

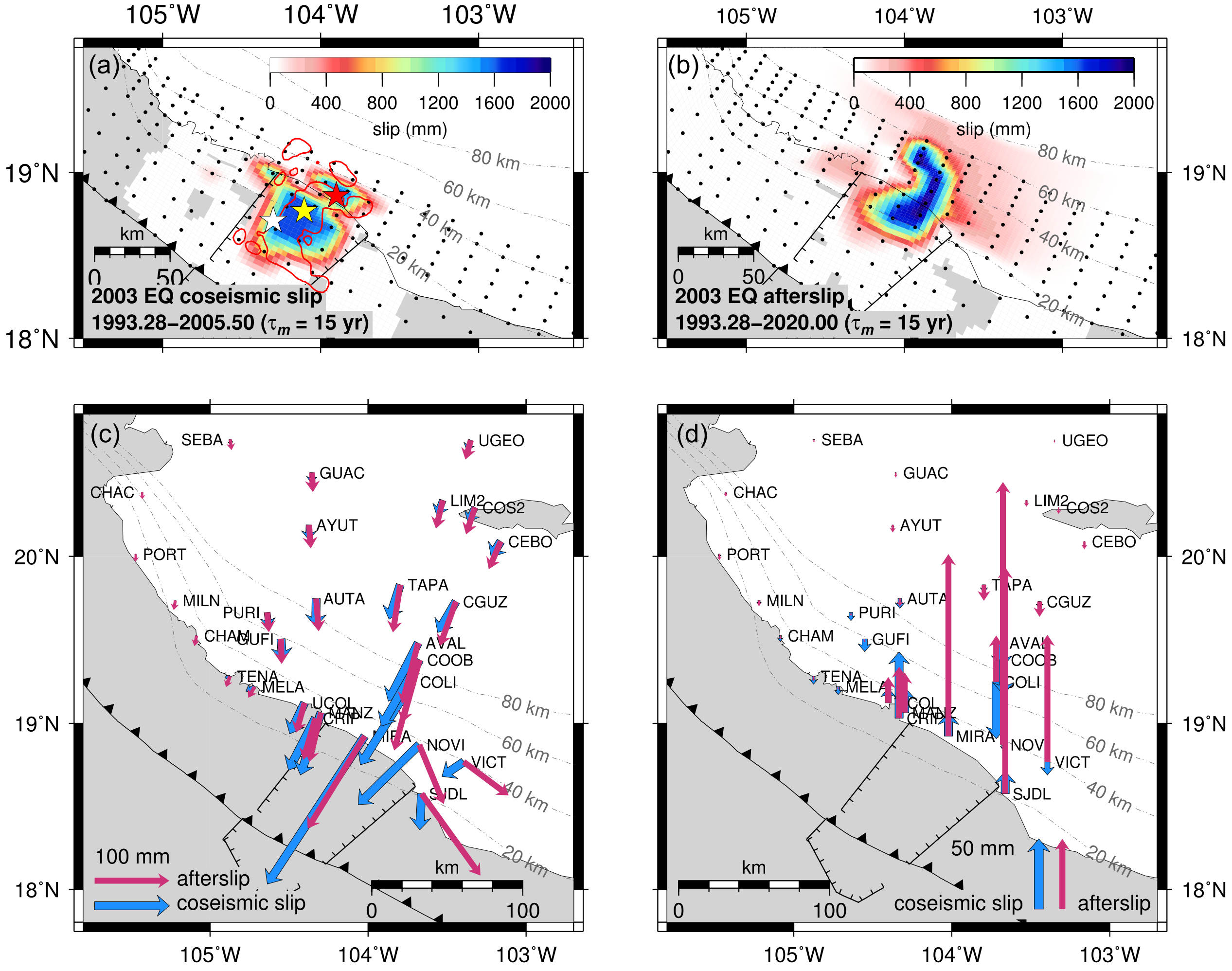

Figure 14. TDEFNODE slip solution for (a) the 2003 Tecomán earthquake and (b) its post-seismic afterslip (integrated over the 2003.06–2020.00 interval) for a model using time-series corrected for the viscoelastic effects of a mantle with $\tau_m = 15$ yr. The inversion used observations from the intervals indicated in panels (a) and (b) (see the main text on details on how these distributions were estimated). EQ: earthquake. Dashed lines show the slab contours every 20 km. Black dots locate the fault nodes where slip is estimated. The red line delimits the rupture area for the earthquake (Yagi *et al.* 2004). White, yellow and red stars are the epicentres from Yagi *et al.* (2004) and USGS, and the centroid from the gCMT catalogue (Ekström *et al.* 2004), respectively. Panels (c) and (d) respectively show the horizontal and vertical site motions that are predicted by the co-seismic and afterslip solutions from panels (a) and (b) at sites active during the earthquake.

10.7 mm at the 27 campaign sites. Misfit F for this model is 11.9, similar to that of the 1995 earthquake ($F = 13.4$). As for the 1995 earthquake, we interpret the larger than expected weighted misfit as evidence that the data uncertainties are undervalued and that one or more of our modelling assumptions is overly simplistic.

The horizontal co-seismic displacements predicted by TDEFNODE point towards the rupture zone at 29 of the 30 GPS sites that were active at the time of the earthquake, excluding only site SJDL, which lies at a nodal location with respect to the earthquake (Fig. 14c and Supporting Information Table S4). Co-seismic subsidence is predicted at most sites (Fig. 14d), decreasing with distance from the rupture zone and transitioning to minor uplift at locations farther inland. Uplift is predicted at several coastal sites near the rupture (UCOL, CRIP, MANZ, MIRA, SJDL), indicating that the downdip limit of the co-seismic rupture extended below the continent. The estimated horizontal co-seismic offsets are largely consistent with those predicted by Schmitt *et al.* (2007) but differ at some locations in the vertical component (Supporting Information Fig. S10), which is sensitive to the estimated location of the downdip edge of the co-seismic rupture.

5.4 Viscoelastic deformation from the 2003 Tecomán earthquake

We modelled surface displacements produced by the viscoelastic response to the 2003 Tecomán earthquake for all six co-seismic slip solutions (Supporting Information Fig. S9) using their corresponding mantle Maxwell times ($\tau_m = 2.5$, 4, 8, 15, 25 and 40 yr). Viscoelastic relaxation due to the 2003 earthquake (Fig. 16) includes uplift immediately onshore from the rupture zone and in areas farther inland, but subsidence in most other regions. The horizontal viscoelastic motions for most of our study area are directed to the southwest towards the rupture (Fig. 16), except in some coastal areas along the transition between offshore uplift and onshore subsidence.

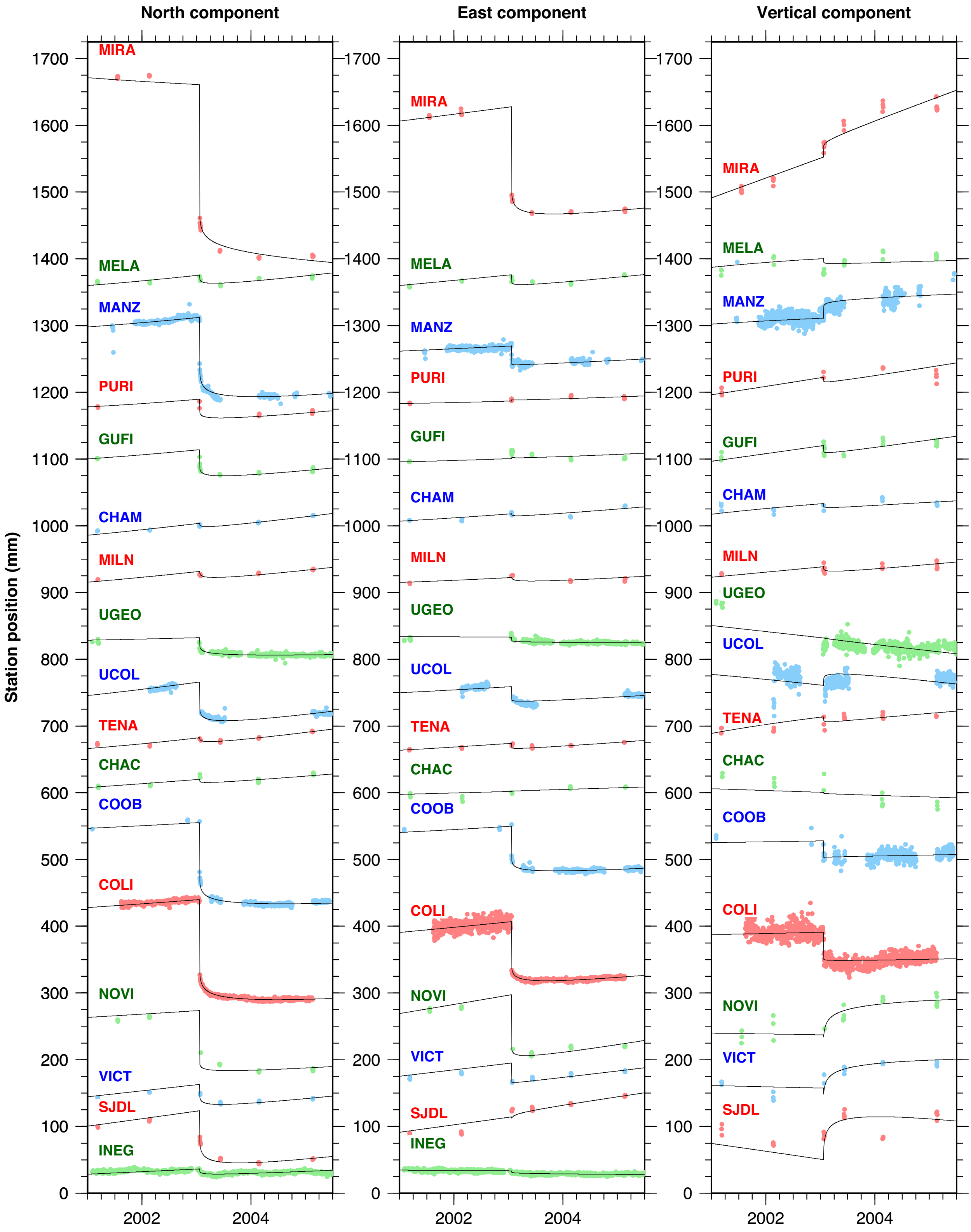

Figure 15. TDEFNODE fits (black lines) to daily north, east and vertical station positions (blue, red and green dots) relative to a fixed NA plate for selected stations with observations spanning the 2003 Tecomán earthquake. Intercepts are arbitrary. The data set has been corrected for the viscoelastic effects of the 1995 Colima–Jalisco earthquake using $\tau_m = 15$ yr for the mantle.

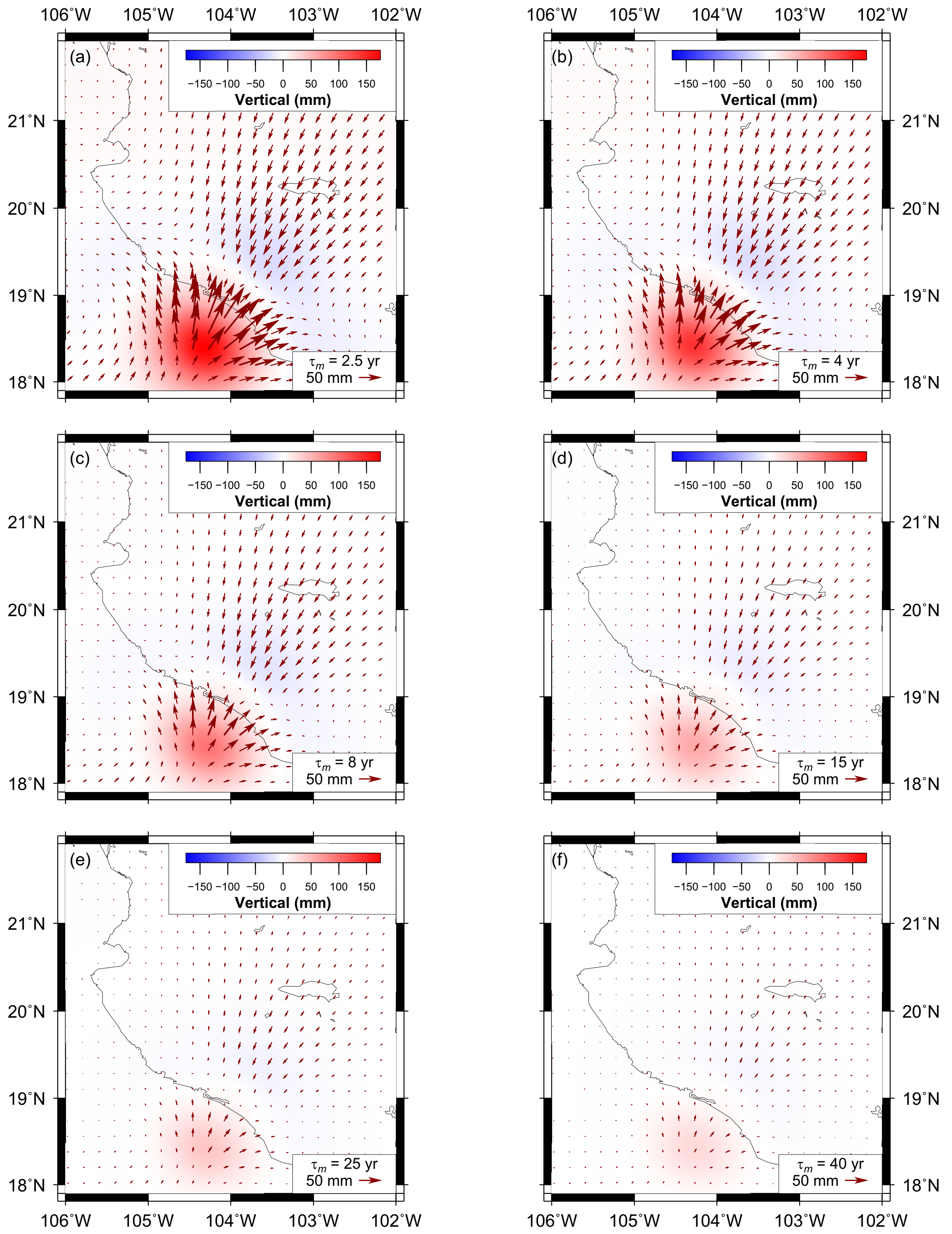

Figure 16. Cumulative viscoelastic displacements for the ∼17-yr-long period 2003.06 to 2020.25 triggered by the 2003 Tecomán earthquake, as modelled with RELAX software using our preferred 2003 co-seismic slip solutions. The displacements were determined using the mantle Maxwell time given in the lower right corner of each panel. Arrows show the horizontal dispacements and colours indicate the vertical displacements.

Supporting Information Fig. S11 shows the modelled displacements at selected sites.

The viscoelastic motions predicted for the 2003 Tecomán earthquake differ from the viscoelastic deformation triggered by the 1995 Colima–Jalisco earthquake in two notable respects. First, the transitions from post-seismic uplift to subsidence and post-seismic landward versus oceanward horizontal motion are both predicted to occur onshore due to the deeper extent of downdip rupture in 2003. Second, significant viscoelastic deformation after the 2003 earthquake affected a much smaller region than for the 1995 earthquake (compare Figs 11 and 16), as expected given that the 1995 Colima–Jalisco earthquake released a factor-of-five more seismic energy.

The combined viscoelastic effects of the 1995 and 2003 earthquakes for the 25-yr interval spanned by our study constitute a non-negligible fraction of the overall deformation within our study area during the past few decades. Supporting Information Figs S12 and S13 show the combined surface effects over the study area and at selected sites, respectively. At site COLI, the combined viscoelastic effects of the two earthquakes by mid-2020 were as large as 75 mm, 55 mm and 35 mm in the north, east and vertical components (Supporting Information Fig. S14). We estimate that site COLI's steady interseismic movement for the same interval was ∼171 mm and ∼178 mm to the north and east, respectively, based on 10 ± 2.5 mm yr^{-1} of N46° E-directed interseismic elastic shortening measured at COLI from ∼2.5 yr of continuous measurements prior to the 1995 Colima–Jalisco earthquake (Marquez-Azua *et al.* 2002). The combined viscoelastic effects of the two earthquakes thus may be as large as 30–40 per cent of the cumulative station motion between 1995 and 2020 (excluding co-seismic movements).

5.5 Afterslip solutions: 1995 Colima–Jalisco and 2003 Tecomán earthquakes

From TDEFNODE inversions of the north, east and vertical daily position estimates at 62 GPS sites, consisting of 201,506 observations between 1993 and 2020, we estimated afterslip solutions for the 1995 Colima–Jalisco and 2003 Tecomán earthquakes and the 3D interseismic site-velocities (Section 5.6). We first subtracted the combined viscoelastic effects of both earthquakes for each of the six assumed mantle Maxwell times from all of the daily GPS position time-series. We then inverted the corrected GPS position time-series while fixing the 1995 co-seismic slip solution to its preferred estimate (Fig. 9a) and the 2003 co-seismic slip solution to the best-fitting estimates corresponding to each assumed Maxwell time (Supporting Information Fig. S9). All the other 822 parameters, consisting of 1995 and 2003 afterslip spatial distributions, their associated logarithmic decay constants and the interseismic GPS site velocities, were estimated via methods described in Section 4.2. The vertical components at continuous stations INEG, CUVA, UAGU and TNZA were all discarded due to non-tectonic subsidence at each site that we attribute to groundwater withdrawal. Figs 9(b) and 14(b) respectively show the best-fitting 1995 and 2003 earthquake afterslip solutions derived from the GPS positions that were corrected by the representative $\tau_\mathrm{m} = 15$ yr viscoelastic model. Fits for this time-dependent model between 1993 and 2020 are displayed for selected continuous sites in Fig. 17 and selected campaign sites in Fig. 18. The wrms misfits range from 1.9 to 4.9 mm in the horizontal components at the 36 continuous sites and 5.0–5.1 mm at the 26 campaign sites. F for this model is 14.4, larger than F for the inversions of data that span shorter periods (e.g. Section 5.3). We attribute the larger misfit to a combination of factors: the sensitivity of the fit to the assumed mantle Maxwell time, our assumption of a Newtonian mantle rheology and our simple single-layer, linear viscoelastic model. The larger wrms misfits to the campaign site time-series (5.0–5.1 mm for the horizontal components and 13.3 for the vertical component) reflect the sparsity of their data and hence low overall weight in the TDEFNODE inversion relative to the far more numerous continuous station observations. Because many more campaign than continuous sites were operating during the early years of this study, when rapid post-seismic deformation after the 1995 Colima–Jalisco earthquake occurred, we favoured the models that best fit the early campaign observations.

5.5.1 *1995 Colima–Jalisco earthquake afterslip*

The TDEFNODE inversion of the 1993–2020 GPS data corrected for viscoelastic deformation for $\tau_\mathrm{m} = 15$ yr indicates that more than 85 per cent of the 1995 afterslip moment occurred at depths below 15 km, downdip from the co-seismic rupture zone (Fig. 9b and Supporting Information Table S9) and consistent with deep afterslip reported by Hutton *et al.* (2001). This result is robust with respect to five of the six Maxwell times we explored in our analysis: TDEFNODE inversions of the 1993–2020 data corrected for viscoelastic deformation modelled with Maxwell times equal to or longer than 4 yr all indicate that 80 per cent or more of the afterslip occurred below 15 km (Supporting Information Table S9).

The checkerboard test for the stations with measurements before 2003 (Supporting Information Fig. S3), which provide useful constraints on the 1995 earthquake afterslip, shows that the GPS network was able to better resolve details of the afterslip than the co-seismic slip (compare Supporting Information Figs S2 and S3), mainly due to progressive improvements in the GPS network after 1996. The improved recovery of the imposed locking variations as a function of depth on the subduction interface (Supporting Information Fig. S3) suggests that the apparent occurrence of afterslip 10–20 km farther downdip on the JCSZ interface than the co-seismic slip (compare Figs 9a and b) is real rather than an artefact of the inversion.

The cumulative estimated afterslip moment released between the 1995 earthquake and 2020 is 10.8×10^{20} N m ($M_\mathrm{w} = 8.0$), equivalent to ∼110 per cent of the co-seismic moment release (Supporting Information Table S5). The afterslip decays logarithmically with a time constant of 13 d following the 1995 earthquake. During the first ∼3.5 yr after the earthquake, afterslip released an equivalent of ∼80 per cent of the co-seismic moment, comparable to the afterslip versus co-seismic moment release ratio of 70 per cent reported by Hutton *et al.* (2001) for the same period.

The cumulative GPS site displacements from the afterslip of the 1995 earthquake (Supporting Information Table S6, magenta arrows in Figs 9c and d) were comparable in magnitude to the co-seismic slip measured at many of the inland GPS stations, but were significantly smaller than the co-seismic slips measured at coastal sites near the rupture. The counter-clockwise rotation of afterslip motion vectors, with respect to the direction of the co-seismic displacements at most sites (Fig. 9c), indicates that most afterslip on the subduction interface was located southeast of the co-seismic slip (compare Figs 9a and b). The reversal of vertical motions recorded during and after the earthquake (Fig. 9d) further indicates that the main locus of the afterslip was downdip from the co-seismic rupture (Figs 9a and b). Both features of our 1995 afterslip model (i.e. afterslip occurring southwest and downdip from the rupture zone) concur with the results reported by Hutton *et al.* (2001) from their modelling of the first few years of post-seismic data, and with the results from Marquez-Azua *et al.* (2002) from their modelling of continuous measurements at site COLI.

5.5.2 *2003 Tecomán earthquake afterslip*

The same TDEFNODE inversion indicates that afterslip from the 2003 earthquake was concentrated primarily along and directly downdip from the 2003 earthquake rupture zone (Fig. 14b). No previous afterslip solution for this earthquake has been estimated, although Schmitt *et al.* (2007) speculated that the afterslip in 2003 occurred at a downdip location based on an observed reversal in the sense of the co-seismic and post-seismic vertical movements at two coastal sites in the days after the earthquake.

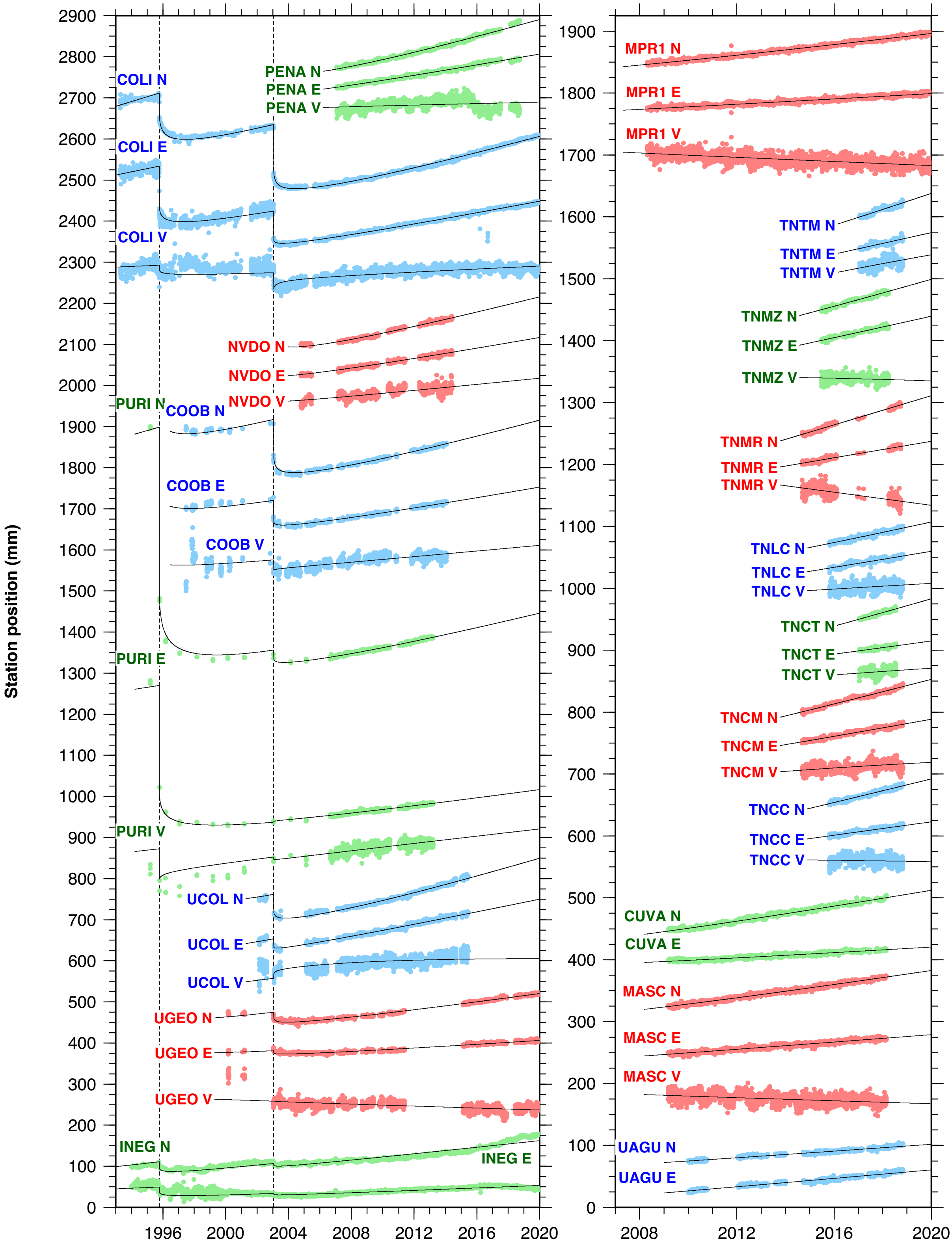

Figure 17. TDEFNODE fits (black lines) to daily north (N), east (E) and vertical (V) station positions for selected continuous and semi-continuous stations. Intercepts are arbitrary. The data set has been corrected for the viscoelastic effects of the 1995 Colima–Jalisco and the 2003 Tecomán earthquakes using $\tau_m =$ 15 yr for the mantle.

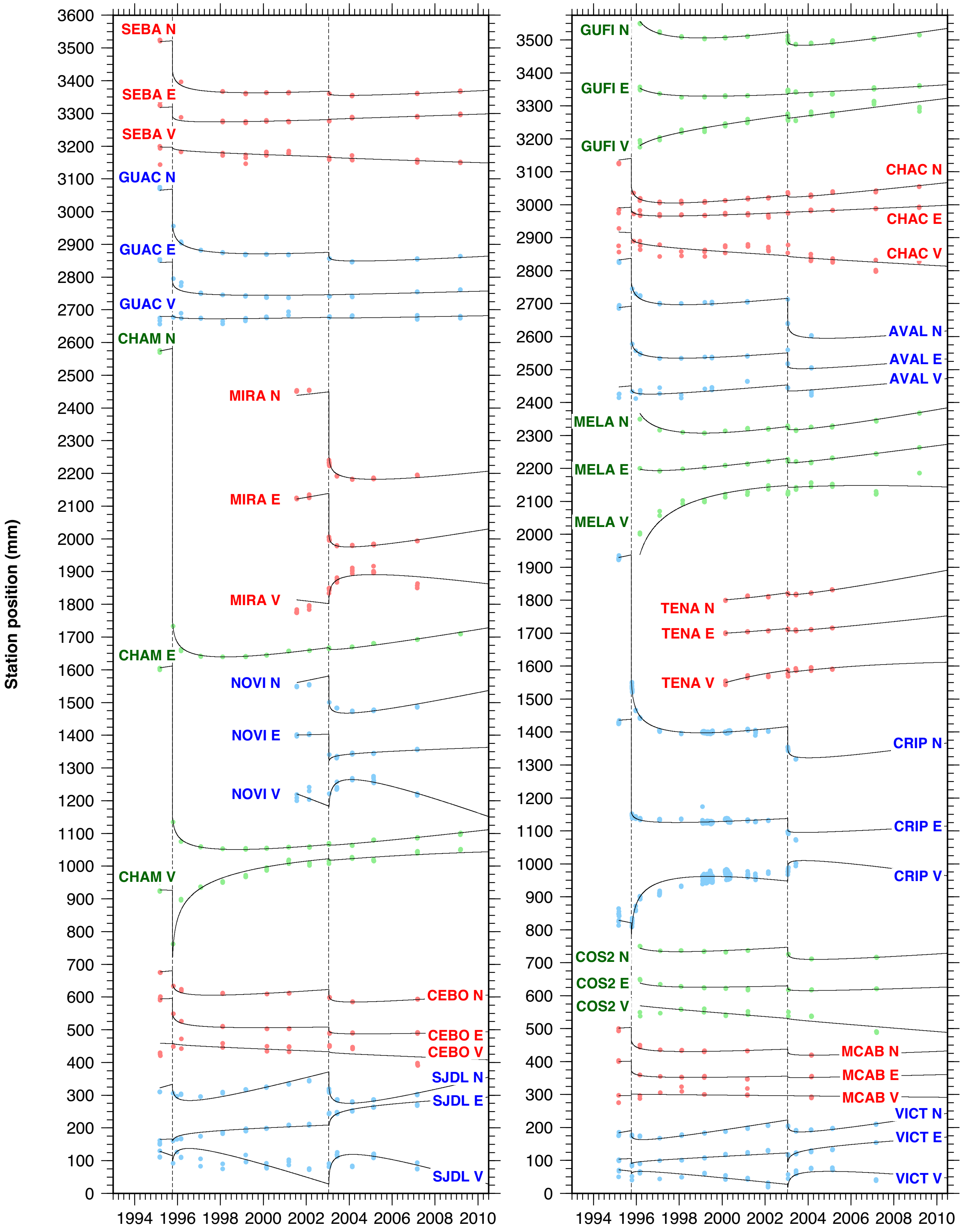

Figure 18. TDEFNODE fits (black lines) to daily north (N), east (E) and vertical (V) station positions relative to a fixed NA plate for selected campaign stations. The data set has been corrected for the viscoelastic effects of the 1995 Colima–Jalisco and the 2003 Tecomán earthquakes using $\tau_m = 15$ yr for the mantle.

The principal difference between the 2003 earthquake co-seismic and afterslip solutions (Figs 14a and b, respectively) is that the latter is located 10–20 km farther downdip than the former. Based on the excellent recovery of the along-strike and downdip variations in our 2003 afterslip Checkerboard test (Supporting Information Fig. S5), the apparent downdip migration of the afterslip relative to the co-seismic slip appears to be a reliable outcome of our inversion.

The cumulative afterslip moment estimated at 2.8×10^{20} N m ($M_w = 7.6$) is $\sim$1.5 times larger than the co-seismic moment. Whereas $\sim$85 per cent of the afterslip energy was released at depths of 15–60 km (Fig. 14c and Supporting Information Table S7), $\sim$5 km farther downdip from the region of co-seismic slip (Fig. 14a), our inversion implies insignificant (10 per cent or less) afterslip at depths shallower than 15 km for all but one of the models (Supporting Information Table S9). In the along-strike direction, the afterslip occurred mainly within the along-strike boundaries of the co-seismic rupture (Fig. 14). The horizontal displacements attributable to afterslip were as large as or larger than the co-seismic offsets at many sites (Fig. 14c and Supporting Information Table S8), particularly at inland locations. This result, and the reversal of vertical motions with respect to the co-seismic direction, strongly indicate that the fault afterslip was focused downdip of the co-seismic rupture (compare Figs 14a and b). The vertical displacements associated with afterslip transition from uplift onshore from the rupture to minor subsidence at sites father inland (Fig. 14d).

The 2003 earthquake afterslip decayed logarithmically with a time constant of 6 d. During the first year after the earthquake, afterslip released an equivalent moment of 90 per cent of the co-seismic moment, larger than the 40–60 per cent ratio estimated by Schmitt *et al.* (2007) for the same interval from the early post-seismic motions at just two sites.

Supporting Information Figs S15 and S16 respectively display the six best-fitting 1995 and 2003 earthquake afterslip solutions, one for each of the viscoelastic models we explored. Tables S5-S9 provide relevant information for all the models. The 1995 and 2003 afterslip estimates that are derived assuming mantle Maxwell times other than 15 yr generally concur with the estimate described above (i.e. for $\tau_m = 15$ yr) and are thus not discussed further.

5.6 The interseismic velocity field

Fig. 19 displays GPS site velocities from the TDEFNODE inversion (i.e. V_{ij} in eq. (2) of Section 4.2) with viscoelastic corrections for a mantle Maxwell time of 15 yr. Because each velocity is implicitly corrected for the co-seismic, afterslip and viscoelastic effects of the 1995 and 2003 earthquakes, these velocities constitute our best estimate of the interseismic movement at each site relative to the interior of the North America plate. The horizontal and vertical interseismic site velocities V_{ij} for all six assumed mantle Maxwell times are tabulated in Supporting Information Table S10. A comparison of the velocities from models with $\tau_m = 2.5$, 15 and 40 yr is shown in Supporting Information Figs S17 and S18.

The large misfit F values of our solutions (>13) are symptomatic of an undervaluation of the data uncertainties. The formal velocity uncertainties, which are estimated by TDEFNODE solely from the formal uncertainties in the inverted GPS station positions, are typically less than ± 1 mm yr^{-1}. They exclude uncertainties that are introduced by our model assumptions and viscoelastic corrections. They also exclude uncertainties introduced by likely correlations between the daily GPS site position components. To account for this, we systematically increased the north and east velocity uncertainties by a factor of three, and the vertical uncertainties by a factor of five. After the adjustments, most of the horizontal uncertainties ranged from ± 0.6–3.5 mm yr^{-1} and vertical uncertainties from ± 0.9–4 mm yr^{-1}. Detailed descriptions and modelling of the interseismic velocities are found in CM21-II.

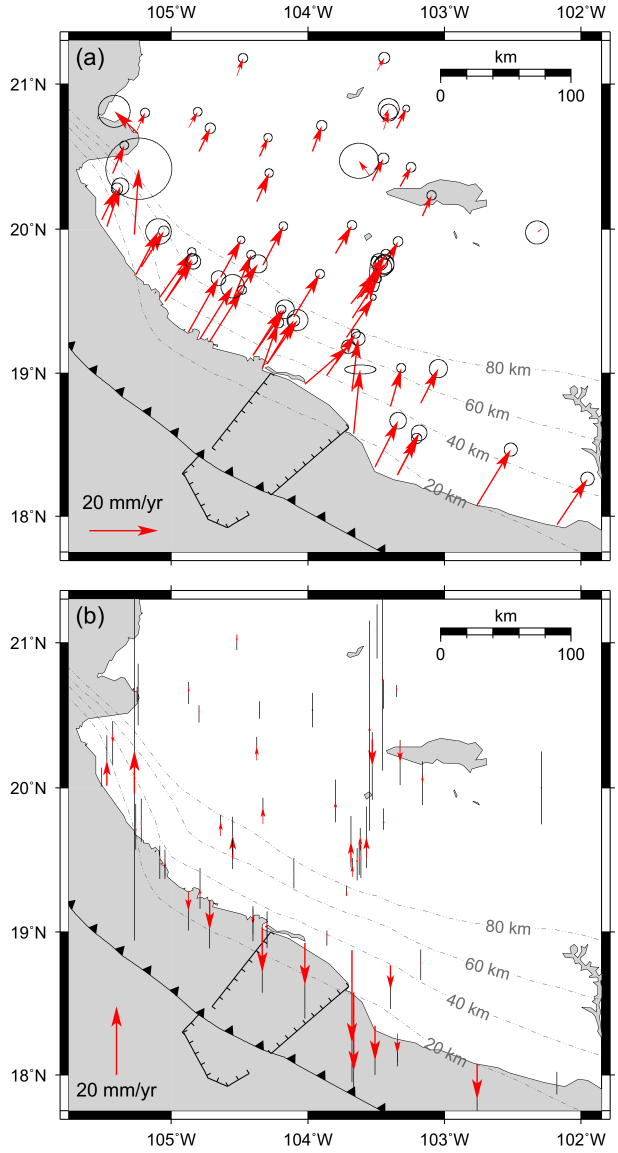

Figure 19. Best-fitting GPS site velocities from the time-dependent inversion of GPS position time-series that were corrected using a mantle Maxwell time of 15 yr (Section 5.6 and Supporting Information Table S10). (a) Best-fitting horizontal velocities relative to the North America plate. The velocity ellipses show the 2-D, 1-σ uncertainties. (b) Vertical velocities. Thin black lines represent 1-σ uncertainties.

6 DISCUSSION

6.1 Influence of assumed mantle viscosity on co-seismic and afterslip solutions

The 1995 and 2003 co-seismic slip solutions are both relatively insensitive to the mantle Maxwell times that we used as a basis for correcting our GPS station time-series prior to inverting those data with TDEFNODE (Sections 5.1 and 5.3). In contrast, the post-seismic 1995 and 2003 afterslip solutions are more sensitive to the assumed Maxwell time (Section 5.5, Supporting Information Figs S15 and S16), reflecting the trade-off between fitting post-seismic site motions with a combination of logarithmically decaying afterslip and exponentially decaying viscoelastic deformation. In general, smaller values of τ_{m} for the viscoelastic corrections, which correspond to larger magnitude short-term viscoelastic deformation, result in smaller estimated afterslip (Supporting Information Figs S15 and S16).

Previous authors have considered the same trade-off between afterslip and viscoelastic mantle/crustal responses along subduction zones. Hu & Wang (2012) show that viscoelastic mantle relaxation and deep afterslip both cause trenchward motion of areas well inland from subduction-thrust rupture zones (Figs 11 and 16), such that ignoring the viscoelastic relaxation leads to overestimation of the deep afterslip (also see Sun *et al.* 2014; Tsang *et al.* 2016; Barbot 2018; Qiu *et al.* 2018; Weiss *et al.* 2019). Similarly, post-seismic viscoelastic relaxation and shallow afterslip respectively cause landward and seaward (i.e. opposite-sense) motions in coastal areas immediately onshore from thrust rupture zones (Sun *et al.* 2014; Sun & Wang 2015; Barbot 2018; Weiss *et al.* 2019, and figs 11 and 16). Ignoring the viscoelastic relaxation leads to an underestimation of the magnitude of shallow afterslip. By implication, neglecting the post-seismic viscoelastic effects of large ($M_{\mathrm{w}} \geq 7.5$) thrust earthquakes, such as the $M_{\mathrm{w}} = 8.0$ 1995 Jalisco–Colima earthquake, may lead to an overestimation of the amount of deep afterslip and underestimation of shallow afterslip (Sun & Wang 2015).

Our modelling illustrates both of these trade-offs. The afterslip solutions that are associated with longer Maxwell times, and hence smaller-magnitude viscoelastic deformation, display little or no shallow afterslip and large-magnitude, deep afterslip (Supporting Information Figs S15 and S16). Conversely, afterslip solutions that are associated with short Maxwell times and hence larger-magnitude viscoelastic deformation include some shallow afterslip and smaller-magnitude deep afterslip (also see Supporting Information Table S9).

6.2 Implications for subduction along the northernmost Mexico subduction zone

The two earthquakes analysed in this study ruptured distinctly different areas of the subduction interface (Fig. 20). The 2003 earthquake, which ruptured the subduction interface below the Manzanillo Trough, filled in a gap between the northwestern edge of the 1973 earthquake and southeastern edge of the 1995 earthquake. Any overlap between the rupture areas for the 1995 Colima–Jalisco and 2003 Tecomán earthquakes was minimal (Fig. 20). Including the June 1932 M∼8 earthquakes, whose rupture areas are known only approximately (Fig. 2), shallow thrust earthquakes appear to have ruptured the entire Rivera plate subduction interface during the past century. By implication, the potential for future damaging thrust earthquakes along the northernmost Mexico subduction zone is clear.

Schmitt *et al.* (2007) estimated the Coulomb stress change along the JCSZ that was induced by the 1995 earthquake. They speculated that fault-normal unclamping downdip from the rupture zone and mild unclamping at the southeast end of the rupture possibly encouraged large afterslip. Our estimates of the size and location of the 1995 afterslip (orange area in Fig. 20) support this hypothesis. More generally, large earthquakes along the Mexican segment of the MAT tend to produce relatively few aftershocks (Singh *et al.* 2003), possibly indicating that afterslip rather than aftershocks are the primary means of relieving post-seismic stresses at depths below ∼35–40 km. Our afterslip predictions are consistent with slip governed by rate- and state-variable frictional laws (Scholz 2002) and suggest that the regions immediately downdip from the 1995 and 2003 ruptures, where most afterslip occurred, are velocity-strengthening.

The 1995 and 2003 earthquakes both triggered unusually large afterslip, with respective afterslip-to-earthquake moment ratios of ∼110 per cent and ∼150 per cent (Tables S5 and S7). Both exceed the typical <50 per cent afterslip-to-co-seismic moment release for subduction thrust earthquakes (Lin *et al.* 2013). Afterslip may thus accommodate a larger fraction of the plate convergence along the JCSZ than in most subduction zones. Although Lin *et al.* (2013) suggest that the relative magnitude of post-seismic-to-co-seismic moment scales with the magnitude of the main shock, we observe the converse: the 2003 Tecomán earthquake released proportionally more afterslip than did the 1995 earthquake even though the moment of the 1995 earthquake was five times larger than in 2003.

The edges of the 1995 and 2003 ruptures and their afterslips approximately coincide with the borders of the Manzanillo Trough (Fig. 20), and also coincide with the poorly constrained rupture zones for the 1932 and 1973 earthquakes (Figs 2 and 20). This suggests that structures within or near the Manzanillo Trough, including the Tecomán trough, Manzanillo horst and other nearby seismically imaged normal and strike-slip faults (Bandy *et al.* 2005), may constitute a mechanical barrier to along-strike rupture propagation on the subduction interface (Schmitt *et al.* 2007). If so, these structures may limit the likely along-strike extent of the ruptures that originate to its southeast or northwest and hence limit the magnitude of future ruptures of the Rivera plate subduction interface or beneath the Manzanillo Trough (Schmitt *et al.* 2007). Using Hutton *et al.* (2001)'s assumed maximum rupture area of 200 km along-strike by 80 km downdip for the subduction interface northwest of the Manzanillo Trough (16,000 km^2), a hypothetical 4 m uniform rupture of the entire area would have a moment magnitude of $M_{\mathrm{w}} = 8.2$ (for a shear modulus of 40 GPa). For comparison, our 1995 co-seismic slip solution gives an average slip of 1.8 m over an area of ∼13,200 km^2. Similarly, using Schmitt *et al.* (2007)'s assumed maximum rupture area of the seismogenic zone beneath the Manzanillo Trough (70 km along-strike and 70 km downdip), a 3 m uniform rupture of the entire area would have a moment magnitude of $M_{\mathrm{w}} = 7.8$. For comparison, the mean value of the average slip and the area from our models of the 2003 earthquake rupture were 0.8 m and ∼5,800 km^2, respectively.

From continuous measurements at ∼50 broadband seismometers in western Mexico, Brudzinski *et al.* (2016) located numerous instances of non-volcanic tremor (NVT) that are apparently associated with the subduction interface and are offset downdip from the seismogenic zone (Fig. 20). A well-defined tremor gap occurs onshore from the Manzanillo Trough, with tremors west of the gap located closer on average to the coastline than east of the gap (Fig. 20). Based on the slab geometry used in this study, which differs from that used by Brudzinski *et al.* (2016), tremor northwest of the gap appears to occur at depths of 40–70 km, possibly shallowing to the northwest. Tremor east of the gap is instead mostly at depths of 50–70 km (Fig. 20). In both areas, our afterslip solutions suggest 0.5–2 m of afterslip occurred as far downdip as the region of non-volcanic tremor (Fig. 20). Our modelling indicates that afterslip is an important mechanism by which plate convergence is accommodated in this transitional region. Further observations are needed

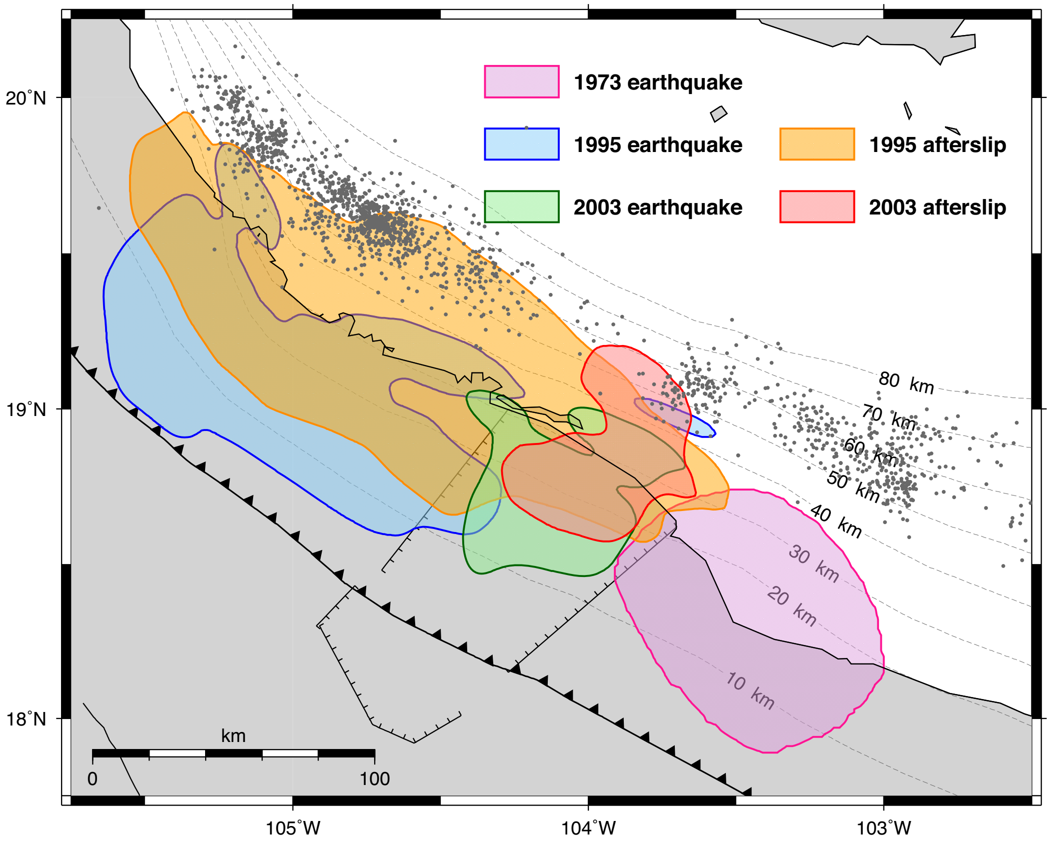

Figure 20. Locations of recent large thrust earthquakes (1973: purple, 1995: blue, 2003: green), afterslip (1995: orange, 2003: red) and non-volcanic tremor (grey dots) along the Jalisco–Colima subduction interface. The 1973 rupture is from Reyes *et al.* (1979). The 1995 and 2003 co-seismic ruptures and afterslip correspond to the 0.5 m contour of the co-seismic slip and afterslip solutions from our model with viscoelastic rebound corrections using $\tau_m = 15$ yr. Tremor locations are from Brudzinski *et al.* (2016). Dashed lines show the slab contours every 10 km.

to determine how much, if any of the plate convergence is accommodated by slow slip events (SSEs). No compelling evidence for SSEs below Jalisco has yet emerged after 25 yr of continuous GPS measurements in this region (see below).

Our results suggest the seismogenic zone extends between depths of 5 km to ∼40 km (Fig. 20). Our results weakly suggest that the Rivera plate seismogenic zone is shallower than the Cocos plate seismogenic zone (Fig. 20), in accord with the extended Slab 1.0 subduction depth contours for the northwest Mexico subduction zone (dotted lines in Fig. 20). The 1995 and 2003 earthquakes were followed by large afterslip that partially overlapped their rupture zones and extended downdip to depths of 60–65 km. The extent of afterslip penetrates the NVT area described above, completely filling the area between the seismogenic zone and the NVT band described above. Table 1 summarizes the depths of these different processes.

Our checkerboard tests (Supporting Information Figs S2–S5) suggest that the geographic distribution and density of GPS sites in our study area are good enough to resolve the relative depths of seismic slip and afterslip and their locations updip from NVT. Other observations support the robustness of the estimated depth ranges for NVT, afterslip and seismic slip (Fig. 20). Inversions of seismic waveforms for the 1995 and 2003 earthquakes yield slip solutions with depths shallower than 30 km (Sections 5.1 and 5.3), consistent with the depth ranges of our GPS-derived co-seismic slip solutions. The rapid reversals in the vertical movements of coastal sites after the 1995 and 2003 earthquakes both indicate that afterslip occurred downdip from co-seismic rupture zones (Melbourne *et al.* 1997; Hutton *et al.* 2001; Schmitt *et al.* 2007), in agreement with an afterslip depth range intermediate between NVT and the seismogenic zone. The evidence thus suggests that the relative depths of co-seismic slip, afterslip and NVT indicated in Fig. 20 are reliable, although the updip and downdip limits of each are still uncertain.

6.3 Comparative subduction along the Jalisco versus Guerrero/Oaxaca segments

Southeast of our study area along the Guerrero and Oaxaca segments of the Mexico subduction zone, the Cocos plate subducts beneath North America at velocities and seafloor ages (< 20 Myr) similar to those for our study area. The age of the subducting Cocos plate lithosphere diminishes gradually to the northwest along the trench from ∼15 Myr along the Guerrero and Oaxaca segments (Seton *et al.* 2020) to 11 Myr along the Rivera subduction zone (DeMets & Traylen 2000). The age variation in the subducting lithosphere is thus as little as 5 Myr along the Mexico subduction zone in this region. Although the subduction interface along the Guerrero and Oaxaca trench segments remains flat-to-nearly-flat more than 200 km beneath central Mexico (Pérez-Campos *et al.* 2008; Kim *et al.* 2010), thrust earthquakes for both segments are typically shallower than depths of ∼25 km (Suárez & Sánchez 1996; Pacheco & Singh 2010). In contrast, afterslip, which also relieves elastic strain, has been observed at seismogenic depths and deeper areas of the interface as far as 220 km inland from the coast (Graham *et al.*

Table 1. Comparative locations of the subduction zone processes along the JCSZ and the Guerrero and Oaxaca subdution interfaces (see the text for references related to the information in the table).

	JCSZ			
	Northwestern segment	Southeastern segment	Guerrero segment	Oaxaca segment
Max. depth of the seismogenic zone	∼25 km	∼40 km	∼25 km	∼25 km
Max. depth of afterslip	∼60 km	∼60 km	∼50 km	∼50 km
Max. depth of SSEs	—	—	∼40 km, with possible overlap with the seismogenic zone in Guerrero	
SSE magnitude	—	—	∼7.5	∼6.5–7.0
Depth of NVT	∼40–70 km	∼50–70 km	∼40 km	∼40–50 km
Offset of the seismogenic zone and NVT	∼5 km inland	∼40 km inland	∼80 km inland	∼50 km inland

2014b). GPS observations since the early 1990s have recorded numerous SSEs at depths of ∼20–40 km, with equivalent magnitudes that are larger than observed along any other subduction zone (e.g. Lowry *et al.* 2001; Kostoglodov *et al.* 2003, 2010; Brudzinski *et al.* 2007; Larson *et al.* 2007; Correa-Mora *et al.* 2008, 2009; Vergnolle *et al.* 2010; Radiguet *et al.* 2012; Cavalié *et al.* 2013; Graham *et al.* 2014a, 2016; Bekaert *et al.* 2015; Maubant *et al.* 2020). Seismic observations have detected widespread NVT on the subduction interface downdip from the source regions of SSEs and offset downdip from the megathrust earthquake rupture zones (Payero *et al.* 2008; Brudzinski *et al.* 2010; Kostoglodov *et al.* 2010).

Despite the geometric similarities of the Guerrero and Oaxaca subduction interfaces, SSEs beneath Guerrero have larger magnitudes ($M\sim7.5$) than those beneath Oaxaca ($M\sim6.5$–7), and the SSEs are shallower, possibly intruding the seismogenic zone and releasing a portion of the accumulated shallow elastic strain (Kostoglodov *et al.* 2003; Iglesias *et al.* 2004; Yoshioka *et al.* 2004; Larson *et al.* 2007; Radiguet *et al.* 2012; Cavalié *et al.* 2013; Graham *et al.* 2016). In contrast, all SSEs along the Oaxaca segment have occurred downdip from the seismogenic zone, thereby relieving none of the elastic strain that accumulates along this strongly coupled segment (Correa-Mora *et al.* 2008; Radiguet *et al.* 2012; Graham *et al.* 2016). The occurrence of larger SSEs coincides with larger spatial offsets between the area of occurrence of large thrust earthquakes and the location of tremor, which are, respectively, ∼80 km and ∼50 km from the trench in Guerrero and Oaxaca (Brudzinski *et al.* 2016).

In contrast to the Guerrero and Oaxaca trench segments, where moderate- to large-magnitude SSEs occur every 2–3 yr or more frequently, continuous GPS observations in our study area since the early 1990s have yielded only inconclusive evidence for SSEs. Brudzinski *et al.* (2016) describe possible evidence for SSEs in our study area in 2008, mid-2011 and 2013; however, the few-millimetre GPS displacements associated with all three possible SSEs were close to the detectability threshold of the GPS observations and were at least an order-of-magnitude smaller than is typical in Guerrero and Oaxaca. To date, the absence (or infrequency) of moderate or large-magnitude SSEs appears to be the primary difference between how subduction is accommodated along the JCSZ versus the Guerrero and Oaxaca trench segments.

Brudzinski *et al.* (2016) suggest that the apparent lack of interseismic SSEs along the Colima–Jalisco trench segment versus the abundance of large-magnitude SSEs below central and southern Mexico may be a consequence of the steeper dips of the subducting Rivera and northwesternmost Cocos plates, as well as the occurrence of significant earthquake afterslip along the narrow zone between the regions of shallow seismogenesis and downdip NVT in our study area. Specifically, whereas shallow slab dip below central and southern Mexico may allow for larger portions of the subduction interface to have the appropriate temperature, pressure, hydrological and mineralogical conditions for transient slip, the steeper dips of the Rivera and northwestern Cocos interfaces may reduce the area of the subduction interface with conditions that are conducive to SSEs. The offset between the area of NVT and deepest co-seismic slip in our study area ranges from only ∼5 to 40 km (Fig. 20), half or less the ∼80 km offset in Guerrero and ∼50 km offset in Oaxaca (Brudzinski *et al.* 2016).

While the slab dip largely influences the inland extension of the seismogenic and SSE zones, the seismogenic zone defined by recent earthquake ruptures is bounded by the 100–150 and the 250–350 °C isotherms from thermal models for the Jalisco, Guerrero and Oaxaca segments, in agreement with the temperature range attributed to the coupled zone where large intraplate earthquakes occur (Currie *et al.* 2002; Manea *et al.* 2004; Manea & Manea 2011). Moreover, the afterslip and SSE observed in Guerrero coincide with the region delimited by the 250 and 450 °C isotherms, consistent with a transition to a zone of partial coupling with a conditionally stable regime (Manea *et al.* 2004). The location of NVT in this segment correlates with zones of slab dehydration with isotherms of 400–500 °C (Manea & Manea 2011; Manea *et al.* 2013). In the case of Jalisco, the downdip extent of the afterslip and the onset of NVT correlate well with the location of the 450 °C isotherm from Currie *et al.* (2002).

Our modelling suggests that afterslip in 1995 and 2003 extended all the way downdip to the region of NVT on the Rivera/Cocos subduction interfaces (Fig. 20). If the frictional properties of subduction interfaces differ significantly in areas where post-seismic afterslip and interseismic SSEs occur, as suggested by Malservisi *et al.* (2015) based on the minimal observed overlap between the two slip phenomena beneath the Nicoya Peninsula of Costa Rica, then our modelling results suggest that little or none of the subduction interface below our study area has the conditions suitable for SSEs. Alternatively, if frictional conditions do permit SSEs and post-seismic afterslip to occur along the same parts of a subduction interface, as appears to be true along the Oaxaca segment (Graham *et al.* 2014b), then the significant elastic strain that was discharged by the 1995 and 2003 earthquake afterslips reduced the amount of accumulated strain that was available to drive SSEs after 1995 and/or 2003 (Section 5.5, Tables S5 and S7). This hypothesis is further supported by numerical models of the earthquake cycle of megathrust earthquakes, in which the occurrence of large earthquakes followed by afterslip that propagates downdip into the slow-slip region weakens the fault segment and releases strain energy, thus suppressing SSEs for up to a few decades (Shi *et al.* 2020). Overlap of post-seismic afterslip regions and SSE and tremor zones has been observed in other subduction zones such as Cook Inlet, Alaska (Huang *et al.* 2020) and Nankai, Japan (Sherrill & Johnson 2021). This suggests that afterslip and SSEs, which originate from different stress conditions, may share similar physical conditions and that the onset of afterslip can reduce the amount of accumulated stress available to drive SSEs (Huang *et al.* 2020).

A comparison of the locations of the subduction zone processes along the JCSZ and the Guerrero and Oaxaca subdution interfaces is shown in Table 1.

6.4 Challenges and pitfalls of our modelling: model fits and residuals

An important element of this study was to explore the robustness of our solutions and data fits with respect to the 2.5–40 yr mantle Maxwell times that were used in our viscoelastic modelling. The TDEFNODE misfits F (eq. 3) varied by only ∼10 per cent for the wide range of mantle Maxwell times we tested (Supporting Information Table S12), including an inversion of the GPS position time-series without any viscoelastic corrections (Supporting Information Section S1, Tables S3, S5, S7, S9 and S11, and Figs S19 and S20). The mantle rheology is thus not strongly constrained by our observations, as expected given the many fitting trade-offs that exist between the model parameters. The observations that provide the most information on the mantle rheology are the mostly campaign measurements during 1995–1999, the period of rapid transient deformation due to the 1995 Colima–Jalisco earthquake. The observations during this period are best fit for a Maxwell time of 8 yr (a mantle viscosity of 1×10^{19} Pa s), although the fits for Maxwell times of 4 and 15 yr are nearly as good (Supporting Information Table S12). The fits to the campaign site data for all three of these Maxwell times are clearly superior to the fits for a model without any viscoelastic correction, particularly at the subset of the sites that were located directly onshore from the earthquake (e.g. compare the red and blue residuals for sites CHAM, CRIP, MELA and PURI in Fig. 21 for $\tau_m = 8$ yr).

The 0.5–1.9 $\times 10^{19}$ Pa s mantle viscosities associated with the 4–15 yr Maxwell times are consistent with viscosities estimated in similar previous studies, including 3.2×10^{19} Pa s for the 1964 Alaska earthquake (Suito & Freymueller 2009); $\sim 10^{19}$ Pa s for the 1960 Chile, 2006 Sumatra and ∼1700 Cascadia megathrust earthquakes (Wang *et al.* 2012); 5×10^{18} Pa s and 3×10^{19} Pa s respectively for a low-viscosity wedge and the long term mantle viscosity (Trubienko *et al.* 2013); and 0.8–1.5 $\times 10^{19}$ Pa s from modelling of long-term post-seismic deformation in Nankai (Johnson & Tebo 2018). Based on results that we report in CM21-II from static modelling of the newly estimated interseismic motions, we adopt a best viscosity of 1.9×10^{19} Pa s ($\tau_m = 15$ yr).

None of our solutions satisfactorily fits all the GPS data. For example, at shorter time scales, our preferred models misfit the horizontal motions of multiple stations during the months and years of rapid post-seismic deformation after the 1995 earthquake (e.g. Fig. 21 and Supporting Information Fig. S21, $\tau_m = 8$ yr). At intermediate time scales, the preferred model fails to predict ∼6 months of observed post-seismic subsidence at site COLI immediately after the 2003 earthquake (Fig. 17). Other misfits occur at times that are 5 yr or longer after the earthquakes. Most notably, the continuous sites COLI and COOB clearly experienced a gradual transition from slow post-seismic uplift in the years after the 2003 Tecomán earthquake to slow subsidence after ∼2015 (Figs 3, 7a, 13, 17 and 21), which our models fail to capture.

Although practical considerations precluded any further effort to improve the fits, some candidates to explore for improving the fits include the following: (1) different subduction interface geometries (Pardo & Suárez 1995; Andrews *et al.* 2011; Abbott & Brudzinski 2015; Hayes *et al.* 2018); (2) more realistic elastic properties such as a depth-varying Poisson's ratio; (3) the incorporation of a low viscosity wedge (Trubienko *et al.* 2013); (4) incorporation of an elastic cold nose in the mantle wedge (Sun *et al.* 2014; Freed *et al.* 2017; Johnson & Tebo 2018); (5) the use of power law or Burgers mantle rheologies to estimate the viscoelastic corrections (Freed & Bürgmann 2004; Freed *et al.* 2006; Hu & Wang 2012; Wang *et al.* 2012; Trubienko *et al.* 2013; Sun *et al.* 2014, 2018; Peña *et al.* 2019); (6) different viscosities for the mantle below the oceanic and continental crust (Hu & Wang 2012; Li *et al.* 2015; Wiseman *et al.* 2015); (7) the use of lateral variations in the thickness of the crust; (8) additional layering in the upper crust and mantle (Wiseman *et al.* 2015; Freed *et al.* 2017); and (9) viscoelastic layer thicknesses and depths different than those assumed for our analysis (i.e. Fig. 8). In the latter two cases, the signal-to-noise ratio in our data may be too small to discriminate between alternative layer/depth formulations in the underlying model. Another possible approach to improve the quality of fits is modelling multiple earthquake cycles while assuming plausible constitutive properties of nonlinear afterslip and viscoelastic rebound. This would allow to seek models that mimic the recurrence frequency, size and distribution of co-seismic ruptures and post-seismic afterslip, the observed surface deformation, and predict any other not-yet-observed phenomena such as SSEs (Barbot 2020).

7 CONCLUSIONS

The $M_w = 8.0$ 1995 Colima–Jalisco and $M_w = 7.5$ 2003 Tecomán earthquakes on the JCSZ triggered unusually large post-seismic afterslip and significant viscoelastic responses. Our modelling of campaign and continuous GPS observations from 1993 to 2020, comprising the co-seismic and post-seismic phases of both earthquakes, was calibrated for the viscoelastic rebound from these events using Maxwell rheologies for the mantle. Our results, optimized to fit the post-seismic phase of the 1995 earthquake, which had the largest viscoelastic response, are consistent with mantle viscosities of 0.5–1.9 $\times 10^{19}$ Pa s (Maxwell times of 4–15 yr), in agreement with similar studies in other subduction zones. Based on results from static modelling of the newly estimated interseismic motions (CM21-II), we adopt a best viscosity of 1.9×10^{19} Pa s ($\tau_m = 15$ yr).

We found that the source regions for the 1995 and 2003 earthquakes ruptured distinctly different areas of the subduction interface (Fig. 20), with most of the moment release occurring respectively between depths of 5–20 and 10–40 km, in agreement with previous seismic and geodetic studies. The results suggest the seismogenic zone extends between depths of ∼5 and ∼40 km, and may become shallower to the northwest along the interface (Fig. 20).

The large afterslip following the 1995 and 2003 earthquakes partially overlapped their rupture zones and extended downdip to depths of 60–65 km. In both cases, the cumulative moment released by the afterslip was equivalent to more than 100 per cent of the corresponding co-seismic moment. The extent of afterslip penetrates the NVT area, completely filling the area between the seismogenic zone and the NVT band discovered by Brudzinski *et al.* (2016; Fig. 20). The size and extent of the afterslip, as well as the narrower gap between the seismogenic zone and the NVT could explain the lack of observed SSE in the area which, along with

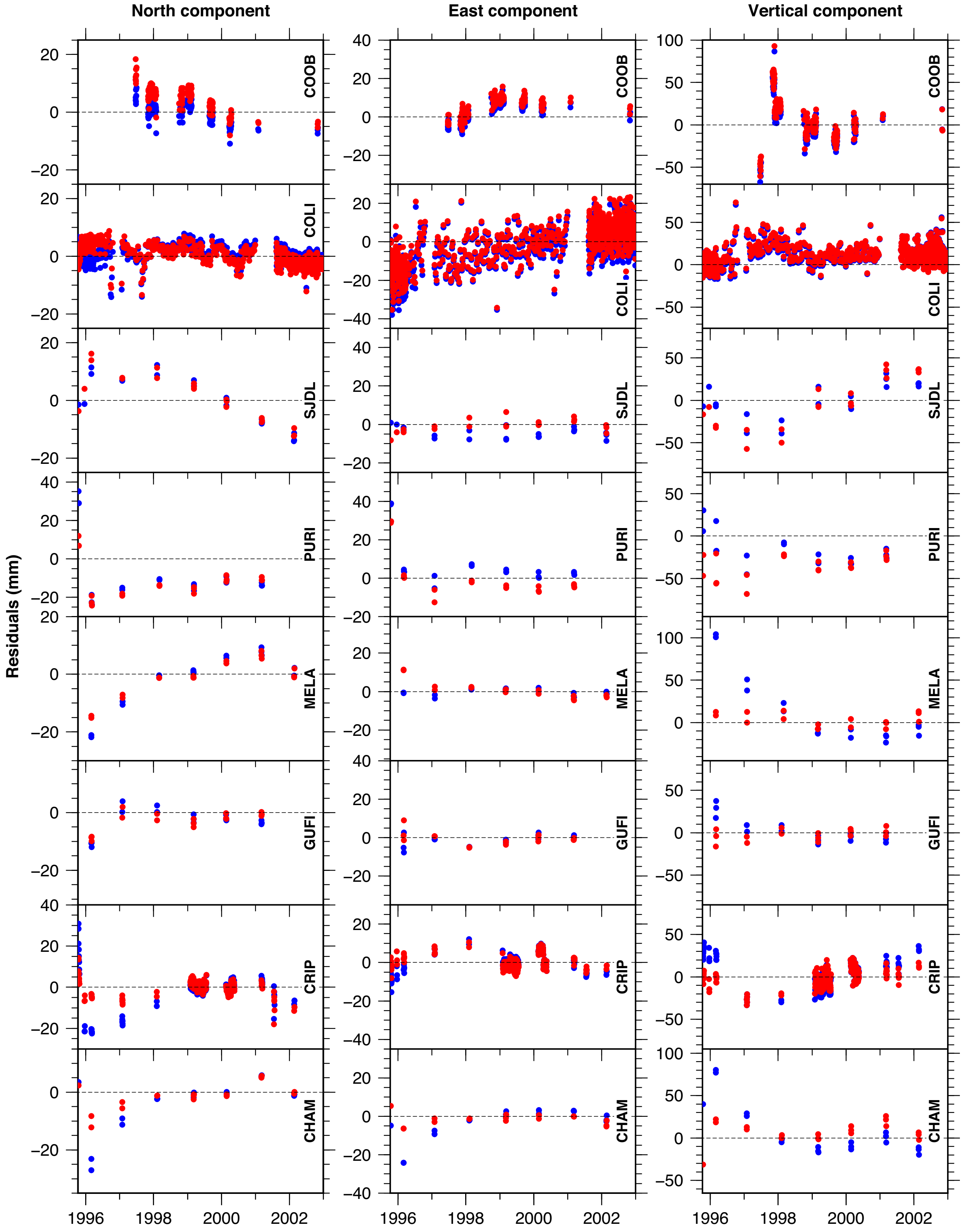

Figure 21. Residuals at selected sites from our model with viscoelastic response corrections using $\tau_{\mathrm{m}} = 8$ yr for the mantle (red) and with no corrections for viscoelastic effects (blue), for the time interval between the 1995 and 2003 earthquakes.

the steeper slab, differentiates the JCSZ from its neighbours to the southwest, the Guerrero and Oaxaca segments.

ACKNOWLEDGEMENTS

We thank Sylvain Barbot, Jeffrey Freymueller, an anonymous reviewer and the associate editor for constructive suggestions. Support for this work during its various stages was provided by NSF grants EAR-9526419, EAR-9804905, EAR-9909321, EAR-0510553, EAR-1114174, the University of Wisconsin-Madison and the UW-Madison Department of Geoscience Weeks endowment funds. This material is based on GPS data and services provided by the GAGE Facility, operated by UNAVCO, Inc. and by the TLALOCNet GPS network operated by Servicio de Geodesia Satelital (SGS; Cabral-Cano *et al.* 2018) at the Instituto de Geofísica-Universidad Nacional Autónoma de México (UNAM). UNAVCO's initial support for TLALOCNet (now part of NOTA) was performed under EAR-1338091 and is currently supported by the National Science Foundation and the National Aeronautics and Space Administration under NSF Cooperative Agreement EAR-1724794. TLALOCNet and other GPS related operations from SGS have also been supported by the Consejo Nacional de Ciencia y Tecnología (CONACyT) projects 253760, 256012 and 2017-01-5955, UNAM-Programa de Apoyo a Proyectos de Investigación e Innovación Tecnológica (PAPIIT) projects IN104213, IN111509, IN109315-3, IN104818-3, IN107321 and supplemental support from UNAM-Instituto de Geofísica. We are deeply grateful to all personnel from UNAVCO and SGS for station maintenance, data acquisition, IT support and data curation and distribution for these networks and in particular to the following individuals and institutions, whose hard work and resourcefulness were central to the success of this project: Bill Douglass, Neal Lord and Bill Unger at UW-Madison, Oscar Díaz-Molina and Luis Salazar-Tlaczani at SGS, John Galetzka, Adam Wallace, Shawn Lawrence, Sean Malloy and Chris Walls at UNAVCO, Jesus Pacheco-Martínez at Universidad Autónoma de Aguascalientes, personnel at the Universidad de Guadalajara at campus Guadalajara, Mascota and Ameca, Protección Civil de Jalisco, Universidad de Colima at campus Colima and campus El Naranjo and Instituto de Biología-UNAM Estación Chamela. Most figures were produced using Generic Mapping Tools software (Wessel & Smith 1991).

DATA AVAILABILITY

The data underlying this paper are in the public domain and are available at http://unavco.org, with the exception of GPS sites COLI and INEG. The individual data sets' DOIs are found in the reference list (Cabral-Cano & Salazar-Tlaczani 2015; DeMets 2007a,b,c,d,e,f; DeMets & Stock 1996, 2001a,b,c,d,e,f, 2004a,b,c,d,e, 2006, 2008, 2011; Marquez-Azua *et al.* 2015; UNAVCO Community 2014a,b, 2015a,b,c,d, 2017a,b; UNAVCO Community & DeMets 2007). Data from the GPS sites COLI and INEG for the period 1993–2001 were provided courtesy of Professor Bertha Márquez-Azúa of the University of Guadalajara (bmarquez@cencar.udg.mx). COLI and INEG data from 2001 to 2020 were procured from ftp://geodesia.inegi.org.mx.

REFERENCES

Abbott, E.R. & Brudzinski, M.R., 2015. Shallow seismicity patterns in the northwestern section of the Mexico Subduction Zone, *J. South Am. Earth Sci.,* **63,** 279–292.

Altamimi, Z., Rebischung, P., Métivier, L. & Collilieux, X., 2016. ITRF2014: a new release of the international terrestrial reference frame modeling nonlinear station motions, *J. geophys. Res.,* **121,** 6109–6131.

Andrews, V., Stock, J., Ramírez Vázquez, C.A. & Reyes-Dávila, G., 2011. Double-difference relocation of the aftershocks of the Tecomán, Colima, Mexico earthquake of 22 January 2003, *Pure appl. Geophys.,* **168,** 1331–1338.

Bandy, W.L. *et al.*, 2005. Subsidence and strike-slip tectonism or the upper continental slope off Manzanillo, Mexico, *Tectonophysics,* **398,** 115–140.

Barbot, S., 2014. RELAX v1.0.7 [software], computational infrastructure for geodynamics, url:https://geodynamics.org/cig/software/relax/.

Barbot, S., 2018. Asthenosphere flow modulated by megathrust earthquake cycles, *Geophys. Res. Lett.,* **45**(12), 6018–6031.

Barbot, S., 2020. Frictional and structural controls of seismic super-cycles at the Japan trench, *Earth Planets Space,* **72**(63), 1–25.

Barbot, S. & Fialko, Y., 2010a. A unified continuum representation of post-seismic relaxation mechanisms: semi-analytic models of afterslip, poroelastic rebound and viscoelastic flow: Semi-analytic models of postseismic transient, *Geophys. J. Int.,* **182**(3), 1124–1140.

Barbot, S. & Fialko, Y., 2010b. Fourier-domain Green's function for an elastic semi-infinite solid under gravity, with applications to earthquake and volcano deformation: Fourier-domain elastic solutions, *Geophys. J. Int.,* **182**(2), 568–582.

Bedford, J., Moreno, M., Li, S., Oncken, O., Baez, J.C., Bevis, M., Heidbach, O. & Lange, D., 2016. Separating rapid relocking, afterslip, and viscoelastic relaxation: an application of the postseismic straightening method to the Maule 2010 cGPS, *J. geophys. Res.,* **121,** 7618–7638.

Bekaert, D.P.S., Hooper, A. & Wright, T.J., 2015. Reassessing the 2006 Guerrero slow-slip event, Mexico, *J. geophys. Res.,* **120,** 1357–1375.

Ben-Menahmen, A. & Singh, S.K., 1981. *Seismic Waves and Sources,* Springer-Verlag.

Bertiger, W., Desai, S.D., Haines, B., Harvey, N., Moore, A.W., Owen, S. & Weiss, J.P., 2010. Single receiver phase ambiguity resolution with GPS data, *J. Geod.,* **94,** 327–337.

Brudzinski, M., Cabral-Cano, E., Correa-Mora, F., DeMets, C. & Marquez-Azua, B., 2007. Slow slip transients along the Oaxaca subduction segment from 1993 to 2007, *Geophys. J. Int.,* **171,** 523–538.

Brudzinski, M.R., Hinojosa-Prieto, H.R., Schlanser, K.M., Cabral-Cano, E., Arciniega-Ceballos, A., Díaz-Molina, O. & DeMets, C., 2010. Nonvolcanic tremor along the Oaxaca segment of the Middle America subduction zone, *J. geophys. Res.,* **115,** B00A23, doi:10.1029/2008JB006061.

Brudzinski, M., Schlanser, K.M., Kelly, N.J., DeMets, C., Grand, S.P., Márquez-Az a, B. & Cabral-Cano, E., 2016. Tectonic tremor and slow slip along the northwestern section of the Mexico subduction zone, *Earth planet. Sci. Lett.,* **454,** 259–271.

[dataset]Cabral-Cano, E. & Salazar-Tlaczani, L., 2015. *TLALOCNet - UAGU-uagu_tnet_mx2008 P.S., UNAVCO, GPS/GNSS Observations Dataset,* doi:10.7283/T5513WK7.

Cabral-Cano, E. *et al.*, 2018. TLALOCNet: a continuous GPS-Met backbone in Mexico for seismotectonic and atmospheric research, *Seismol. Res. Lett.,* **89**(2A), 373–381.

Cavalié, O., Pathier, E., Radiguet, M., Vergnolle, M., Cotte, N., Walpersdorf, A., Kostoglodov, V. & Cotton, F., 2013. Slow slip event in the Mexican subduction zone: evidence of shallower slip in the Guerrero seismic gap for the 2006 event revealed by the joint inversion of InSAR and GPS data, *Earth planet. Sci. Lett.,* **367,** 52–60.

Corbo-Camargo, F., Arzate-Flores, J.A., Álvarez-Béjar, R., Aranda-Gómez, J.J. & Yutsis, V., 2013. Subduction of the Rivera plate beneath the Jalisco block as imaged by magnetotelluric data, *Rev. Mex. Cienc. Geol.,* **30**(2), 268–281.

Correa-Mora, F., DeMets, C., Cabral-Cano, E., Marquez-Azua, B. & Díaz-Molina, O., 2008. Interplate coupling and transient slip along the subduction interface beneath Oaxaca, Mexico, *Geophys. J. Int.,* **175,** 269–290.

Correa-Mora, F., DeMets, C., Cabral-Cano, E., Díaz-Molina, O. & Marquez-Azua, B., 2009. Transient deformation in southern Mexico in 2006 and 2007: evidence for distinct deep-slip patches beneath Guerrero and Oaxaca, *Geochem. Geophys Geosyst.,* **10,** Q02S12, doi:10.1029/2008GC002211.

Cosenza-Muralles, B., DeMets, C., Márquez-Azúa, B., Sánchez, O., Stock, J., Cabral-Cano, E. & McCaffrey, R., 2021. GPS-derived interseismic fault locking along the Jalisco–Colima segment of the Mexico subduction zone, *Geophys. J. Int.*. Available at: https://doi.org/10.1093/gji/ggab436.

Courboulex, F., Singh, S.K. & Pacheco, J.F., 1997. The 1995 Colima-Jalixco, Mexico, earthquake (Mw 8): a study of the rupture process, *Geophys. Res. Lett.,* **24**(9), 1019–1022.

Currie, C.A., Hyndman, R.D., Wang, K. & Kostoglodov, V., 2002. Thermal models of the Mexico subduction zone: implications for the megathrust seismogenic zone, *J. geophys. Res.,* **107**(B12), 2370.

DeMets, C., 2007a. *Jalisco GPS Network - FARO-El Faro lighthouse P.S., UNAVCO, GPS/GNSS Observations Dataset,* doi:10.7283/T5NG4NQB.

DeMets, C., 2007b. *Jalisco GPS Network - PENA-US Gypsum Mine at Pena Colorada P.S., UNAVCO, GPS/GNSS Observations Dataset,* doi:10.7283/T51R6NMX.

DeMets, C., 2007c. *Jalisco GPS Network - PURI-Purificacion P.S., UNAVCO, GPS/GNSS Observations Dataset,* doi:10.7283/T5X0655S.

DeMets, C., 2007d. *Jalisco GPS Network - PZUL-Telmex tower near Cruz de Loreto P.S., UNAVCO, GPS/GNSS Observations Dataset,* doi:10.7283/T5DZ06D2.

DeMets, C., 2007e. *Jalisco GPS Network - TECO-APASCO Cement Factory and quarry P.S., UNAVCO, GPS/GNSS Observations Dataset,* doi:10.7283/T5S75DF2.

DeMets, C., 2007f. *Jalisco GPS Network - UCOM-Univ. Colima at Manzanillo P.S., UNAVCO, GPS/GNSS Observations Dataset,* doi:10.7283/T5959FNN.

DeMets, C. & Stock, J., 1996. *Jalisco 1996, UNAVCO, GPS/GNSS Observations Dataset,* doi:10.7283/T5XD0ZS7.

DeMets, C. & Stock, J., 2001a. *Jalisco 1995 03 (March), UNAVCO, GPS/GNSS Observations Dataset,* doi:10.7283/T5K35RSF.

DeMets, C. & Stock, J., 2001b. *Jalisco 1995 10 (October), UNAVCO, GPS/GNSS Observations Dataset,* doi:10.7283/T55T3HKM.

DeMets, C. & Stock, J., 2001c. *Jalisco 1997, UNAVCO, GPS/GNSS Observations Dataset,* doi:10.7283/T5222RWN.

DeMets, C. & Stock, J., 2001d. *Jalisco 1998, UNAVCO, GPS/GNSS Observations Dataset,* doi:10.7283/T5SN073R.

DeMets, C. & Stock, J., 2001e. *Jalisco 1999, UNAVCO, GPS/GNSS Observations Dataset,* doi:10.7283/T59K48BS.

DeMets, C. & Stock, J., 2001f. *Jalisco GPS Network - CRIP-Cent. Reg. Inv. Pesqueras P.S., UNAVCO, GPS/GNSS Observations Dataset,* doi:10.7283/T5RN360T.

DeMets, C. & Stock, J., 2004a. *Jalisco 2000, UNAVCO, GPS/GNSS Observations Dataset,* doi:10.7283/T5FB512H.

DeMets, C. & Stock, J., 2004b. *Jalisco 2001, UNAVCO, GPS/GNSS Observations Dataset,* doi:10.7283/T5NV9GCG.

DeMets, C. & Stock, J., 2004c. *Jalisco 2002, UNAVCO, GPS/GNSS Observations Dataset,* doi:10.7283/T5J38QN2.

DeMets, C. & Stock, J., 2004d. *Jalisco 2003, UNAVCO, GPS/GNSS Observations Dataset,* doi:10.7283/T5DB7ZXB.

DeMets, C. & Stock, J., 2004e. *Jalisco 2004, UNAVCO, GPS/GNSS Observations Dataset,* doi:10.7283/T58K775Z.

DeMets, C. & Stock, J., 2006. *Jalisco 2005, UNAVCO, GPS/GNSS Observations Dataset,* doi:10.7283/T54T6GGP.

DeMets, C. & Stock, J., 2008. *Jalisco 2007, UNAVCO, GPS/GNSS Observations Dataset,* doi:10.7283/T5154F50.

DeMets, C. & Stock, J., 2011. *Jalisco 2009, UNAVCO, GPS/GNSS Observations Dataset,* doi:10.7283/T5WD3XQR.

DeMets, C. & Traylen, S., 2000. Motion of the Rivera plate since 10 Ma relative to the Pacific and North American plates and the mantle, *Tectonophysics,* **318,** 119–159.

DeMets, C. & Wilson, D.S., 1997. Relative motions of the Pacific, Rivera, North American, and Cocos plates since 0.78 Ma, *J. geophys. Res.,* **102,** 2789–2806.

DeMets, C., Carmichael, I., Melbourne, T., Sánchez, O., Stock, J., Suárez, G. & Hudnut, K., 1995. Anticipating the successor to Mexico's largest historical earthquake, *EOS, Trans. Am. geophys. Un.,* **76**(42), 417–424.

DeMets, C., Gordon, R.G. & Argus, D.F., 2010. Geologically current plate motions, *Geophys. J. Int.,* **181,** 1–80.

Dziewonski, A.M., Ekström, G. & Salganik, M.P., 1997. Centroid- moment tensor solutions for October–December 1995, *Phys. Earth planet. Inter.,* **101,** 1–12.

Ekström, G., Dziewonski, A.M., Maternovskaya, N.N. & Nettles, M., 2004. Global seismicity of 2003: centroid-moment-tensor solutions for 1087 earthquakes, *Phys. Earth planet. Inter.,* **148,** 327–351.

Escobedo, D., Pacheco, J.F. & Suárez, G., 1998. Teleseismic body-wave analysis of the 9 October, 1995 ($M_w = 8.0$), Colima–Jalisco earthquake, and its largest foreshock and aftershock, *Geophys. Res. Lett.,* **25**(4), 547–550.

Freed, A.M. & Bürgmann, R., 2004. Evidence of power-law flow in the Mojave desert mantle, *Nature,* **430,** 548–551.

Freed, A.M., Bürgmann, R., Calais, E. & Freymueller, J., 2006. Stress-dependent power-law flow in the upper mantle following the 2002 Denali, Alaska, earthquake, *Earth planet. Sci. Lett.,* **252,** 481–489.

Freed, A.M., Hashima, A., Becker, T.W., Okaya, D.A., Sato, H. & Hatanaka, Y., 2017. Resolving depth-dependent subduction zone viscosity and afterslip from postseismic displacements following the 2011 Tohoku-oki, Japan earthquake, *Earth planet. Sci. Lett.,* **459,** 279–290.

Graham, S. *et al.*, 2014a. GPS constraints on the 2011/12 Oaxaca slow slip event that preceded the 20 March 2012 Ometepec earthquake, southern Mexico, *Geophys. J. Int.,* **197**(3), 1593–1607.

Graham, S. *et al.*, 2014b. GPS constraints on the $M_w = 7.5$ Ometepec earthquake sequence, southern Mexico: coseismic and post-seismic deformation, *Geophys. J. Int.,* **199,** 200–218.

Graham, S. *et al.*, 2016. Slow slip history for the MEXICO subduction zone: 2005 through 2011, *Pure appl. Geophys.,* **173,** 3445–3465.

Hayes, G.P., Moore, G.L., Portner, D.E., Hearne, M., Flamme, H. & Furtney, M., 2018. Slab2, a comprehensive subduction zone geometry model, *Science,* **362**(6410), 58–61.

Hayes, G.P., Wald, D.J. & Johnson, R.L., 2012. Slab1.0: a three-dimensional model of global subduction zone geometries, *J. geophys. Res.,* **117,** B01302, doi:10.1029/2011JB008524.

Hu, Y. & Wang, K., 2012. Spherical-Earth finite element model of short-term postseismic deformation following the 2004 Sumatra earthquake, *J. geophys. Res.,* **117,** B05404, doi:10.1029/2012JB009153.

Hu, Y., Wang, K., He, J., Klotz, J. & Khazaradze, G., 2004. Three- dimensional viscoelastic finite element model for post-seismic deformation of the great 1960 Chile earthquake, *J. geophys. Res.,* **109,** B12403, doi:10.1029/2004JB003163.

Huang, K., Hu, Y. & Freymueller, J.T., 2020. Decadal viscoelastic postseismic deformation of the 1964 M_w9.2 Alaska earthquake, *J. geophys. Res.,* **125,** e2020JB019649, doi:10.1029/2020JB019649.

Hutton, W., DeMets, C., Sánchez, O., Suárez, G. & Stock, J., 2001. Slip kinematics and dynamics during and after the 1995 October 9 M_w=8.0 Colima–Jalisco earthquake, Mexico, from GPS geodetic constraints, *Geophys. J. Int.,* **146,** 637–658.

Iglesias, A., Singh, S., Lowry, A., Santoyo, M., Kostoglodov, V., Larson, K. & Franco-Sánchez, S., 2004. The silent earthquake of 2002 in the Guerrero seismic gap, Mexico ($M_w = 7.6$): inversion of slip on the plate interface and some implications, *Geofis. Int.,* **43,** 309–317.

Johnson, K.M. & Tebo, D., 2018. Capturing 50 years of postseismic mantle flow at Nankai subduction zone, *J. geophys. Res.,* **123,** 10091–10106.

Kim, Y., Clayton, R.W. & Jackson, J.M., 2010. Geometry and seismic properties of the subducting Cocos plate in central Mexico, *J. geophys. Res.,* **115,** B06310, doi:10.1029/2010JB006942.

Kogan, M.G., Vasilenko, N.F., Frolov, D.I., Freymueller, J.T., Steblov, G.M., Prytkov, A.S. & Ekström, G., 2013. Rapid postseismic relaxation after the great 2006–2007 Kuril earthquakes from GPS observations in 2007–2011, *J. geophys. Res.,* **118,** 3691–3706.

Kostoglodov, V., Singh, S.K., Santiago, J.A., Franco, S.I., Larson, K.M., Lowry, A.R. & Bilham, R., 2003. A large silent earthquake in the Guerrero seismic gap, Mexico, *Geophys. Res. Lett.,* **30,** 1807.

Kostoglodov, V., Husker, A., Shapiro, N.M., Payero, J.S., Campillo, M., Cotte, N. & Clayton, R., 2010. The 2006 slow slip event and nonvolcanic tremor in the Mexican subduction zone, *Geophys. Res. Lett.,* **37,** L24301, doi:10.1029/2010GL045424.

Larson, K.M., Kostoglodov, V., Miyazaki, S.I. & Santiago, J.A.S., 2007. The 2006 aseismic slow slip event in Guerrero, Mexico: new results from GPS, *Geophys. Res. Lett.,* **34,** L13309, doi:10.1029/2007GL029912.

Li, S., Moreno, M., Bedford, J., Rosenau, M. & Oncken, O., 2015. Revisiting viscoelastic effects on interseismic deformation and locking degree: a case study of the Peru-North Chile subduction zone, *J. geophys. Res.,* **120,** 4522–4538.

Lin, Y.-N.N. *et al.*, 2013. Coseismic and postseismic slip associated with the 2010 Maule Earthquake, Chile: characterizing the Arauco Peninsula barrier effect, *J. geophys. Res.,* **118,** 3142–3159.

Lowry, A., Larson, K., Kostoglodov, V. & Bilham, R., 2001. Transient fault slip in Guerrero, southern Mexico, *Geophys. Res. Lett.,* **28,** 3753–3756.

Malservisi, R. *et al.*, 2015. Multiscale post- seismic behavior on a megathrust: the 2012 Nicoya earthquake, Costa Rica, *Geochem. Geophys. Geosyst.,* **16,** doi:10.1002/2015GC005794.

Manea, V.C. & Manea, M., 2011. Flat-slab thermal structure and evolution beneath central Mexico, *Pure appl. Geophys.,* **168,** 1475–1487.

Manea, V.C., Manea, M. & Ferrari, L., 2013. A geodynamical perspective on the subduction of Cocos and Rivera plates beneath Mexico and central America, *Tectonophysics,* **609,** 56–81.

Manea, V.C., Manea, M., Kostoglodov, V., Currie, C.A. & Sewell, G., 2004. Thermal structure, coupling and metamorphism in the Mexican subduction zone beneath Guerrero, *Geophys. J. Int.,* **158,** 775–784.

Marquez-Azua, B. & DeMets, C., 2003. Crustal velocity field of Mexico from continuous GPS measurements, 1993 to June, 2001: Implications for the neotectonics of Mexico, *J. geophys. Res.,* **108**(B9), 2450.

Marquez-Azua, B., DeMets, C. & Masterlark, T., 2002. Strong interseismic coupling, fault afterslip, and viscoelastic flow before and after the Oct. 9, 1995 Colima–Jalisco earthquake: Continuous GPS measurements from Colima, Mexico, *Geophys. Res. Lett.,* **29,** doi:10.1029/2002GL014702.

Marquez-Azua, B., DeMets, C., Cabral-Cano, E. & Salazar-Tlaczani, L., 2015. *TLALOCNet - UGEO-ugeo_tnet_mx1998 P.S., UNAVCO, GPS/GNSS Observations Dataset,* doi:10.7283/T58S4N9N.

Masterlark, T., DeMets, C., Wang, H.F., Sánchez, O. & Stock, J., 2001. Homogeneous vs heterogeneous subduction zone models: Coseismic and postseismic deformation, *Geophys. Res. Lett.,* **28**(21), 4047–4050.

Maubant, L. *et al.*, 2020. Independent component analysis and parametric approach for source separation in InSAR time series at regional scale: application to the 2017–2018 slow slip event in Guerrero (Mexico), *J. geophys. Res.,* **25,** e2019JB018187, doi:10.1029/2019JB018187.

McCaffrey, R., 2005. Block kinematics of the Pacific-North America plate boundary in the southwestern United States from inversion of GPS, seismological, and geologic data, *J. geophys. Res.,* **110,** B07401, doi:10.1029/2004JB003307.

McCaffrey, R., 2009. Time-dependent inversion of three-component continuous GPS for steady and transient sources in northern Cascadia, *Geophys. Res. Lett.,* **36,** L07304, doi:10.1029/2008GL036784.

Melbourne, T., Carmichael, I., DeMets, C., Hudnut, K., Sánchez, O., Stock, J., Suárez, G. & Webb, F., 1997. The geodetic signature of the M=8.0 October 9, 1995, Jalisco subduction earthquake, *Geophys. Res. Lett.,* **24,** 715–718.

Melbourne, T.I., Webb, F.H., Stock, J.M. & Reigber, C., 2002. Rapid postseismic transients in subduction zones from continuous GPS, *J. geophys. Res.,* **107**(B10), 2241.

Mendoza, C. & Hartzell, S., 1999. Fault-slip distribution of the 1995 Colima–Jalisco, Mexico, earthquake, *Bull. seism. Soc. Am.,* **89**(5), 1338–1344.

Okada, Y., 1985. Surface deformation to shear and tensile faults in a half-space, *Bull. seism. Soc. Am.,* **75,** 1135–1154.

Okada, Y., 1992. Internal deformation due to shear and tensile faults in a half-space, *Bull. seism. Soc. Am.,* **82,** 1018–1040.

Ortiz, M., Singh, S.K., Pacheco, J. & Kostoglodov, V., 1998. Rupture length of the October 9, 1995 Colima–Jalisco earthquake (Mw 8) estimated from tsunami data, *Geophys. Res. Lett.,* **25**(15), 2857–2860.

Pacheco, J.F. & Singh, S.K., 2010. Seismicity and state of stress in Guerrero segment of the Mexican subduction zone, *J. geophys. Res.,* **115,** B01303, doi:10.1029/2009JB006453.

Pacheco, J. *et al.*, 1997. The October 9, 1995 Colima–Jalisco, Mexico earthquake (Mw 8): An aftershock study and a comparison of the earthquake with those of 1932, *Geophys. Res. Lett.,* **24**(17), 2223–2226.

Pardo, M. & Suárez, G., 1995. Shape of the subducted Rivera and Cocos plates in southern Mexico: Seismic and tectonic implications, *J. geophys. Res.,* **100**(B7), 12357–12373.

Payero, J.S., Kostoglodov, V., Shapiro, N., Mikumo, T., Iglesias, A., Pérez-Campos, X. & Clayton, R.W., 2008. Nonvolcanic tremor observed in the Mexican subduction zone, *Geophys. Res. Lett.,* **35,** L07305, doi:10.1029/2007GL032877.

Peña, C., Heidbach, O., Moreno, M., Bedford, J., Ziegler, M., Tassara, A. & Oncken, O., 2019. Role of lower crust in the postseismic deformation of the 2010 Maule earthquake: insights from a model with power-law rheology, *Pure appl. Geophys.,* **176,** 3913–3928.

Pérez-Campos, X. *et al.*, 2008. Horizontal subduction and truncation of the Cocos Plate beneath central Mexico, *Geophys. Res. Lett.,* **35,** L18303, doi:10.1029/2008GL035127.

Pollitz, F.F., Bürgmann, R. & Segall, P., 1998. Joint estimation of afterslip rate and postseismic relaxation following the 1989 Loma Prieta earthquake, *J. geophys. Res.,* **103**(B11), 26975–26992.

Qiu, Q., Moore, J.D., Barbot, S., Feng, L. & Hill, E.M., 2018. Transient rheology of the Sumatran mantle wedge revealed by a decade of great earthquakes, *Nat. Commun.,* **9**(995), doi:10.1038/s41467-018-03298-6.

Quintanar, L., Rodríguez-Lozoya, H.E., Ortega, R., Gómez-González, J.M., Domínguez, T., Javier, C., Alcántara, L. & Rebollar, C.J., 2010. Source characteristics of the 22 January 2003 Mw = 7.5 Tecomán, Mexico, Earthquake: New insights, *Pure appl. Geophys.,* **168,** 1339–1353.

Radiguet, M., Cotton, F., Vergnolle, M., Campillo, M., Walpersdorf, A., Cotte, N. & Kostoglodov, V., 2012. Slow slip events and strain accumulation in the Guerrero gap, Mexico, *J. geophys. Res.,* **117,** B04305, doi:10.1029/2011JB008801.

Reyes, A., Brune, J.N. & Lomnitz, C., 1979. Source mechanism and aftershock study of the Colima, Mexico earthquake of January 30, 1973, *Bull. seism. Soc. Am.,* **69,** 1819–1840.

Schmitt, S.V., DeMets, C., Stock, J., Sánchez, O., Marquez-Azua, B. & Reyes, G., 2007. A geodetic study of the 2003 January 22 Tecomán, Colima, Mexico earthquake, *Geophys. J. Int.,* **169,** 389–406.

Scholz, C.H., 2002. *The Mechanics of Earthquakes and Faulting,* Cambridge Univ. Press.

Selvans, M.M., Stock, J.M., DeMets, C., Sánchez, O. & Marquez-Azua, B., 2011. Constraints on Jalisco block motion and tectonics of the Guadalajara Triple Junction from 1998–2001 Campaign GPS Data, *Pure appl. Geophys.,* **168,** 1435–1447.

Seton, M. *et al.*, 2020. A Global Data Set of Present-Day Oceanic Crustal Age and Seafloor Spreading Parameters, *Geochem. Geophys. Geosyst.,* **21,** e2020GC009214, doi:10.1029/2020GC009214.

Sherrill, E.M. & Johnson, K. M., 2021. New insights into the slip budget at Nankai: an iterative approach to estimate coseismic slip and afterslip, *J. geophys. Res.,* **126,** e2020JB020833, doi:10.1029/2020JB020833.

Shi, Q., Barbot, S., Wei, S., Tapponnier, P., Matsuzawa, T. & Shibazaki, B., 2020. Structural control and system-level behavior of the seismic cycle at the Nankai Trough, *Earth Planets Space,* **72**(1), 1–31.

Singh, S.K., Ponce, L. & Nishenko, S.P., 1985. The great Jalisco, Mexico, earthquakes of 1932: Subduction of the Rivera plate, *Bull. seism. Soc. Am.,* **75,** 1301–1314.

Singh, S.K. *et al.*, 2003. A preliminary report on the Tecomán, Mexico earthquake of 22 January 2003 (M_W 7.4) and its effects, *Sesimol. Res. Lett.,* **74**(3), 279–289.

Suárez, G. & Sánchez, O., 1996. Shallow depth of seismogenic coupling in southern Mexico: implications for the maximum size of earthquakes in the subduction zone, *Phys. Earth planet. Inter.,* **93,** 53–61.

Suhardja, S.K., Grand, S.P., Wilson, D., Guzman-Speziale, M., Gómez-González, J.M., Domínguez-Reyes, T. & Ni, J., 2015. Crust and subduction zone structure of Southwestern Mexico, *J. geophys. Res.,* **120,** 1020–1035.

Suito, H. & Freymueller, J.T., 2009. A viscoelastic and afterslip postseismic deformation model for the 1964 Alaska earthquake, *J. geophys. Res.,* **114,** B11404.

Sun, T. & Wang, K., 2015. Viscoelastic relaxation following subduction earthquakes and its effects on afterslip determination, *J. geophys. Res.,* **120,** 1329–1344.

Sun, T. *et al.*, 2014. Prevalence of viscoelastic relaxation after the 2011 Thoku-oki earthquake, *Nature,* **514,** 84–87.

Sun, T., Wang, K. & He, J., 2018. Crustal deformation following great subduction earthquakes controlled by earthquake size and mantle rheology, *J. geophys. Res.,* **123,** 5323–5345.

Trubienko, O., Fleitout, L., Garaud, J.-D. & Vigny, C., 2013. Interpretation of interseismic deformations and the seismic cycle associated with large subduction earthquakes, *Tectonophysics,* **589,** 126–141.

Tsang, L.L., Hill, E.M., Barbot, S., Qiu, Q., Feng, L., Hermawan, I., Banerjee, P. & Natawidjaja, D.H., 2016. Afterslip following the 2007 Mw 8.4 Bengkulu earthquake in Sumatra loaded the 2010 Mw 7.8 Mentawai tsunami earthquake rupture zone, *J. geophys. Res.,* **121**(12), 9034–9049.

UNAVCO Community, 2014a. *TLALOCNet - TNCM-TNCM_TNET_MX2014 P.S., UNAVCO, GPS/GNSS Observations Dataset,* doi:10.7283/T5B856FW.

UNAVCO Community, 2014b. *TLALOCNet - TNMR-TNMR_TNET_MX2014 P.S., UNAVCO, GPS/GNSS Observations Dataset,* doi:10.7283/T5Z036FZ.

UNAVCO Community, 2015a. *TLALOCNet - PENA-PENA-TNET-MX2015 P.S., UNAVCO, GPS/GNSS Observations Dataset,* doi:10.7283/T5891464.

UNAVCO Community, 2015b. *TLALOCNet - TNCC-TNCC_TNET_MX2015 P.S., UNAVCO, GPS/GNSS Observations Dataset,* doi:10.7283/T50R9MSK.

UNAVCO Community, 2015c. *TLALOCNet - TNLC-TNLC_TNET_MX2015 P.S., UNAVCO, GPS/GNSS Observations Dataset,* doi:10.7283/T5CZ35J8.

UNAVCO Community, 2015d. *TLALOCNet - TNMZ-Manzanilo_TNET_MX_2015 P.S., UNAVCO, GPS/GNSS Observations Dataset,* doi:10.7283/03FG-YJ81.

UNAVCO Community, 2017a. *TLALOCNet - TNCT-Chalacatepec__TNET_MX_2017 P.S., UNAVCO, GPS/GNSS Observations Dataset,* doi:10.7283/JCTK-TZ92.

UNAVCO Community, 2017b. *TLALOCNet - TNTM-Tamarindo_TNET_MX_2017 P.S., UNAVCO, GPS/GNSS Observations Dataset,* doi:10.7283/PN65-9M91.

UNAVCO Community & DeMets, C., 2007. *Jalisco GPS Network - PENA-US Gypsum Mine at Pena Colorada P.S., UNAVCO, GPS/GNSS Observations Dataset,* doi:10.7283/T5K35S10.

Vergnolle, M., Walpersdorf, A., Kostoglodov, V., Tregoning, P., Santiago, J.A., Cotte, N. & Franco, S.I., 2010. Slow slip events in Mexico revised from the processing of 11 year GPS observations, *J. geophys. Res.,* **115,** B08403, doi:10.1029/2009JB006852.

Wang, K., 2007. Elastic and viscoelastic models of crustal deformation in subduction earthquake cycles, in *The Seismogenic Zone of Subduction Thrust Faults,* eds, Dixon, T.H. & Moore, J.C., pp. 540–575, Columbia Univ. Press.

Wang, K., Hu, Y. & He, J., 2012. Deformation cycles of subduction earthquakes in a viscoelastic Earth, *Nature,* **484,** 327–332.

Watkins, W.D., Thurber, C.H., Abbott, E.R. & Brudzinski, M.R., 2018. Local earthquake tomography of the Jalisco, Mexico region, *Tectonophysics,* **724–725,** 51–64.

Weiss, J.R. *et al.*, 2019. Illuminating subduction zone rheological properties in the wake of a giant earthquake, *Sci. Adv.,* **5**(12), eaax6720, doi:10.1126/sciadv.aax6720.

Wessel, P. & Smith, W.H.F., 1991. Free software helps map and display data, *EOS, Trans. Am. geophys. Un.,* **72**(41), 445–446.

Wiseman, K., Bürgmann, R., Freed, A.M. & Banerjee, P., 2015. Viscoelastic relaxation in a heterogeneous Earth following the 2004 Sumatra-Andaman earthquake, *Earth planet. Sci. Lett.,* **431,** 308–317.

Yagi, Y., Mikumo, T., Pacheco, J. & Reyes, G., 2004. Source rupture process of the Tecomán, Colima, Mexico Earthquake of 22 January 2003, determined by joint inversion of teleseismic body-wave and near-source data, *Bull. seism. Soc. Am.,* **94**(5), 1795–1807.

Yoshioka, S., Mikumo, T., Kostoglodov, V., Larson, K., Lowry, A. & Singh, S., 2004. Interplate coupling and a recent aseismic slow slip event in the Guerrero seismic gap of the Mexican subduction zone, as deduced from GPS data inversion using a Bayesian information criterion, *Phys. Earth Planet. Inter.,* **146,** 513–530.

Zumberge, J.F., Heflin, M.B., Jefferson, D.C., Watkins, M.M. & Webb, F.H., 1997. Precise point positioning for the efficient and robust analysis of GPS data from large networks, *J. geophys. Res.,* **102,** 5005–5017.

SUPPORTING INFORMATION

Supplementary data are available at *GJI* online.

vel&slip_files.zip
Supp_Information_Cosenza-Muralles_etal_2021-I.pdf

Table S1: GPS site information

Table S2: Co-seismic displacements from the 1995 Colima–Jalisco earthquake at GPS sites active during the earthquake.

Table S3: Comparative 2003 earthquake sizes for models using time-series corrected for viscoelastic relaxation from a mantle using different Maxwell times (τ_{m}).

Table S4: Co-seismic displacements from the 2003 Tecomán earthquake at GPS sites active during the earthquake.

Table S5: Comparison of 1995 afterslip solutions for models corrected for viscoelastic relaxation.

Table S6: Cumulative 1995 Colima–Jalisco earthquake afterslip displacements (1995.77–2020.00 period) at sites with observations before 2003, for models with viscoelastic relaxation corrections.

Table S7: Comparison of 2003 afterslip solutions for models corrected for viscoelastic relaxation.

Table S8: Cumulative 2003 Tecomán earthquake afterslip displacements (2003.06–2020.00 period) at sites with observations before 2005.

Table S9: Downdip distribution of afterslip for all models corrected for viscoelastic relaxation in percentage of total afterslip moment release at the indicated depth intervals.

Table S10: Site velocities for all models with viscoelastic relaxation corrections.

Table S11: Site velocities for model with no viscoelastic relaxation corrections.

Table S12: Misfit F (eq. 1.3) and weighted root mean square (wrms) error (eq. 1.4) for all models with viscoelastic relaxation corrections.

Figure S1: Time coverage of the GPS sites. Vertical lines indicate earthquake dates.

Figure S2: Checkerboard tests for the Jalisco–Colima subduction zone. Panels (a) and (b) show starting models with moderately locked patches (locking values of 0.5) and their predicted (synthetic) horizontal GPS velocities. Panels (c) and (d) show locking solutions recovered from inversions of the synthetic GPS velocities with 1σ noise added ($\sigma = 1$ mm for the north and east components, and $\sigma = 2$ mm for the vertical component) and the residuals of the horizontal site velocities from the best fitting solutions. Purple line delimits the 1995 co-seismic rupture area as shown in Fig. 20 of the main document.

Figure S3: Checkerboard tests for the Jalisco–Colima subduction zone. Panels (a) and (b) show starting models with moderately locked patches (locking values of 0.5) and their predicted (synthetic) horizontal GPS velocities. Panels (c) and (d) show locking solutions recovered from inversions of the synthetic GPS velocities with 1σ noise added ($\sigma = 1$ mm for the north and east components, and $\sigma = 2$ mm for the vertical component) and the residuals of the horizontal site velocities from the best fitting solutions. Purple line delimits the 1995 afterslip area as shown in Fig. 20 of the main document.

Figure S4: Checkerboard tests for the Jalisco–Colima subduction zone. Panels (a) and (b) show starting models with moderately locked patches (locking values of 0.5) and their predicted (synthetic) horizontal GPS velocities. Panels (c) and (d) show locking solutions recovered from inversions of the synthetic GPS velocities with 1σ noise added ($\sigma = 1$ mm for the north and east components, and $\sigma = 2$ mm for the vertical component) and the residuals of the horizontal site velocities from the best fitting solutions. Purple line delimits the 2003 co-seismic rupture area as shown in Fig. 20 of the main document.

Figure S5: Checkerboard tests for the Jalisco–Colima subduction zone. Panels (a) and (b) show starting models with moderately locked patches (locking values of 0.5) and their predicted (synthetic) horizontal GPS velocities. Panels (c) and (d) show locking solutions recovered from inversions of the synthetic GPS velocities with 1σ noise added ($\sigma = 1$ mm for the north and east components, and $\sigma = 2$ mm for the vertical component) and the residuals of the horizontal site velocities from the best fitting solutions. Purple line delimits the 2003 afterslip area as shown in Fig. 20 of the main document.

Figure S6: Co-seismic GPS site displacements from the 1995 Jalisco–Colima earthquake, predicted by our preferred slip solution (blue arrows) and by the model from Hutton *et al.* (2001; magenta arrows).

Figure S7: TDEFNODE slip solutions for the 1995 Colima–Jalisco earthquake using observations from the interval indicated on each panel. '15 sites' refers to the use of the sites active during the earthquake exclusively. Dashed lines show the slab contours every 20 km. Black dots locate the fault nodes where slip is estimated.

Figure S8: TDEFNODE geodetic slip solutions for the 2003 Colima–Jalisco earthquake using time-series corrected for the viscoelastic effects of the 1995 Tecoman earthquake with $\tau_m = 15$ yr for the mantle. The interval used for the inversion is shown in each panel. Bottom right panel (1993.28–2020.00) corresponds to a model with no viscoelastic corrections. Dashed lines show the slab contours every 20 km. Black dots locate the fault nodes where slip is estimated.

Figure S9: TDEFNODE slip solutions for the 2003 Tecoman earthquake using time-series corrected for the viscoelastic effects of the 1995 Colima–Jalisco earthquake. The Maxwell time τ_m for the mantle corresponding to the correction is indicated in each panel. The interval used for the inversion was 1993.28–2005.50. Dashed lines show the slab contours every 20 km. Black dots locate the fault nodes where slip is estimated.

Figure S10: Co-seismic GPS site displacements from the 2003 Tecoman earthquake, predicted by Schmitt *et al.* (2007; magenta arrows) and by our preferred slip solution for the model corresponding to the correction for the viscoelastic effects of a mantle with $\tau_m = 15$ yr (blue arrows).

Figure S11: Modelled viscoelastic deformation for the 2003 Tecomán earthquake at selected GPS sites, for mantle rheologies corresponding to Maxwell times of 2.5 (blue), 15 (red) and 40 yr (green).

Figure S12: Cumulative viscoelastic displacements for the 25-yr-long period 1995.77 to 2020.27 triggered by the 1995 Colima–Jalisco and the 2003 Tecomán earthquakes, as predicted with RELAX software using our preferred co-seismic slip solutions. The displacements shown in each panel were determined using the mantle Maxwell time given in the lower right corner of each panel. Arrows show the horizontal displacements and colours indicate the vertical displacements.

Figure S13: Modelled viscoelastic deformation for the 1995 Colima–Jalisco and the 2003 Tecomán earthquakes at selected GPS sites, for mantle rheologies corresponding to Maxwell times of 2.5 (blue), 15 (red) and 40 yr (green). The dashed vertical lines mark the time of the 2003 Tecomán earthquake.

Figure S14: Daily north, east and vertical displacements for GPS station COLI, from 1993 to 2019. Grey dots correspond to the original time-series. Blue, red and green dots correspond to the time-series corrected for the viscoelastic deformation response from the 1995 and 2003 earthquakes, using $\tau_m = 2.5$, 15 and 40 yr, respectively. The black dashed line marks the time of the 2003 Tecoman earthquake.

Figure S15: TDEFNODE slip solutions for the 1995 Colima–Jalisco earthquake afterslip (integrated over the 1995.77–2020.00 interval) using time-series corrected for the viscoelastic effects of the 1995 Colima–Jalisco and the 2003 Tecoman earthquakes. The mantle Maxwell times τ_m used for the corrections are indicated in each panel. The interval of observations used for the inversions was 1993.28–2020.00. Dashed lines show the slab contours every 20 km. Black dots locate the fault nodes where slip is estimated.

Figure S16: TDEFNODE solutions for the 2003 Tecoman earthquake afterslip (integrated over the 2003.06–2020.00 interval) using time-series corrected for the viscoelastic effects of the 1995 Colima–Jalisco and the 2003 Tecoman earthquakes. The mantle Maxwell times τ_m used for the corrections are indicated in each panel. The interval of observations used for the inversions was 1993.28–2020.00. Dashed lines show the slab contours every 20 km. Black dots locate the fault nodes where slip is estimated.

Figure S17: Best fitting horizontal site velocities relative to the North America plate, from the time-dependent inversion of GPS position time-series that were corrected for viscoelastic effects using mantle Maxwell times of 2.5 (green), 15 (red) and 40 (blue) yr. Uncertainties have been omitted for clarity.

Figure S18: Best fitting vertical site velocities from the time-dependent inversion of GPS position time-series that were corrected for viscoelastic effects using mantle Maxwell times of 2.5 (green), 15 (red) and 40 (blue) yr. Black dots show the site locations. Superposing velocity vectors are shifted to the right to help visualization. Uncertainties have been omitted for clarity.

Figure S19: TDEFNODE slip solution for (a) the 1995 Colima–Jalisco earthquake and (b) its post-seismic afterslip for a model without viscoelastic effect corrections. EQ: earthquake. Dashed lines show the slab contours every 20 km. Black dots locate the fault nodes where slip is estimated. The blue line delimits the earthquake aftershock area (Pacheco *et al.* 1997). White, yellow and red stars are the epicentres from Courboulex *et al.* (1997) and USGS, and the centroid from the gCMT catalogue (Dziewonski *et al.* 1997), respectively. Panels (c) and (d) respectively show the horizontal and vertical site motions that are predicted by the co-seismic and afterslip solutions from panels (a) and (b) at sites active during the earthquake for panel (c) and sites active between 1995 and 2003 for panel (d).

Figure S20: TDEFNODE slip solution for (a) the 2003 Tecomán earthquake and (b) its post-seismic afterslip for a model without viscoelastic effects corrections. EQ: earthquake. Dashed lines show the slab contours every 20 km. Black dots locate the fault nodes where slip is estimated. The red line delimits the rupture area for the earthquake (Yagi *et al.* 2004). White, yellow and red stars are the epicentres from Yagi *et al.* (2004) and USGS, and the centroid from the gCMT catalogue (Ekström *et al.* 2004), respectively. Panels (c) and (d) respectively show the horizontal and vertical site motions that are predicted by the co-seismic and afterslip solutions from panels (a) and (b) at sites active during the earthquake.

Figure S21: Residuals at selected sites from our model with viscoelastic corrections using $\tau_{\mathrm{m}} = 8$ yr for the mantle (red) and with no corrections for viscoelastic effects (blue). Dashed vertical lines mark the time of the 1995 and 2003 earthquakes.